

PROSPECTS FOR B-PHYSICS IN THE NEXT DECADE

Sheldon Stone
Department of Physics
Syracuse University
Syracuse, N.Y. 13244-1130
Email: Stone@suhep.phy.syr.edu

ABSTRACT

In these lectures I review what has been learned from studies of b -quark decays, including semileptonic decays (V_{ub} and V_{cb}), $B^0 - \bar{B}^0$ mixing and rare B decays. Then a discussion on CP violation follows, which leads to a summary of plans for future experiments and what is expected to be learned from them.

Presented at NATO Advanced Study Institute on Techniques and Concepts of High Energy Physics, Virgin Islands, July 1996

1. INTRODUCTION

My assignment is to discuss “Future B Physics Experiments.” But to understand what results we desire, it is necessary to understand past accomplishments and have a firm theoretical background. In this paper I will give a brief theoretical introduction to the “Standard Model,” and historical introduction to the study of b quark decays. Then I will discuss in some detail the physics already found including: B lifetimes, semileptonic B decays and the CKM couplings V_{cb} and V_{ub} , $B^o - \bar{B}^o$ mixing, rare b decays, and CP violation in K_L^o decays. Following this is a pedantic discussion on CP violation in B decays, which leads into a discussion of future experiments.

1.1. Theoretical Background

The physical states of the “Standard Model” are comprised of left-handed doublets containing leptons and quarks and right handed singlets¹

$$\begin{pmatrix} u \\ d \end{pmatrix}_L, \begin{pmatrix} c \\ s \end{pmatrix}_L, \begin{pmatrix} t \\ b \end{pmatrix}_L, \quad u_R, d_R, c_R, s_R, t_R, b_R \quad (1)$$

$$\begin{pmatrix} e^- \\ \nu_e \end{pmatrix}_L, \begin{pmatrix} \mu^- \\ \nu_\mu \end{pmatrix}_L, \begin{pmatrix} \tau^- \\ \nu_\tau \end{pmatrix}_L, \quad e_R^-, \mu_R^-, \tau_R^-, \nu_{eR}, \nu_{\mu R}, \nu_{\tau R}. \quad (2)$$

The gauge bosons, W^\pm , γ and Z^o couple to mixtures of the physical d , s and b states. This mixing is described by the Cabibbo-Kobayashi-Maskawa (CKM) matrix (see below).²

The Lagrangian for charged current weak decays is

$$L_{cc} = -\frac{g}{\sqrt{2}} J_{cc}^\mu W_\mu^\dagger + h.c., \quad (3)$$

where

$$J_{cc}^\mu = (\bar{\nu}_e, \bar{\nu}_\mu, \bar{\nu}_\tau) \gamma^\mu \begin{pmatrix} e_L \\ \mu_L \\ \tau_L \end{pmatrix} + (\bar{u}_L, \bar{c}_L, \bar{t}_L) \gamma^\mu V_{CKM} \begin{pmatrix} d_L \\ s_L \\ b_L \end{pmatrix} \quad (4)$$

and

$$V_{CKM} = \begin{pmatrix} V_{ud} & V_{us} & V_{ub} \\ V_{cd} & V_{cs} & V_{cb} \\ V_{td} & V_{ts} & V_{tb} \end{pmatrix}. \quad (5)$$

Multiplying the mass eigenstates (d, s, b) by the CKM matrix leads to the weak eigenstates (d', s', b') . There are nine complex CKM elements. These 18 numbers can be reduced to four independent quantities by applying unitarity constraints and the fact that the phases of the quark wave functions are arbitrary. These four remaining numbers are **fundamental constants** of nature that need to be determined from

experiment, like any other fundamental constant such as α or G . In the Wolfenstein approximation* the matrix is written as³

$$V_{CKM} = \begin{pmatrix} 1 - \lambda^2/2 & \lambda & A\lambda^3(\rho - i\eta) \\ -\lambda & 1 - \lambda^2/2 & A\lambda^2 \\ A\lambda^3(1 - \rho - i\eta) & -A\lambda^2 & 1 \end{pmatrix} \quad (6)$$

The constants λ and A are determined from charged-current weak decays. To see how this is done, first consider muon decay. The muon decays weakly into $\nu_\mu e^- \bar{\nu}_e$ as shown in Fig. 1. The decay width is given by⁴

$$\Gamma_\mu = \frac{G_F^2}{192\pi^3} m_\mu^5 \times (\text{radiative corrections}). \quad (7)$$

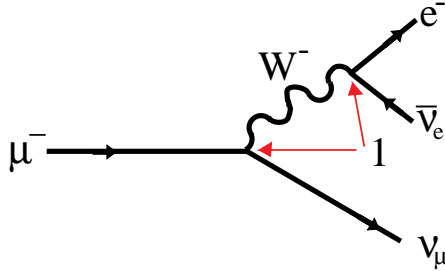


Fig. 1. Diagram for muon decay.

The couplings at the vertices are unity for leptons. This process serves to measure the weak interaction decay constant (Fermi constant) G_F .

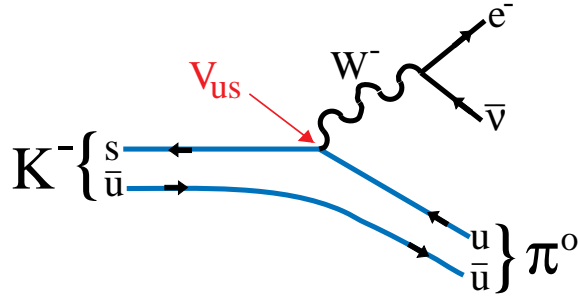


Fig. 2. Semileptonic K^- decay diagram.

A charged current decay diagram for strange quark decay is shown in Fig. 2. Here the CKM element V_{us} is present. The decay rate is given by a formula similar to equation (7), with the muon mass replaced by the s -quark mass and an additional factor of $|V_{us}|^2$. Two complications arise since we are now measuring a decay process involving hadrons, $K^- \rightarrow \pi^0 e^- \bar{\nu}$ rather than elementary constituents. One is that the

*In higher order other terms have an imaginary part; in particular the V_{cd} term becomes $-\lambda - A^2\lambda^5(\rho + i\eta)$, which is important for CP violation in K_L^0 decay.

s -quark mass is not well defined and the other is that we must make corrections for the probability that the \bar{u} -spectator-quark indeed forms a π^0 with the u -quark from the s -quark decay. These considerations will be discussed in greater detail in the semileptonic B decays section. For now⁵ remember that $\lambda = V_{us} = 0.2205 \pm 0.0018$ and, $A \approx 0.8$. Constraints on ρ and η are found from other measurements. These will also be discussed later.

1.2. B Decay Mechanisms

Fig. 3 shows sample diagrams for B decays. Semileptonic decays are shown in Fig. 3(a). The name “semileptonic” is given, since there are both hadrons and leptons in the final state. The leptons arise from the virtual W^- , while the hadrons come from the coupling of the spectator anti-quark with either the c or u quark from the b quark decay. Note that the B is massive enough that all three lepton species can be produced. The simple spectator diagram for hadronic decays (Fig. 3(b)) occurs when the virtual W^- materializes as a quark-antiquark pair, rather than a lepton pair. The terminology *simple spectator* comes from viewing the decay of the b quark, while ignoring the presence of the *spectator* antiquark. If the colors of the quarks from the virtual W^- are the same as the initial b quark, then the color suppressed diagram, Fig. 3(c), can occur. While the amount of color suppression is not well understood, a good first order guess is that these modes are suppressed in amplitude by the color factor $1/3$ and thus in rate by $1/9$, with respect to the non-color suppressed spectator diagram.

The annihilation diagram shown in Fig. 3(d) occurs when the b quark and spectator anti-quark find themselves in the same space-time region and annihilate by coupling to a virtual W^- . The probability of such a wave function overlap between the b and \bar{u} -quarks is proportional to a numerical factor called f_B . The decay amplitude is also proportional to the coupling V_{ub} . The mixing and penguin diagrams will be discussed later.

2. What is known

2.1. Early history

The first experimental evidence for b quarks was found at Fermilab by looking at high mass dimuon pairs in 800 GeV proton interactions on nuclear targets.⁶ Their results are shown in Fig. 4 along with subsequent data from DESY using e^+e^- annihilations which shows narrow peaks at the masses of the Υ and Υ' resonances.⁷

The natural width of the peaks is narrower than the energy resolution of either experiment leading to the interpretation that these states are comprised of a bound $b\bar{b}$ quark system. The narrow decay width is similar to the situation in charmonium,

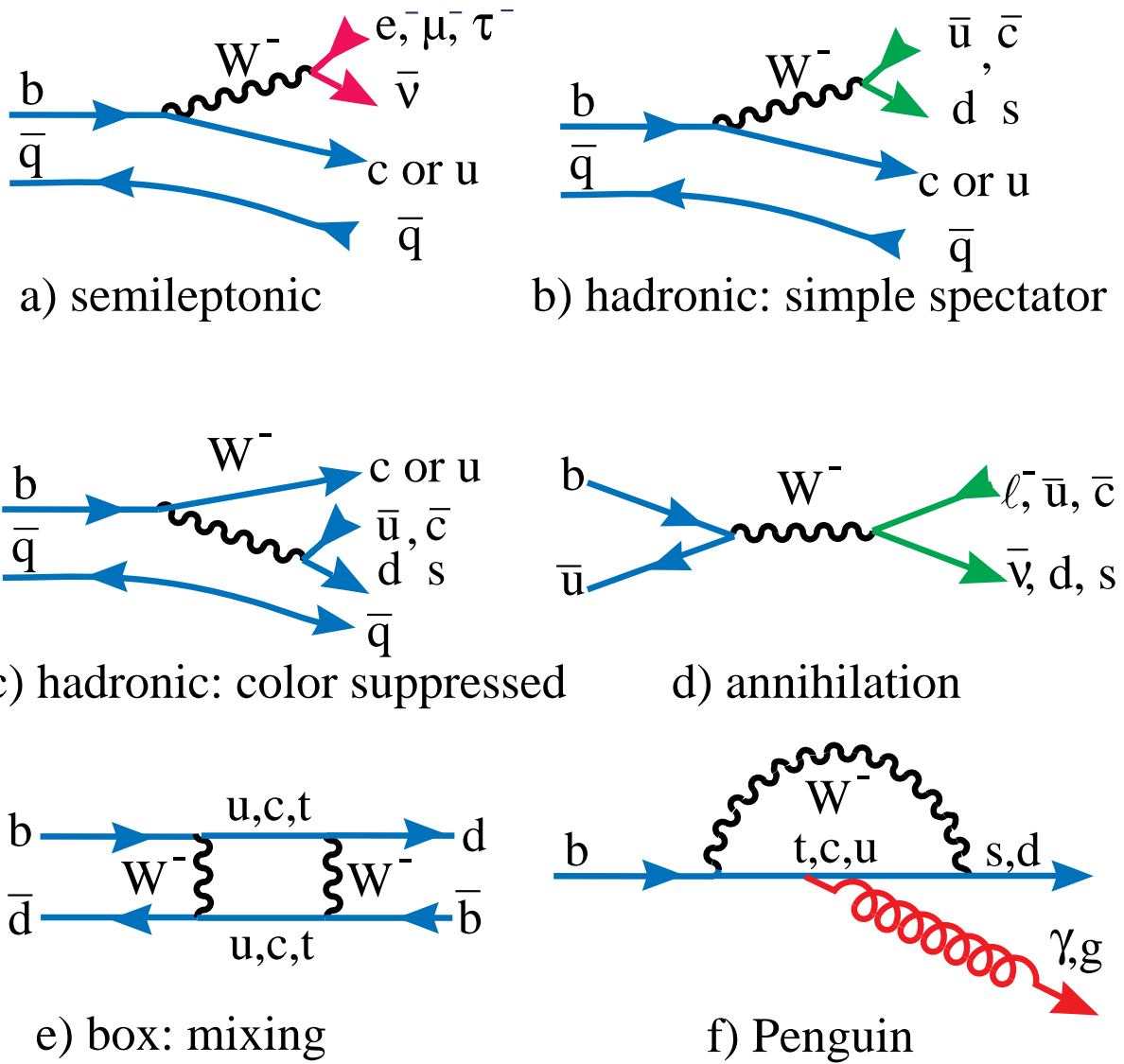


Fig. 3. Various mechanisms for B meson decay.

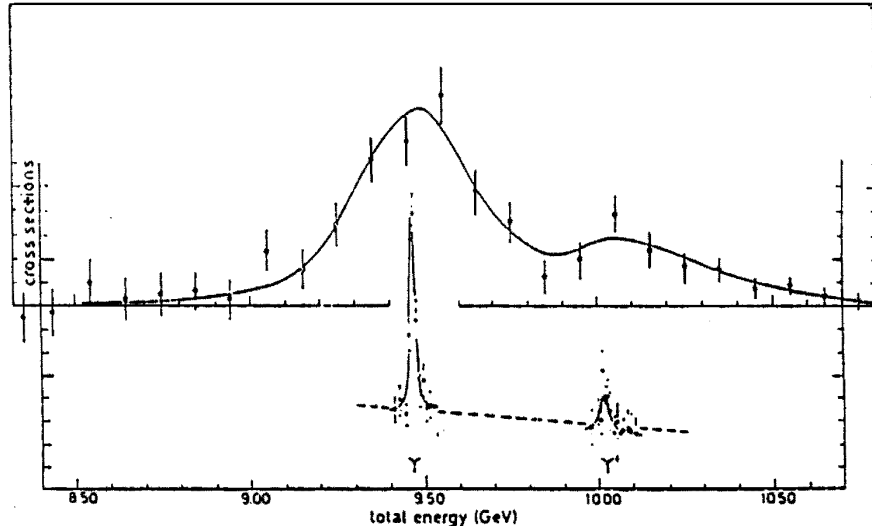


Fig. 4. The data on top is the $\mu^+\mu^-$ invariant mass from the Columbia-Fermilab-Stony Brook collaboration and the data shown below is the total e^+e^- cross-section from the DESY-Heidelberg-Hamburg-Munchen collaboration.

i.e. the decay width is proportional to the strong coupling constant α_s^3 .

As the DESY machine was limited in center-of-mass energy at that time, the torch was passed to the CLEO experiment at the CESR e^+e^- storage ring. An early total cross-section scan is shown in Fig. 5(a). A new narrow state, the Υ'' (or $\Upsilon(3S)$), appears along with a state wider than the experimental resolution, the $\Upsilon(4S)$.

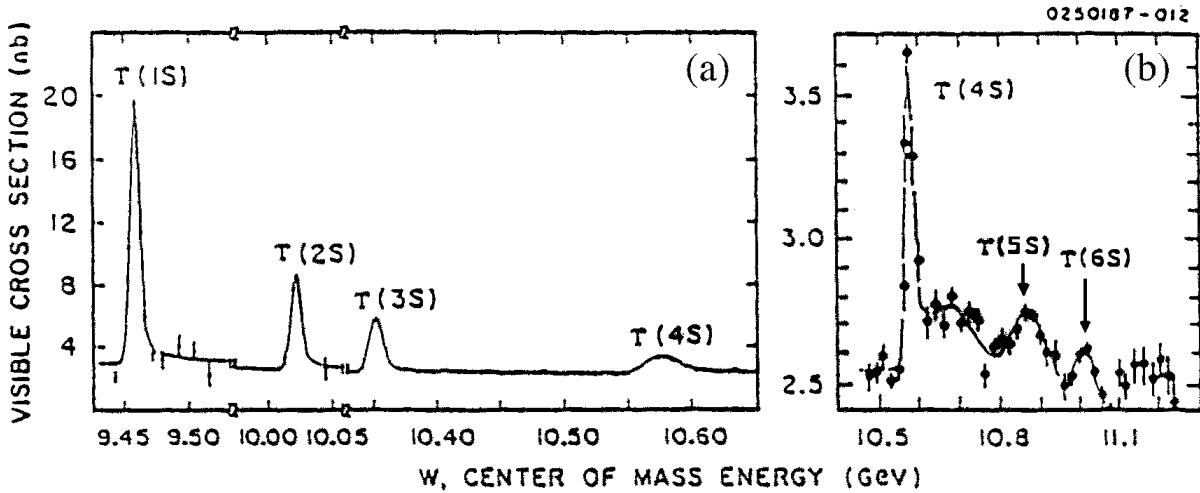


Fig. 5. Hadronic cross-section scan in the Upsilon region, (a) shows 1S-4S and (b) region above 4S.

The mechanism of b quark production in e^+e^- collisions and the subsequent production of the final states B^+B^- and $B^0\bar{B}^0$ from the $\Upsilon(4S)$ are shown in Fig. 6. Subsequent data shown in Fig. 5(b) shows that the cross-section is ≈ 1 nb and details structures in the total cross-section at higher energies.⁸ Little data has been taken

above the $\Upsilon(4S)$, however.

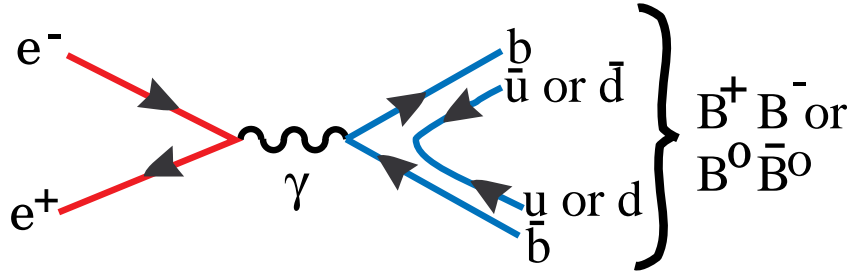


Fig. 6. B production mechanism at the $\Upsilon(4S)$.

Many properties of B meson decays have been discovered by two e^+e^- experiments operating at the $\Upsilon(4S)$ resonance, CLEO at CESR and ARGUS at DESY (the DESY machine group upgraded the energy so they could do this physics). Fully reconstructed B meson decays were first seen by CLEO and the B masses determined.⁹ Now there are several thousand fully reconstructed decays in many modes allowing for branching ratio determinations. A different technique is used to reconstruct B mesons at the $\Upsilon(4S)$ than at other machines. At this resonance we have

$$e^+e^- \rightarrow \Upsilon(4S) \rightarrow B^-B^+ \quad (8)$$

$$\rightarrow B^0\bar{B}^0. \quad (9)$$

From energy conservation, the energy of each B is equal to the beam energy, E_{beam} (the center-of-mass energy is twice E_{beam}). To reconstruct exclusive B meson decays, we first require the energy of the decay products be consistent with the beam energy. Suppose the final state we are considering is $D^0\pi^-$. We require that

$$E_{D^0} + E_{\pi^-} = E_{beam}. \quad (10)$$

In practice this means that the difference between the left-hand side and the right-hand side is less than ≈ 3 times the error on the measured energy sum.

The next step is to compute the invariant mass of the candidate B^- using the well known beam energy:

$$m_B = \sqrt{E_{beam}^2 - (\vec{p}_{D^0} + \vec{p}_{\pi^-})^2}. \quad (11)$$

In practice this technique leads to large background rejections and a B mass resolution of $\sigma \approx 2.5$ MeV (at CESR) which is due mostly to the energy spread of the beam. A few sample B decay candidate mass plots are shown in Fig. 7 from the CLEO experiment.¹⁰

Hadronic production rates for b quarks have been measured at two $p\bar{p}$ colliders, UA1 at the SPS,¹⁵ and CDF at the Tevatron.¹⁶ E789 has also measured b production using an 800 GeV proton beam hitting nuclear targets.¹⁷ CDF has reconstructed B meson decays into modes containing a ψ meson. These are shown¹⁴ in Fig. 8.

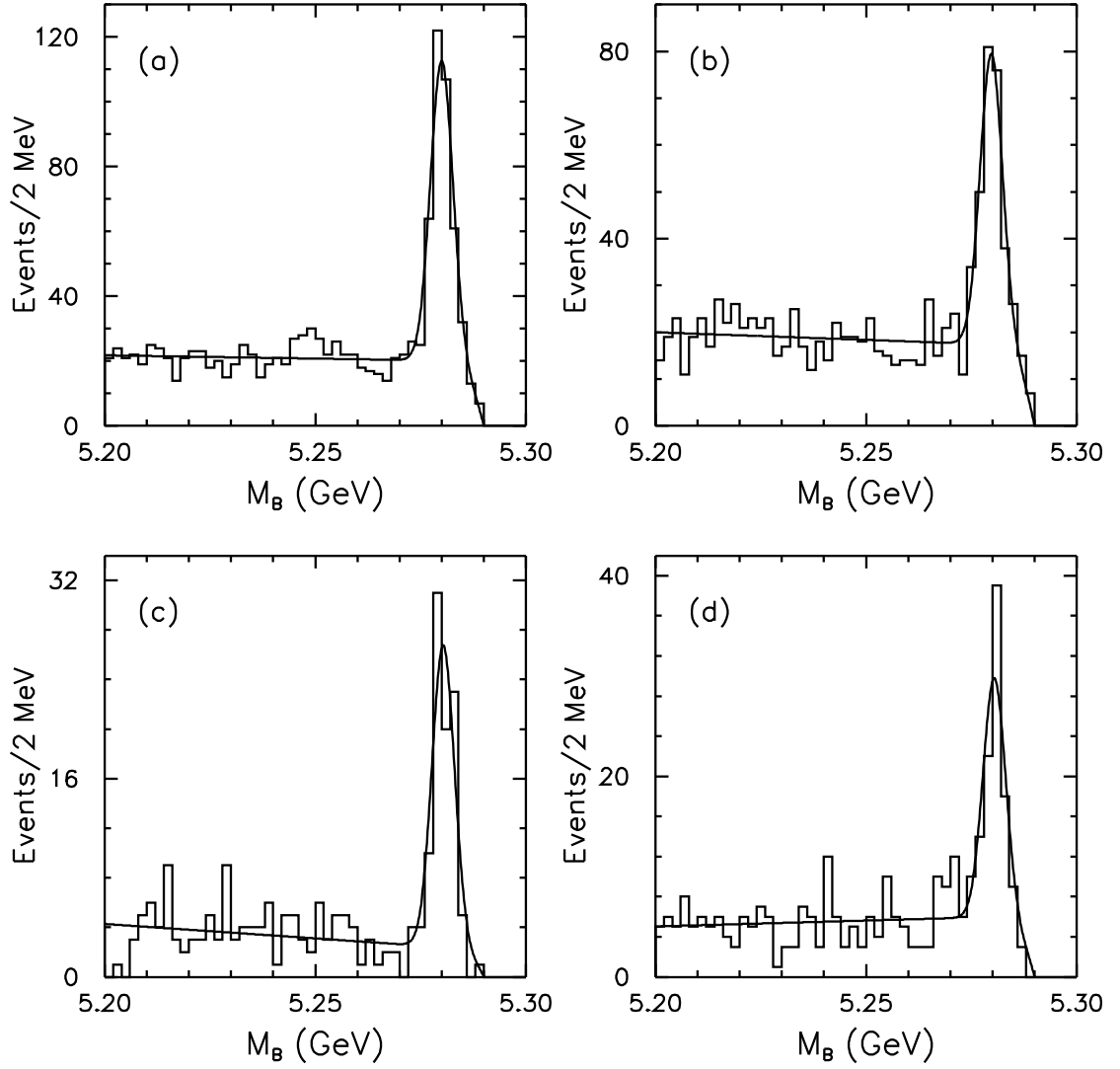


Fig. 7. Beam constrained mass distribution from CLEO for (a) $B^- \rightarrow D^0 \pi^-$, (b) $B^- \rightarrow D^0 \rho^-$, (c) $\bar{B}^0 \rightarrow D^+ \pi^-$ and (d) $\bar{B}^0 \rightarrow D^+ \rho^-$.

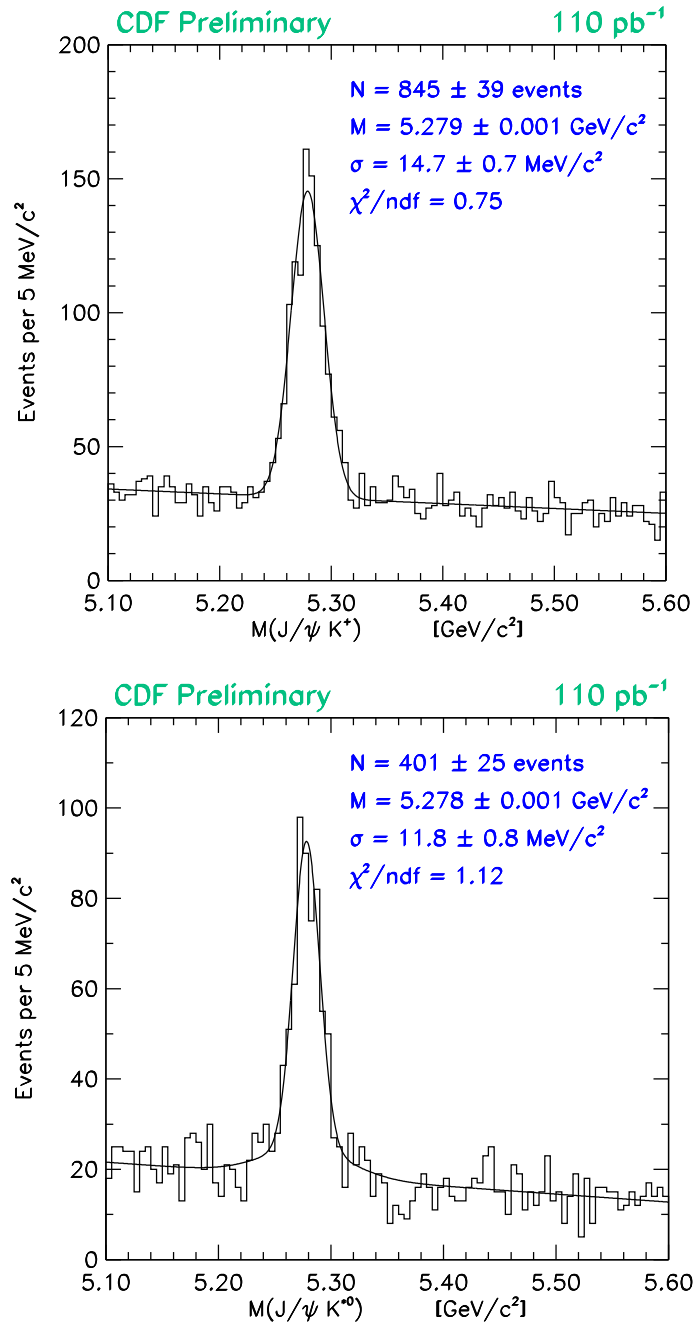


Fig. 8. Invariant mass spectra from CDF for ψK^+ and ψK^{*0} candidates.

2.2. Lifetimes

Lifetimes are a fundamental property of elementary particles. The b quark lifetime, however, was measured before the individual lifetimes of b flavored hadrons at the higher energy e^+e^- machines, PEP and PETRA.¹¹ More recent measurements have come from LEP, SLD and CDF.¹² The meaning of b quark lifetime is really the average of the B hadron lifetimes over the kinds of B hadrons which happen to be produced in the particular environment. The results are summarized in Table 1.¹³

Table 1. B lifetime measurements (ps)

	LEP Avg	CDF	SLD	World Avg
b quark	1.54 ± 0.02	1.51 ± 0.03	1.56 ± 0.05	1.53 ± 0.02
B^-	1.63 ± 0.06	1.68 ± 0.07		1.65 ± 0.05
B^0	1.52 ± 0.06	1.58 ± 0.09		1.55 ± 0.05
B_s^0	1.60 ± 0.10	1.36 ± 0.12		1.50 ± 0.08
Λ_b	1.21 ± 0.07	1.32 ± 0.17		1.23 ± 0.06
Ξ_b	$1.39^{+0.34}_{-0.28}$			$1.39^{+0.34}_{-0.28}$

The meson lifetimes are nearly equal implying the dominance of the spectator diagram. The Λ_b lifetime appears to be shorter, which implies the existence of other diagrams in baryon decay. This is very different from the situation in charm decay where the D^0 , D^+ and Λ_c have different lifetimes.

2.3. The CKM element V_{cb}

2.3.1. Theory of semileptonic decays

The same type of semileptonic charged current decays used to find V_{us} are used to find V_{cb} and V_{ub} . The basic diagram is shown in Fig. 3(a). We can use either inclusive decays, where we look only at the lepton and ignore the hadronic system at the lower vertex, or exclusive decays where we focus on a particular single hadron. Theory currently can predict either the inclusive decay rate, or the exclusive decay rate when there is only a single hadron in the final state. The fraction of semileptonic decays into exclusive final states containing either a pseudoscalar or vector meson is given in Table 2.

Now let us briefly go through the mathematical formalism of semileptonic decays. Let us start with pseudoscalar to pseudoscalar transitions. The decay amplitude is given by¹⁸

$$A(\bar{B} \rightarrow me^- \bar{\nu}) = \frac{G_F}{\sqrt{2}} V_{ij} L^\mu H_\mu, \text{ where} \quad (12)$$

$$L^\mu = \bar{u}_e \gamma^\mu (1 - \gamma_5) v_\nu, \text{ and} \quad (13)$$

Table 2. Fraction of $q \rightarrow x\ell\nu$ to 0^- or 1^- final states

s quark	100%	$K \rightarrow \pi\ell\nu$
c quark	>90%	$D \rightarrow (K + K^*)\ell\nu$
	?	$D \rightarrow (\pi + \rho)\ell\nu$
b quark	$\approx 66\%$	$B \rightarrow (D + D^*)\ell\nu$
	?	$B \rightarrow (\pi + \rho)\ell\nu$
t quark	0%	t does not form hadrons

$$H_\mu = \langle m | J_{had}^\mu(0) | \bar{B} \rangle = f_+(q^2)(P + p)_\mu + f_-(q^2)(P - p)_\mu, \quad (14)$$

where q^2 is the four-momentum transfer squared between the B and the m , and $P(p)$ are four-vectors of the $B(m)$. H_μ is the most general form the hadronic matrix element can have. It is written in terms of the unknown f functions that are called ‘‘form-factors.’’ It turns out that the term multiplying the $f_-(q^2)$ form-factor is the mass of lepton squared. Thus for electrons and muons (but not τ 's), the decay width is given by

$$\frac{d\Gamma_{sl}}{dq^2} = \frac{G_F^2 |V_{ij}|^2 K^3 M_B^2}{24\pi^2} |f_+(q^2)|^2, \quad \text{where} \quad (15)$$

$$K = \frac{M_B}{2} \left[\left(1 - \frac{m^2 - q^2}{M_B^2} \right) - 4 \frac{m^2 q^2}{M_B^4} \right]^{1/2} \quad (16)$$

is the momentum of the particle m (with mass m) in the B rest frame. In principle, $d\Gamma_{sl}/dq^2$ can be measured over all q^2 . Thus the shape of $f_+(q^2)$ can be determined experimentally. However, the normalization, $f_+(0)$ must be obtained from theory, for V_{ij} to be measured. In other words,

$$\Gamma_{SL} \propto |V_{ij}|^2 |f_+(0)|^2 \frac{1}{\tau_B} \int K^3 g(q^2) dq^2, \quad (17)$$

where $g(q^2) = f_+(q^2)/f_+(0)$. Measurements of semileptonic B decays give the integral term, while the lifetimes are measured separately, allowing the product $|V_{ij}|^2 |f_+(0)|^2$ to be experimentally determined.

For pseudoscalar to vector transitions there are three independent form-factors whose shapes and normalizations must be determined.¹⁹

2.3.2. $\bar{B}^0 \rightarrow D^+ \ell^- \bar{\nu}$

CLEO has recently measured the branching ratio and form-factor for the reaction $\bar{B}^0 \rightarrow D^+ \ell^- \bar{\nu}$ using two different techniques.²⁰ In the first method the final state is reconstructed finding only lepton and D^+ candidates, where the $D^+ \rightarrow K^- \pi^+ \pi^+$ decay is used. Then, using the fact that the B 's produced at the $\Upsilon(4S)$ are nearly at rest the missing mass squared (MM^2) is calculated as

$$\begin{aligned}
MM^2 &= E_\nu^2 - \vec{P}_\nu^2 \\
&= (E_B - E_{D^+} - E_\ell)^2 - (\vec{p}_B - \vec{p}_{D^+} - \vec{p}_\ell)^2 \\
&\approx (E_B - (E_{D^+} + E_\ell))^2 - (\vec{p}_{D^+} + \vec{p}_\ell)^2 \\
&\approx E_{beam}^2 + m_B^2 + m_{D^+}^2 + m_\ell^2 - 2\vec{p}_{D^+} \cdot \vec{p}_\ell,
\end{aligned} \tag{18}$$

where E refers to particle energy, m to mass and \vec{p} to three-momentum. The approximation on the third line results from setting p_B to zero. This approximation causes a widening of the MM^2 distribution, giving a r.m.s. width of 0.2 GeV².

This analysis is done by finding the number of D^+ events with opposite sign leptons in different q^2 and MM^2 bins. The $K^-\pi^+\pi^+$ mass distributions for the interval $4 > q^2 > 2$ GeV² and several MM^2 bins are shown in Fig. 9.

There is also a large background from $\bar{B}^0 \rightarrow D^{*+}X\ell^-\bar{\nu}$ decays where the $D^{*+} \rightarrow \pi^0 D^+$. These events are reconstructed and their MM^2 distribution is directly subtracted (after correcting for efficiencies) from the candidate signal distribution. We are left with a sample that contains $D^+\ell^-\bar{\nu}$ decays and also $D^+X\ell^-\bar{\nu}$, where X can be a single hadron or hadrons but cannot be the result of final state with a D^{*+} . We ascertain the total number of signal events by fitting the MM^2 distribution in the different q^2 bins as shown in Fig. 10 to a $D^+\ell^-\bar{\nu}$ signal shape and a background shape for $D^+X\ell^-\bar{\nu}$.

The second technique reconstructs the neutrino by using missing energy and momentum measurements. Essentially all charged tracks and photons in the event are added up and since the total energy must be equal to the center of mass energy and the total three-momentum must be zero, any difference is assigned to the neutrino. Events with a second lepton or which do not conserve charge are eliminated. Furthermore, the momentum and energy measurements must be consistent. Once the neutrino four-vector is determined, the B can be reconstructed in the ‘‘usual’’ way as shown in Fig. 11.

The MM^2 technique gives a branching ratio of $(1.75 \pm 0.25 \pm 0.20)\%$, while the neutrino reconstruction gives $(1.89 \pm 0.22 \pm 0.35)\%$, giving a combined (preliminary) yield of $(1.78 \pm 0.20 \pm 0.24)\%$. The statistical errors in both methods are essentially uncorrelated, while the systematic error is almost completely correlated.

The q^2 distribution from the MM^2 method is shown in Fig. 12. The intercept at q^2 of zero is proportional to $|V_{cb}f_+(0)|^2$. The curve is a fit to a functional form

$$f_+(q^2) = \frac{f_+(0)}{1 - q^2/M_V^2}, \tag{19}$$

where M_V is left unspecified but is theorized to be the mass of the vector exchange particle in the t channel, namely the B^* . The results and comparison with different models are shown in Table 3.

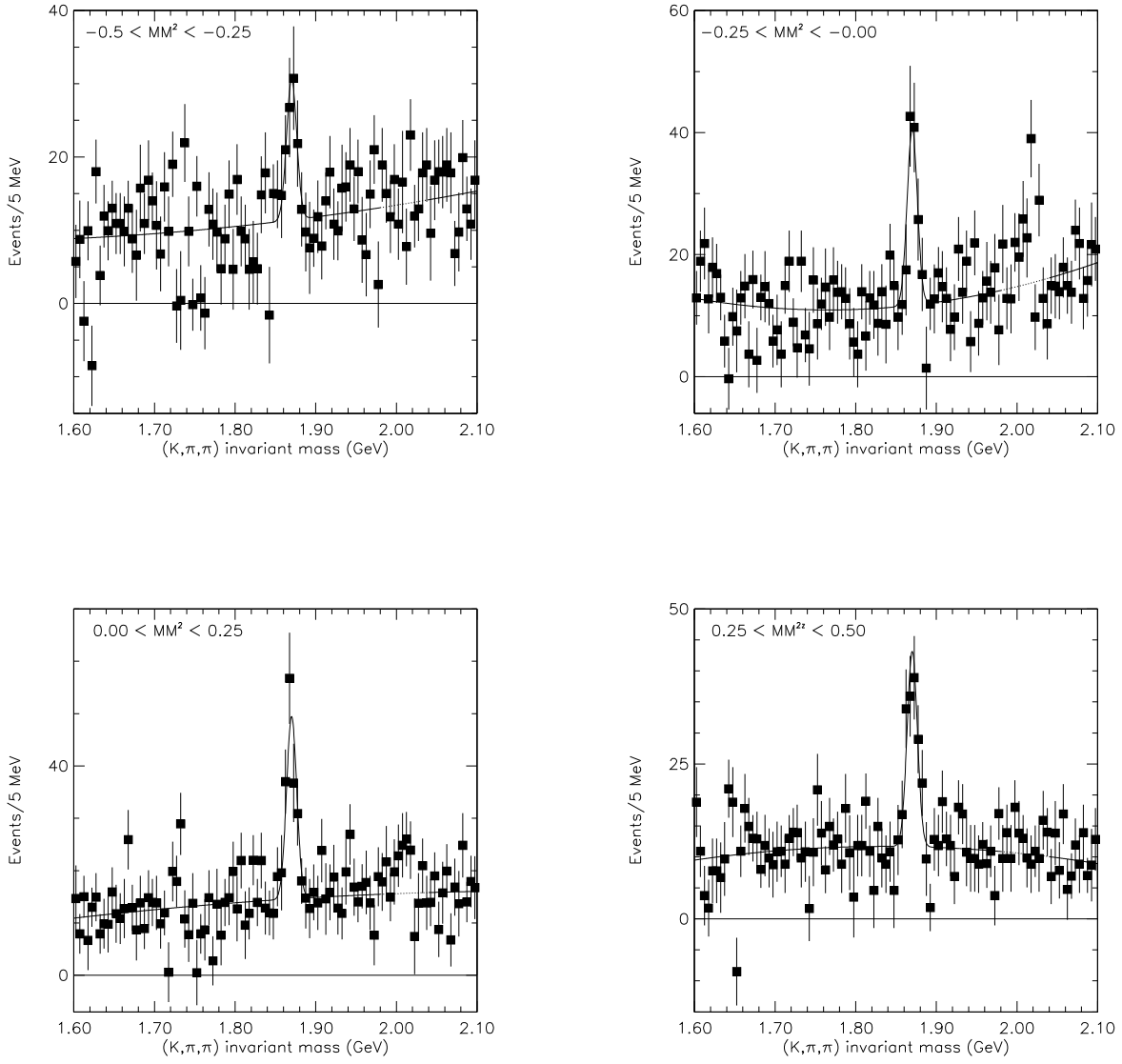


Fig. 9. Invariant $K^-\pi^+\pi^+$ mass spectra from CLEO for events with an opposite sign lepton in the interval $4 > q^2 > 2$ in four different MM^2 slices. The curves are a fit to a Gaussian signal shape summed with a polynomial background.

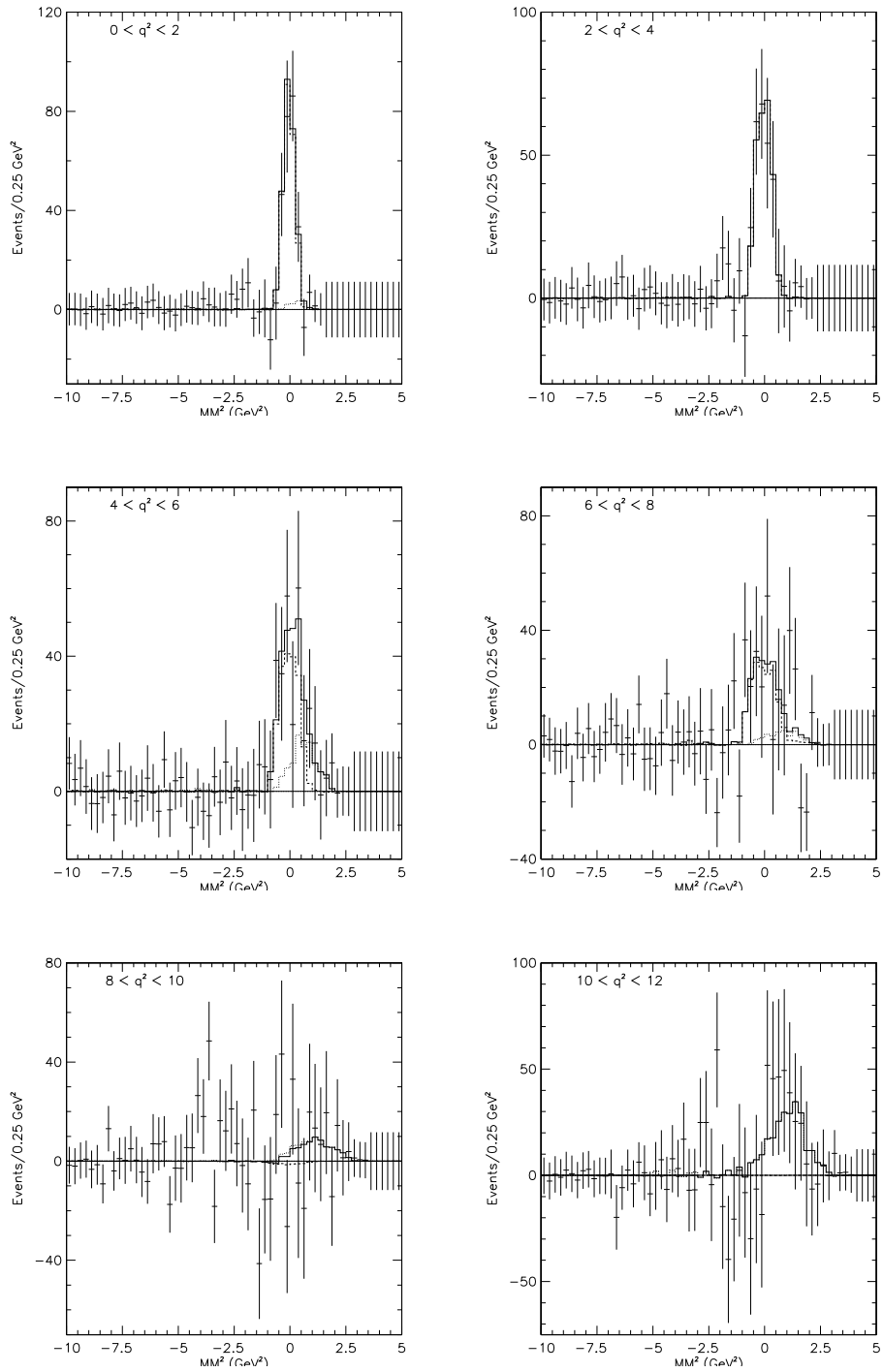


Fig. 10. Fits to the MM^2 distribution for the $D^+ \ell^- \bar{\nu}$ (dashed) and $D^+ X \ell^- \bar{\nu}$ (dotted) components and the sum (solid) in different q^2 intervals

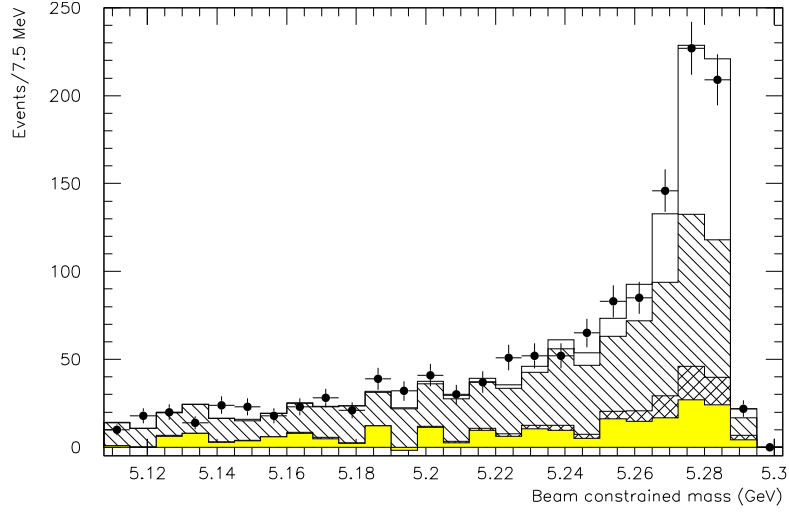


Fig. 11. Beam constrained mass spectrum for all events passing the cuts. The white area represents the signal events, the hatched area represents the combinatoric background, the crosshatched area represents the $D^{*+}\ell^{-}\bar{\nu}$ and the shaded area represents all the remaining backgrounds.

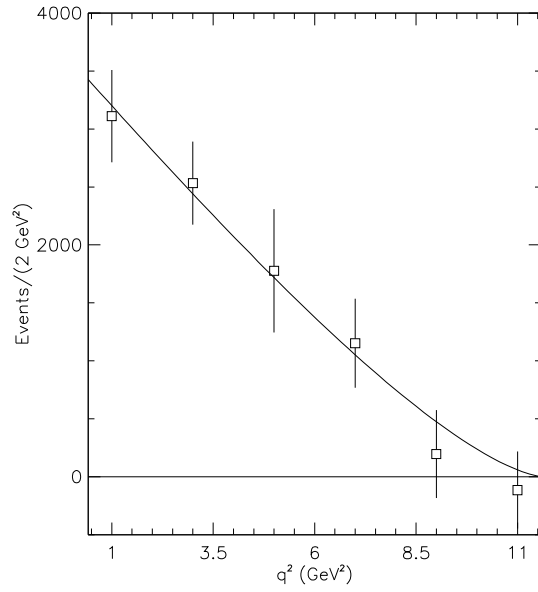


Fig. 12. The q^2 distribution for $\bar{B}^0 \rightarrow D^+\ell^-\bar{\nu}$ from the MM^2 analysis.

Table 3. Results of $\bar{B}^o \rightarrow D^+ \ell^- \bar{\nu}$ analysis

Model	$f_+(0)$ prediction	$ V_{cb} f_+(0) \times 10^3$	$ V_{cb} \times 10^3$
WSB ²¹	0.70	$25.7 \pm 1.4 \pm 1.7$	$37.3 \pm 2.0 \pm 2.5$
KS ²²	0.69	$25.7 \pm 1.4 \pm 1.7$	$36.7 \pm 2.0 \pm 2.5$
Demchuk ^{†23}	0.68	$24.8 \pm 1.1 \pm 1.6$	$36.4 \pm 1.6 \pm 2.4$
Average			$36.9 \pm 3.7 \pm 0.5$

† A smaller statistical error is quoted for this model because M_V is specified.

For the average value for V_{cb} , the first error is the quadrature of the the systematic and statistical errors in the data, and the fact that the fraction of B^o 's produced in $\Upsilon(4S)$ decay is known only as 0.49 ± 0.05 .²⁴ The second error is due only to the model dependence.

2.3.3. Branching Ratio of $\bar{B}^o \rightarrow D^{*+} \ell^- \bar{\nu}$

We next turn to measurements of the branching ratio of the pseudoscalar to vector transition $\bar{B}^o \rightarrow D^{*+} \ell^- \bar{\nu}$, shown in Table 4.

Table 4. Measurements of $\mathcal{B}(\bar{B}^o \rightarrow D^{*+} \ell^- \bar{\nu})$

Experiment	$\mathcal{B}(\%)$
CLEO ²⁵	$4.1 \pm 0.5 \pm 0.7$
ARGUS ²⁶	$4.7 \pm 0.6 \pm 0.6$
CLEO II ²⁴	$4.50 \pm 0.44 \pm 0.44$
ALEPH ²⁷	$5.18 \pm 0.30 \pm 0.62$
DELPHI ²⁸	$5.47 \pm 0.16 \pm 0.67$
Average	4.90 ± 0.35

The width predictions of a collection of representative models and the resulting values of V_{cb} are given in Table 5. Here the first error on the average is the from the error on the measured branching ratio ($\pm 3.6\%$) in quadrature with the error on the lifetime ($\pm 1.6\%$) and the second error reflects the spread in the models ($\pm 5.2\%$).

2.3.4. Heavy Quark Effective Theory and $\bar{B} \rightarrow D^* \ell^- \bar{\nu}$

Our next method for finding V_{cb} uses ‘‘Heavy Quark Effective Theory’’ (HQET).³² We start with a quick introduction to this theory. It is difficult to solve QCD at long distances, but its possible at short distances. Asymptotic freedom, the fact that the strong coupling constant α_s becomes weak in processes with large q^2 , allows perturbative calculations. Large distances are of the order $\sim 1/\Lambda_{QCD} \sim 1$ fm, since Λ_{QCD} is about 0.2 GeV. Short distances, on the other hand, are of the order of the

Table 5. Values of V_{cb} from $\mathcal{B}(\bar{B}^0 \rightarrow D^+ \ell^- \bar{\nu})$

Model	Predicted $\Gamma(B \rightarrow D^* \ell \nu)$ (ps^{-1})	$ V_{cb} \times 10^3$
ISGW ²⁹	$25.2 V_{cb} ^2$	35.2 ± 1.4
ISGW II ³⁰	$24.8 V_{cb} ^2$	35.5 ± 1.4
KS ²²	$25.7 V_{cb} ^2$	34.8 ± 1.4
WBS ²¹	$21.9 V_{cb} ^2$	37.8 ± 1.5
Jaus1 ³¹	$21.7 V_{cb} ^2$	37.9 ± 1.5
Jaus2 ³¹	$21.7 V_{cb} ^2$	37.9 ± 1.5
Average		$36.5 \pm 1.5 \pm 1.9$

quark Compton wavelength; $\lambda_Q \sim 1/m_Q$ equals 0.04 fm for the b quark and 0.13 fm for the c quark.

For hadrons, on the order of 1 fm, the light quarks are sensitive only to the heavy quark's color electric field, not the flavor or spin direction. Thus, as $m_Q \rightarrow \infty$, hadronic systems which differ only in flavor or heavy quark spin have the same configuration of their light degrees of freedom. The following two predictions follow immediately (the actual experimental values are shown below):

$$m_{B_s} - m_{B_d} = m_{D_s} - m_{D^+} \quad (20)$$

$$(90 \pm 3) \text{ MeV} \quad (99 \pm 1) \text{ MeV} , \text{ and}$$

$$m_{B^*}^2 - m_B^2 = m_{D^*}^2 - m_D^2. \quad (21)$$

$$0.49 \text{ GeV}^2 \quad 0.55 \text{ GeV}^2.$$

The agreement is quite good but not exceptional. Since the charmed quark is not that heavy, there is some heavy quark symmetry breaking. This must be accounted for in quantitative predictions, and can probably explain the discrepancies above. The basic idea is that if you replace a b quark with a c quark moving at the same **velocity**, there should only be small and calculable changes.

In lowest order HQET there is only one form-factor function ξ which is a function of the Lorentz invariant four-velocity transfer y , where

$$y = \frac{M_B^2 + M_{D^*}^2 - q^2}{2M_B M_{D^*}}. \quad (22)$$

The point y equals one corresponds to the situation where the B decays to a D^* which is at rest in the B frame. Here the ‘‘universal’’ form-factor function $\xi(y)$ has the value, $\xi(1) = 1$, in lowest order. This is the point in phase space where the b quark changes to a c quark with zero velocity transfer. The idea is to measure the decay rate at this point, since we know the value of the form-factor, namely unity, and then apply the hopefully small and hopefully well understood corrections. Although this analysis can be applied to $\bar{B} \rightarrow D \ell^- \nu$, the vanishing of the decay rate at y equals 1, (maximum q^2 , see Fig. 12), makes this inaccurate.²⁰

The corrections are of two types: quark mass, characterized as some coefficient times Λ_{QCD}/m_Q , and hard gluon, characterized as η_A . The value of the form-factor can then be expressed as³³

$$\xi(1) = \eta_A \left(1 + 0 \cdot \Lambda_{QCD}/m_Q + c_2 \cdot (\Lambda_{QCD}/m_Q)^2 + \dots \right) = \eta_A(1 + \delta). \quad (23)$$

The zero coefficient in front of the $1/m_Q$ term reflects the fact that the first order correction in quark mass vanishes at y equals one. This is called Luke's Theorem.³⁴ Recent estimates are 0.96 ± 0.007 and -0.55 ± 0.025 for η_A and δ , respectively. The value predicted for $\xi(1)$ then is 0.91 ± 0.03 . This is the conclusion of Neubert.³³ There has been much controversy surrounding the theoretical prediction of this number.³⁵

To find the value of the decay width at y equals one, it is necessary to fit data over a finite range in y and extrapolate to y of one. HQET does not predict the shape of the form-factor; hence the shape of the $d\Gamma/dy$ distribution is not specified. Most experimental groups have done the simplest thing and used a linear fit. The CLEO results with both linear and quadratic fits are shown in Fig. 13. The results from the different groups are summarized in Table 6. Also fits of the slope parameter, ρ^2 , coming from the linear fit are included.

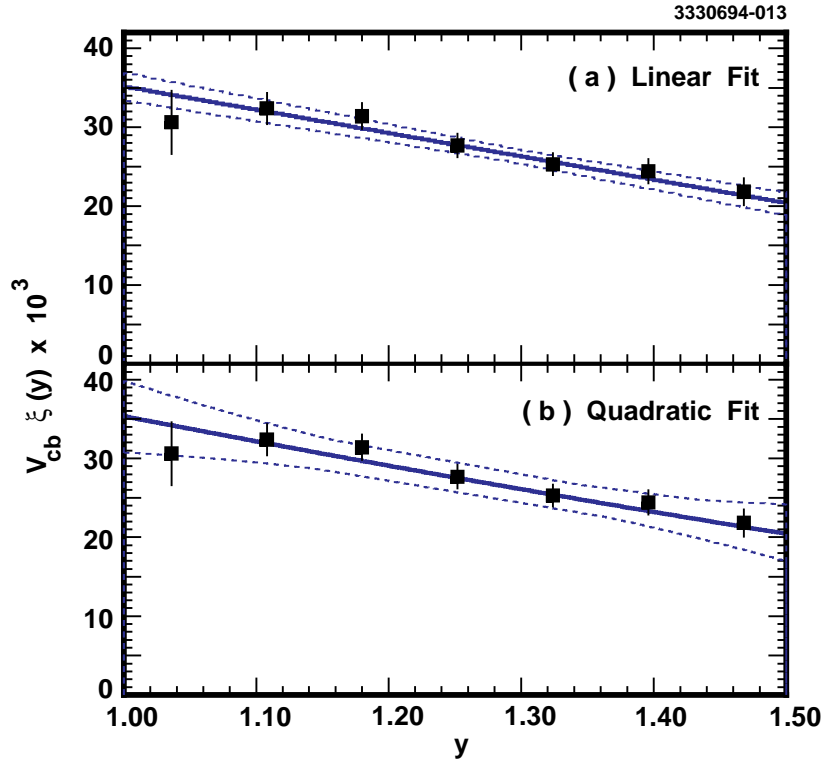


Fig. 13. Linear and quadratic fits to the CLEO data for the $D^{*+} \ell^- \bar{\nu}$ and $D^{*0} \ell^- \bar{\nu}$.

Although the shape of the function is not specified in HQET general considerations lead to the expectation that the slope is positive: there is a pole in the amplitude

Table 6. Values of $|V_{cb}|\xi(1) \times 10^3$

Experiment	$ V_{cb} \xi(1) \times 10^3$	ρ^2
ARGUS ³⁶	$38.8 \pm 4.3 \pm 3.5$	$1.17 \pm 0.22 \pm 0.06$
CLEO II ³⁷	$35.1 \pm 1.9 \pm 2.0$	$0.84 \pm 0.12 \pm 0.08$
ALEPH ³⁸	$31.4 \pm 2.3 \pm 2.5$	$0.39 \pm 0.21 \pm 0.12$
DELPHI ³⁹	$35.0 \pm 1.9 \pm 2.3$	$0.81 \pm 0.16 \pm 0.10$
Average	34.6 ± 1.6	0.82 ± 0.09

as $y \rightarrow -1$ and $\xi(y) \rightarrow 0$ as y increases. Shapes for $\xi(y)$ are suggested by quark models. I have fit the CLEO data to different model functions as shown in Fig. 14. The results are shown in Table 7.

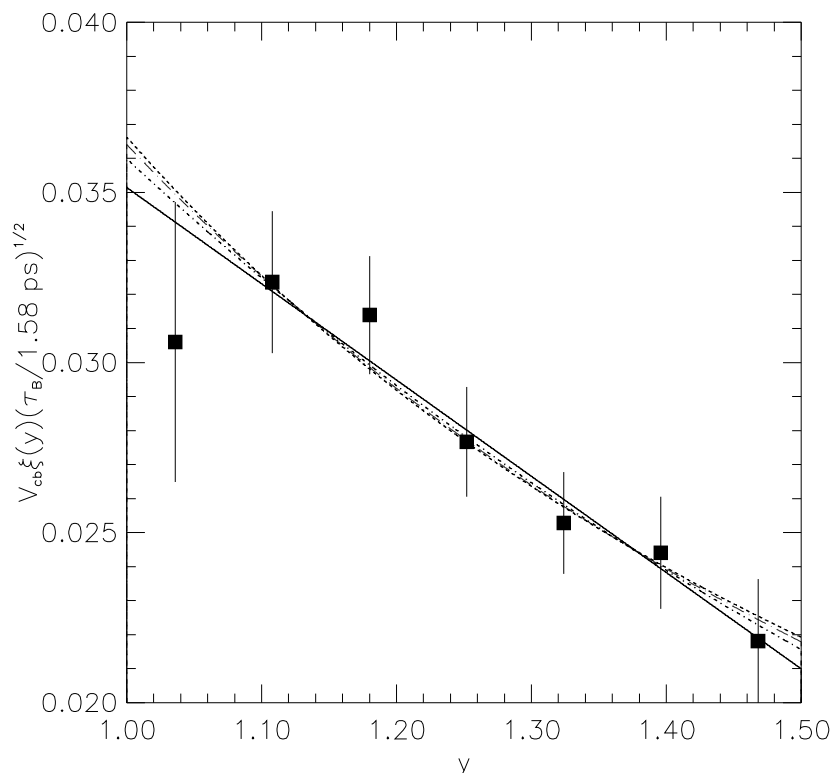


Fig. 14. Fits to the CLEO data with different shapes. The curves are linear (solid), Neubert-Reickert (NR) exponential (dashed), pole (long dash-dot) and exponential (dot-dashed).

These shapes give larger values of $|V_{cb}|\xi(1)|$ than the linear fit by $(5 \pm 3)\%$. I call this a model dependent error. The value then obtained for $|V_{cb}|\xi(1)|$ is $(36.3 \pm 1.6 \pm 1.0) \times 10^{-3}$, and

$$|V_{cb}| = 0.0397 \pm 0.0021 \pm 0.0017 \quad . \quad (24)$$

Table 7. Values of $|V_{cb}|\xi(1)$ for different fit shapes of CLEO II data

$\xi(y)$	name	ρ	$ V_{cb} \xi(1) \times 10^3$
$1 - \rho^2(y - 1)$	linear	0.90 ± 0.07	$0.0351 \pm 0.0018 \pm 0.0018$
$\frac{2}{y+1} \exp\left[-(2\rho^2 - 1)\frac{y-1}{y+1}\right]$	NR exp	0.90 ± 0.12	$0.0366 \pm 0.0024 \pm 0.0018$
$\left(\frac{2}{y+1}\right)^{2\rho^2}$	pole	1.07 ± 0.11	$0.0364 \pm 0.0023 \pm 0.0018$
$\exp[-\rho^2(y - 1)]$	exp	1.01 ± 0.10	$0.0360 \pm 0.0022 \pm 0.0018$

2.3.5. $|V_{cb}|$ using inclusive semileptonic decays

The inclusive semileptonic branching ratio can also be used to measure V_{cb} . While $\mathcal{B}(B \rightarrow Xe^- \bar{\nu})$ this has traditionally been done by measuring the inclusive lepton momentum spectrum using only single lepton data, recently dilepton data have been used. The inclusive lepton spectrum from the latest CLEO II data⁴⁰ is shown in Fig. 15. Both electrons and muons are shown. Leptons which arise from the contin-

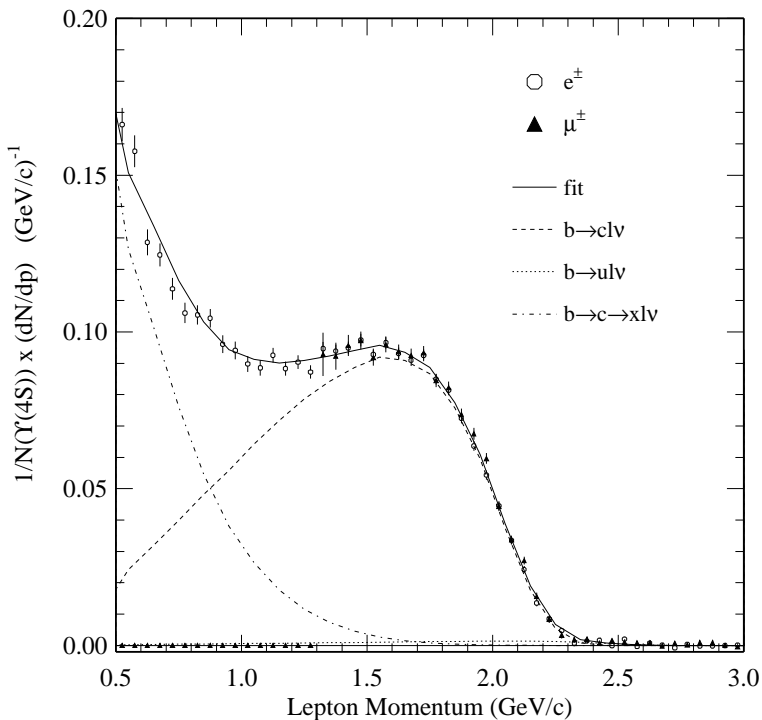


Fig. 15. Fit to the CLEO inclusive lepton spectrum with the ACM model.

uum have been statistically subtracted using the below resonance sample. The peak at low momentum is due to the decay chain $\bar{B} \rightarrow DX$, $D \rightarrow Y\ell^+\nu$. The data are fit to two shapes whose normalizations are allowed to float. The first shape is taken from models of B decay while the second comes from the measured shape of leptons from D mesons produced nearly at rest at the ψ'' , which is then smeared using the measured

momentum distribution of D 's produced in B decay. CLEO finds \mathcal{B}_{sl} of $10.5 \pm 0.2\%$ and $11.1 \pm 0.3\%$ in the ACM⁴³ and ISGW* models, respectively.⁴⁰ The ACM model will be described below. The ISGW* model is a variant of the ISGW²⁹ model. The ISGW model includes all the exclusive single hadron modes, D , D^* , and D^{**} which contains several components. CLEO lets the normalization of the D^{**} components float in the fit, and calls this model ISGW*.

Next, I discuss how to use dilepton events to eliminate the secondary leptons at low momentum. Consider the sign of the lepton charges for the four leptons in the following decay sequence: $\Upsilon(4S) \rightarrow B^- B^+$; $B^- \rightarrow D \ell_1^- \bar{\nu}$, $B^+ \rightarrow \bar{D} \ell_3^+ \nu$; $D \rightarrow Y \ell_2^+ \nu$, $\bar{D} \rightarrow Y' \ell_4^- \bar{\nu}$. If a high momentum negative lepton (ℓ_1^-) is found, then if the second lepton is also negative it must come from the cascade decay of the B^+ (i.e. it must be ℓ_4^-). On the other hand the second lepton being positive shows that it must be either the primary lepton from the opposite B^+ , (ℓ_3^+), or the cascade from the same B^- , (ℓ_2^+). However the cascades from the same B^- can be greatly reduced by insisting that the cosine of the opening angle between the two leptons be greater than zero as they tend to be aligned. The same arguments are applicable to $\Upsilon(4S) \rightarrow B^0 \bar{B}^0$, except that an additional correction must be made to account for $B\bar{B}$ mixing.

The CLEO II data are shown in Fig. 16. The data fit nicely to either the ACM or ISGW* model. They find that the semileptonic branching ratio, \mathcal{B}_{sl} , equals $(10.36 \pm 0.17 \pm 0.40)\%$ with a negligible dependence on the model.⁴¹ This result confirms that the B model shapes are appropriate down to lepton momenta of $0.6 \text{ GeV}/c$. ARGUS⁴² did the first analysis using this technique and found $\mathcal{B}_{sl} = (9.6 \pm 0.5 \pm 0.4)\%$.

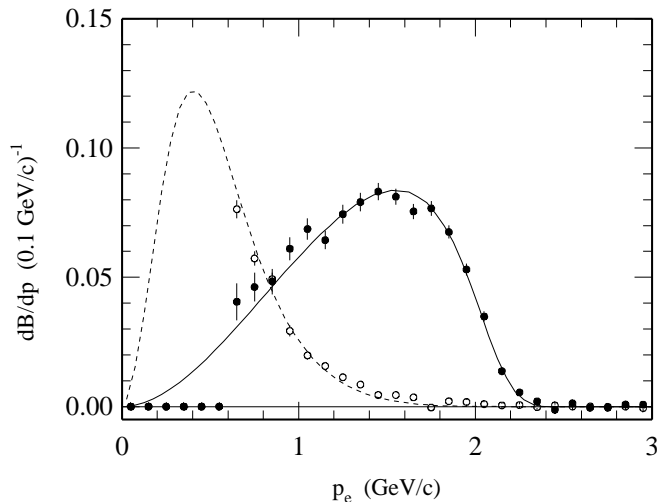


Fig. 16. The lepton momentum spectrum in dilepton events from CLEO. The solid points are for opposite sign leptons, while the open circles indicate like sign lepton pairs. The fit is to the ACM model.

The next topic is to measure V_{cb} using the inclusive lepton spectrum. Consider

$\Gamma_{sl} \equiv \Gamma(B \rightarrow X e^{-} \bar{\nu})$ in the simplest parton model:

$$\Gamma_{sl} = \frac{G_F^2 m_b^5}{192\pi^3} (p_c |V_{cb}|^2 + p_u |V_{ub}|^2) \eta_{QCD}, \quad (25)$$

where the p 's are phase space factors, and the QCD correction, $\eta_{QCD} = 1 - 2\alpha_s/3\pi$. Since $|V_{ub}| \ll |V_{cb}|$, we ignore the 2nd term. To use the semileptonic width to extract $|V_{cb}|$ using this expression requires a knowledge of m_b^5 , which is poorly understood. A way around this dilemma was found by Altarelli et al.⁴³ They make two important corrections to the simple parton model. First they treat the spectator quark in the B meson as a quasi-free particle with a Gaussian spectrum of Fermi-momentum, p :

$$f(p) = \frac{4p^2}{\sqrt{\pi} p_f^3} \exp(-p^2/p_f^2). \quad (26)$$

The average value, p_f , is a free parameter in the model. Secondly, they include the effects of gluon radiation from the quarks, which lowers the spectrum at high lepton momentum. The semileptonic width is given explicitly as:

$$\frac{d\Gamma(B \rightarrow DX \ell^{-} \bar{\nu})}{dx} = \frac{m_b^5 G_F^2 V_{cb}^2}{96\pi^3} \cdot [\Phi(x, \epsilon) - G(x, \epsilon)], \quad (27)$$

where $x = 2E_\ell/m_b$, E_ℓ being the lepton energy, $\epsilon = m_c/m_b$, $G(x, \epsilon)$ is a complicated gluon radiation function and

$$\Phi(x, \epsilon) = \frac{x^2(1 - \epsilon^2 - x)^2}{(1 - x)^3} [(1 - x)(3 - 2x) + (3 - x)\epsilon^2]. \quad (28)$$

Each value of the Fermi-momentum, p , leads to a different value of m_b and hence a different distribution for $\frac{d\Gamma}{dx}$ which must be convoluted with Eq. (27) to find the total theoretical lepton momentum spectrum. The relationship between m_b and p is just given by kinematics

$$m_b^2 = m_B^2 + m_{sp}^2 - 2m_B \sqrt{(p^2 + m_{sp}^2)}. \quad (29)$$

Here m_B is the known value of the B meson mass of 5.280 GeV and m_{sp} is the spectator quark mass. A fit to the shape of the lepton energy spectrum then is needed to determine the free parameters p_f , ϵ and m_{sp} . It turns out that one can fix m_{sp} and any latent dependence is absorbed by the other two. So a fit to the data will determine \mathcal{B}_{sl} , p_f and ϵ . In this way Altarelli et al. remove the explicit dependence of the m_b^5 term in the total decay rate. The ISGW and ISGW* models are also used. The resulting values are given in Table 8.

The representative value of $|V_{cb}|$ found from this analysis alone is

$$|V_{cb}| = 0.039 \pm 0.001 \pm 0.004 \quad . \quad (30)$$

Table 8. V_{cb} Values from Inclusive leptons

Model	Experiment	V_{cb}
ACM	CLEO I	$0.042 \pm 0.002 \pm 0.004$
ACM	ARGUS	$0.039 \pm 0.001 \pm 0.003$
ACM	CLEO II	$0.040 \pm 0.001 \pm 0.004$
ISGW	CLEO I	$0.039 \pm 0.002 \pm 0.004$
ISGW	ARGUS	$0.039 \pm 0.001 \pm 0.005$
ISGW	CLEO II	$0.040 \pm 0.001 \pm 0.004$
ISGW*	CLEO I	$0.037 \pm 0.002 \pm 0.004$
ISGW*	CLEO II	$0.040 \pm 0.002 \pm 0.004$

There are determinations of the inclusive B semileptonic branching ratio from LEP. These measurements average over more B species than at the $\Upsilon(4S)$. Since the lifetimes of some of these, especially the Λ_b appears to be shorter than for the ground state mesons, the semileptonic branching ratio measured at LEP should be lower than that measured on the $\Upsilon(4S)$, yet it is somewhat higher.⁴⁴ Since the measurement at LEP is far more complicated, I have chosen to leave out these results.

The results of using all four methods to find V_{cb} are shown in Fig. 17. It is remarkable that all four separate methods give such consistent results. Advocates for any particular method can choose among these results. I have chosen to average them. The errors are handled by adding the statistical and systematic errors on each method and then adding the different methods in quadrature. This should give a generous estimate of the final error. The average value of V_{cb} is 0.0381 ± 0.0021 , which gives a value for the CKM parameter

$$A = 0.784 \pm 0.043 \quad . \quad (31)$$

2.4. The CKM element V_{ub}

The first evidence of a non-zero value of V_{ub} was obtained by CLEO I who saw a non-zero excess beyond the endpoint allowed for $B \rightarrow D\ell\nu$ transitions.⁴⁵ This result was quickly confirmed by ARGUS.⁴⁶ The latest evidence from CLEO II⁴⁷ is shown in Fig. 18. R_2 is the second Fox-Wolfram event shape variable,⁴⁸ which tends to zero for spherical events, such as $\Upsilon(4S)$ decays and to one for jet-like events. P_{miss} is the missing momentum in the event.

The branching ratios are small. CLEO finds that the rate in the lepton momentum interval $2.6 > p_\ell > 2.4$ GeV/c, $\mathcal{B}_u(p)$, is $(1.5 \pm 0.2 \pm 0.2) \times 10^{-4}$. To extract V_{ub} from this measurement we need to use theoretical models. It is convenient to define: $\Gamma(b \rightarrow u\ell\nu) = \gamma_u |V_{ub}|^2$, and $\Gamma(b \rightarrow c\ell\nu) = \gamma_c |V_{cb}|^2$. In addition, $f_u(p)$ is the fraction of the spectrum predicted in the end point region by different models, and \mathcal{B}_{sl} is the

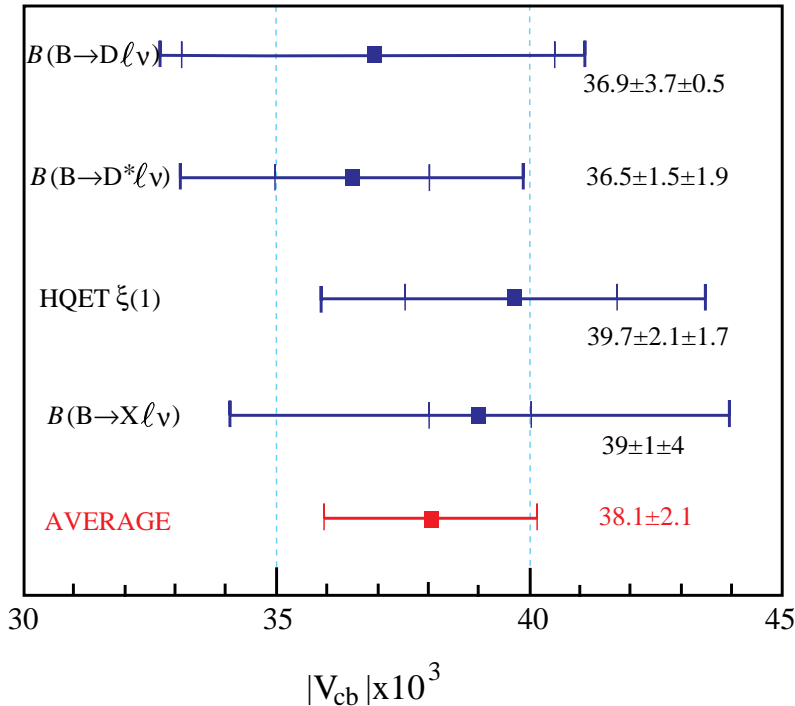


Fig. 17. Results of four different methods used to evaluate V_{cb} , and the resulting average. The horizontal lines show the values, the statistical errors out to the thin vertical lines, and the systematic errors added on linearly out to the thick vertical lines.

semileptonic branching ratio. Then:

$$\frac{|V_{ub}|^2}{|V_{cb}|^2} = \frac{\mathcal{B}_u(p)}{\mathcal{B}_{sl}} \cdot \frac{\gamma_c}{f_u(p)\gamma_u}. \quad (32)$$

These models disagree as to which final states populate the endpoint region. Most models agree roughly on values of γ_c . However, models differ greatly in the value of the product $\gamma_u \cdot f_u(p)$. There are two important reasons for these differences. First of all, different authors disagree as to the importance of the specific exclusive final states such as $\pi \ell \nu$, $\rho \ell \nu$ in the lepton endpoint region. For example, the Altarelli et al. model doesn't consider individual final states and thus can be seriously misleading if the endpoint region is dominated by only one or two final states. In fact, several inventors of exclusive models have claimed that the endpoint is dominated by only a few final states.^{29,21} Secondly, even among the exclusive form-factor models there are large differences in the absolute decay rate predictions. This is illustrated in Fig. 19. The differences in the exclusive models are much larger in $b \rightarrow u$ transitions than in $b \rightarrow c$ transitions because the q^2 range is much larger.

Artuso has explicitly shown that the q^2 distributions were very different in the ACM and original ISGW model.⁴⁹ However, the new ISGW II model agrees much better with ACM (see Fig. 20).⁵⁰

Measurement of exclusive charmless semileptonic decays can put constraints on

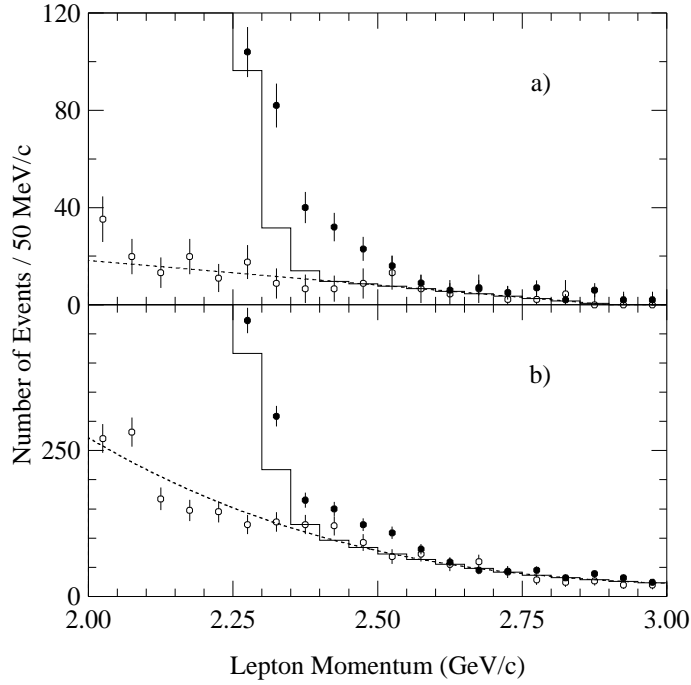


Fig. 18. Lepton yield versus momentum from CLEO II for the “strict” cut sample, $R_2 < 0.2$, $P_{miss} > 1$ GeV/c and the lepton and missing momentum direction point into opposite hemispheres, (a) and the $R_2 < 0.3$ sample (b). The filled points are from data taken on the peak of the $\Upsilon(4S)$, while the open points are continuum data scaled appropriately. The dashed curves are fits to the continuum data, while the solid histograms are predictions of the sum of $b \rightarrow c\ell\nu$ and continuum lepton production.

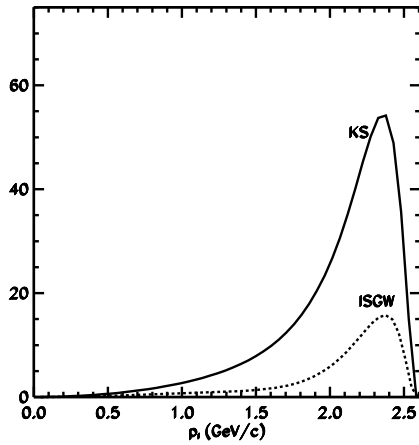


Fig. 19. Lepton momentum spectra, for $B \rightarrow \rho\ell\nu$ in the KS and the original ISGW model.

the models and therefore restrict the model dependence. In principle, the ratio of rates for $\pi\ell\nu$ and $\rho\ell\nu$ can be measured as well as the q^2 dependence of the form-factors. However, measurement of these rates is difficult. CLEO has recently succeeded in

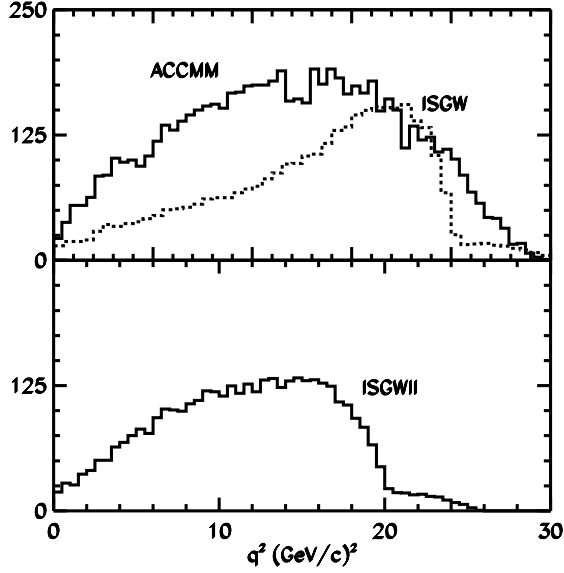


Fig. 20. q^2 distribution, for charmless semileptonic b decays in the model of Altarelli et al.(ACCMM) and the original ISGW model shown on top, and the new ISGW model shown on the bottom. The areas reflect the predicted widths, but the vertical scale is arbitrary. The high q^2 tails on the ISGW models arise from the $\pi\ell\nu$ final state.

measuring the branching ratios.⁵¹

A neutrino reconstruction technique is used. The neutrino energy and momentum is determined by evaluating the missing momentum and energy in the entire event:

$$E_{miss} = 2E_{beam} - \sum_i E_i \quad (33)$$

$$\vec{p}_{miss} = \sum_i \vec{p}_i \quad (34)$$

Criteria are imposed to guard against events with false large missing energies. First, the net charge is required to be zero. Secondly, events with two identified leptons (implying two neutrinos) are rejected. Leptons are required to have momenta greater than 1.5 GeV/c in the case of $\pi\ell\nu$ and greater than 2.0 GeV/c in the case of $\rho\ell\nu$. In addition, the candidate neutrino mass is calculated as

$$M_\nu^2 = E_{miss}^2 - \vec{p}_{miss}^2 \quad (35)$$

Candidate events containing a neutrino are kept if $M_\nu^2/2E_{miss} < 300$ MeV. Then the semileptonic B decay candidates $(\pi^0, \pi^+, \rho^0, \omega^0, \rho^+)\ell\nu$ are reconstructed using the neutrino four-vector found from the missing energy measurement.⁵³ The beam constrained invariant mass, M_{cand} is defined as

$$M_{cand}^2 = E_{beam}^2 - \left(\vec{p}_\nu + \vec{p}_\ell + \vec{p}_{(\pi \text{ or } \rho)} \right)^2, \quad (36)$$

and with the use of the neutrino four-vector is essentially the same as any other full B reconstruction analysis done at the $\Upsilon(4S)$. The M_{cand} distributions are shown in Fig. 21.

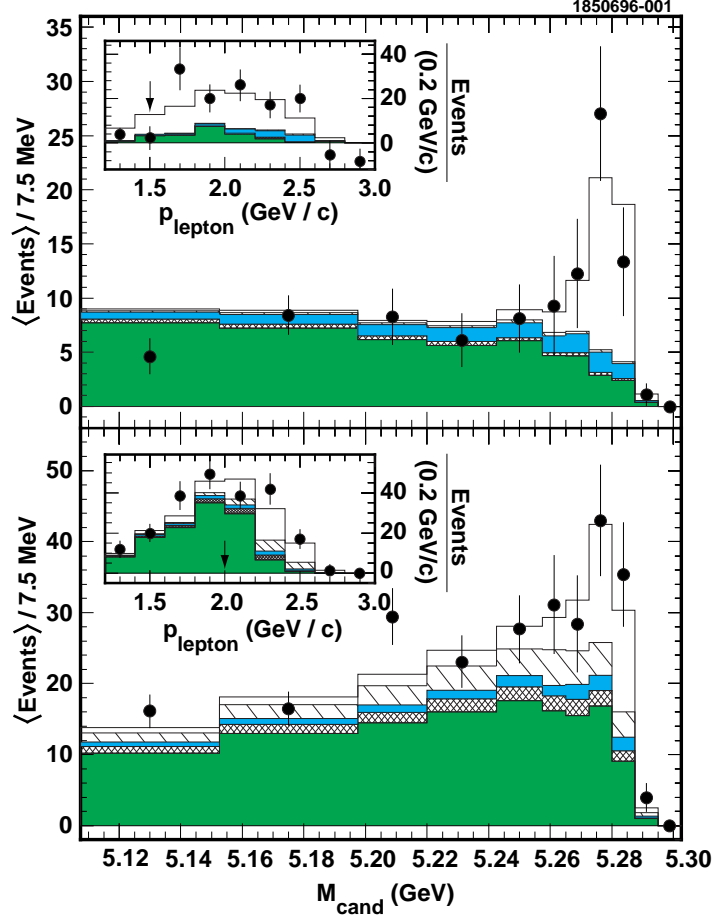


Fig. 21. The B candidate mass distributions, M_{cand} , for the sum of the scalar $\pi^+\ell\nu$ and $\pi^0\ell\nu$ (top) and the vector modes (ρ and ω) (bottom). The points are the data after continuum and fake background subtractions. The unshaded histogram is the signal, while the dark shaded shows the $b \rightarrow cX$ background estimate, the cross-hatched, estimated $b \rightarrow u\ell\nu$ feeddown. For the π (vector) modes, the light-shaded and hatched histograms are $\pi \rightarrow \pi$ (vector \rightarrow vector) and vector $\rightarrow \pi$ ($\pi \rightarrow$ vector) crossfeed, respectively. The insets show the lepton momentum spectra for the events in the B mass peak (the arrows indicate the momentum cuts).

It is often difficult to prove that a $\pi\pi$ system indeed is dominantly resonant ρ . CLEO attempts to show ρ dominance by plotting the $\pi^+\pi^-$ and $\pi^+\pi^0$ summed mass spectrum in Fig. 22. They also show a test case of $\pi^0\pi^0\ell\nu$, which cannot be ρ , since ρ^0 cannot decay to $\pi^0\pi^0$. There is an enhancement in the $\pi^+\pi^-$ plus $\pi^+\pi^0$ sum, while the $\pi^0\pi^0$ shows a relatively flat spectrum that is explained by background. The 3π spectrum shows little evidence of resonant ω , however. More data is needed to settle this issue. CLEO proceeds by assuming they are seeing purely resonant decays in the vector channel.

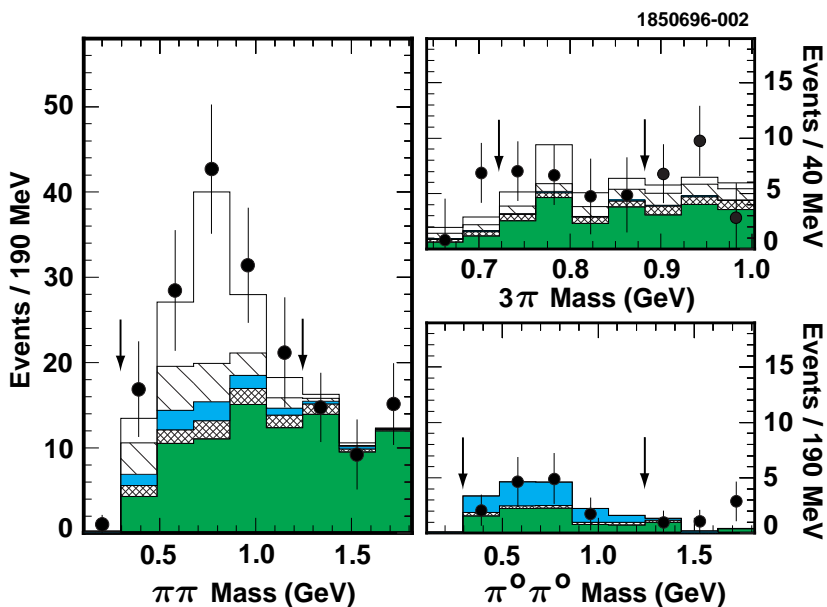


Fig. 22. Mass distributions for $\pi^+\pi^-$ plus $\pi^+\pi^0$ (left), 3π (upper right) and $\pi^0\pi^0$ (lower right), for events which are candidates $B \rightarrow x\ell\nu$ decays which satisfy all the other B candidate cuts including a cut on the B mass. The shading is the same as on the previous figure. The arrows indicate the mass range used in the analysis.

The measured branching ratio is model dependent due to different form-factor dependences on q^2 and lepton momentum. Therefore, CLEO reports different branching ratios for a selection of models. The ratio of $\rho\ell\nu/\pi\ell\nu$ is also given, see Table 9, and compared to model predictions; the errors are non-Gaussian, but the KS model has only a 0.5% likelihood of being consistent with the data.

The values of V_{ub} obtained from both the exclusive and the inclusive analyses are summarized in Fig. 23. For the inclusive analysis, results from CLEO I and ARGUS have been included in the average.⁵² Since the KS model predicts the wrong pseudoscalar/vector ratio, it is excluded from the average. The ISGW model has been dropped in favor of the ISGW II model. The range of model predictions is now narrowed compared to former analyses. However, the model variations still dominate the error. A conservative estimate gives

$$\left| \frac{V_{ub}}{V_{cb}} \right| = 0.080 \pm 0.015 \quad , \quad (37)$$

which provides a constraint

$$\left(\frac{1}{\lambda^2} \right) \left| \frac{V_{ub}}{V_{cb}} \right|^2 = (\rho^2 + \eta^2) = (0.36 \pm 0.07)^2 \quad . \quad (38)$$

Table 9. Results from exclusive semileptonic $b \rightarrow u$ transitions

Model	$\mathcal{B}(B \rightarrow \pi \ell \nu)$ $\times 10^4$	$\mathcal{B}(B \rightarrow \rho \ell \nu)$ $\times 10^4$	$\Gamma(\rho)/\Gamma(\pi)$	$\Gamma(\rho)/\Gamma(\pi)$ predicted
ISGW II	$2.0 \pm 0.5 \pm 0.3$	$2.2 \pm 0.4^{+0.4}_{-0.6}$	$1.1^{+0.5+0.2}_{-0.3-0.3}$	1.47
WSB	$1.8 \pm 0.5 \pm 0.3$	$2.8 \pm 0.5^{+0.5}_{-0.8}$	$1.6^{+0.7+0.3}_{-0.5-0.4}$	3.51
KS	$1.9 \pm 0.5 \pm 0.3$	$1.9 \pm 0.3^{+0.4}_{-0.5}$	$1.0^{+0.5+0.2}_{-0.3-0.3}$	4.55
Melikhov [†]	$1.8 \pm 0.4 \pm 0.3 \pm 0.2$	$2.8 \pm 0.5^{+0.5}_{-0.8} \pm 0.4$	$1.6^{+0.7+0.3}_{-0.5-0.4} \pm 0.11$	1.53 ± 0.15

[†] The 3rd error arises from uncertainties in the estimated form-factors

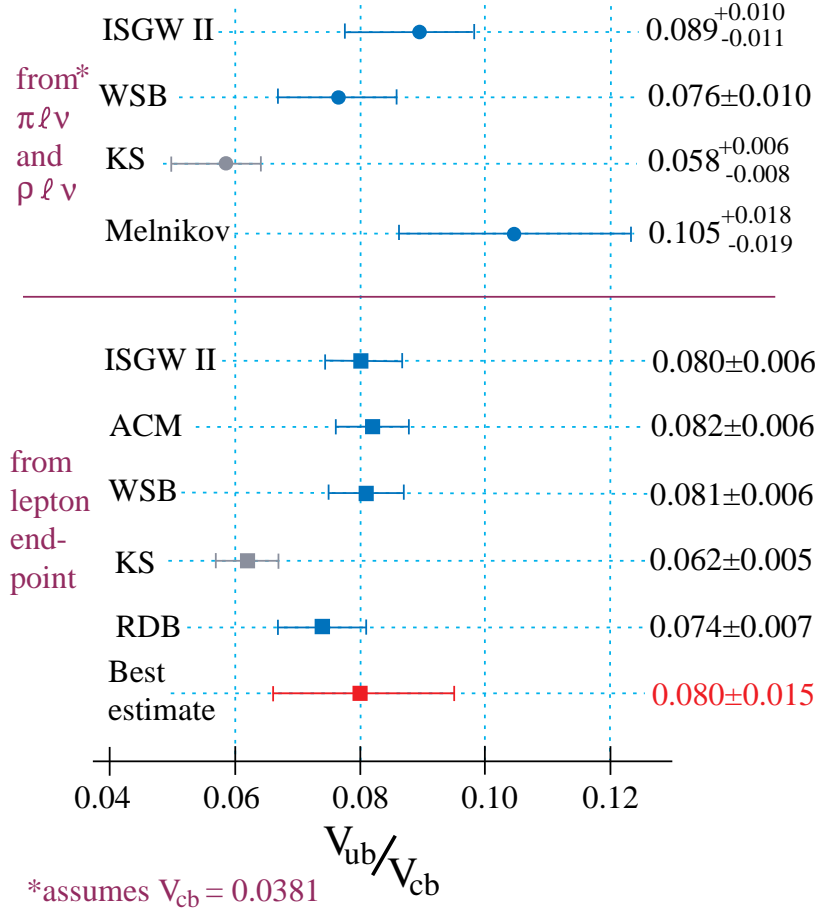


Fig. 23. Values of V_{ub}/V_{cb} obtained from the exclusive $\pi \ell \nu$ and $\rho \ell \nu$ analyses combined and taking $V_{cb} = 0.0381$, and results from the inclusive endpoint analysis. The best estimate combining all models except KS is also given.

2.5. $B_d^0 - \bar{B}_d^0$ Mixing

Neutral B mesons can transform to their anti-particles before they decay. The diagrams for this process are shown in Fig. 24. Although u , c and t quark exchanges

are all shown, the t quark plays a dominant role mainly due to its mass, as the amplitude of this process is proportional to the mass of the exchanged fermion. (We will discuss the phenomenon of mixing in more detail in section 3.2).

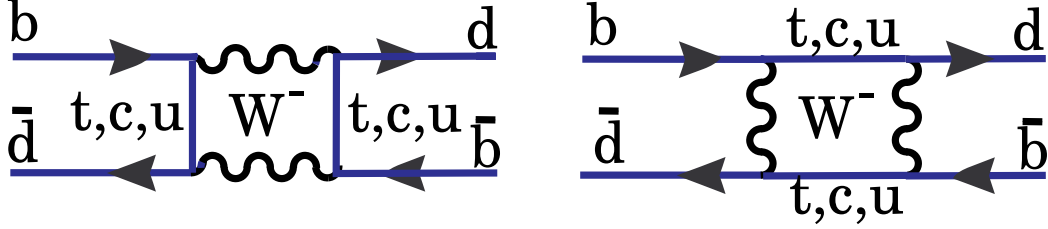


Fig. 24. The two diagrams for B_d mixing.

The probability of mixing is given by⁵⁴

$$x \equiv \frac{\Delta m}{\Gamma} = \frac{G_F^2}{6\pi^2} B_B f_B^2 m_B \tau_B |V_{tb}^* V_{td}|^2 m_t^2 F\left(\frac{m_t^2}{M_W^2}\right) \eta_{QCD}, \quad (39)$$

where B_B is a parameter related to the probability of the d and \bar{b} quarks forming a hadron and must be estimated theoretically, F is a known function which increases approximately as m_t^2 , and η_{QCD} is a QCD correction, with value about 0.8. By far the largest uncertainty arises from the unknown decay constant, f_B . B_d mixing was first discovered by the ARGUS experiment.⁵⁵ (There was a previous measurement by UA1 indicating mixing for a mixture of B_d^0 and B_s^0 .⁵⁶ At the time it was quite a surprise, since m_t was thought to be in the 30 GeV range. Since

$$|V_{tb}^* V_{td}|^2 \propto |(1 - \rho - i\eta)|^2 = (\rho - 1)^2 + \eta^2, \quad (40)$$

measuring mixing gives a circle centered at (1,0) in the $\rho - \eta$ plane.

The best recent mixing measurements have been done at LEP, where the time-dependent oscillations have been measured. The OPAL data⁵⁷ is shown in Fig. 25. Averaging over all LEP experiments $x=0.728 \pm 0.025$.⁵⁸

2.6. Rare B Decays

The term “rare B decays” is loosely defined. The spectator process shown in Fig. 26(a) is included since $b \rightarrow u$ doesn’t occur very often ($\approx 1\%$), and the mixing process which occurs often ($\approx 17\%$) is included since it involves two gauge bosons (the so called box diagram Fig. 26(b)). Other loop or box diagrams are shown in Fig. 26(d-f).

CLEO found the first unambiguous loop process, the one shown in Fig. 26(c).⁵⁹ These decays involving a loop diagram are sometimes called “penguins,” an indefensible if amusing term that was injected into the literature as a result of a bet. For the Standard Model to be correct these decays must exist. In fact, penguins are expected

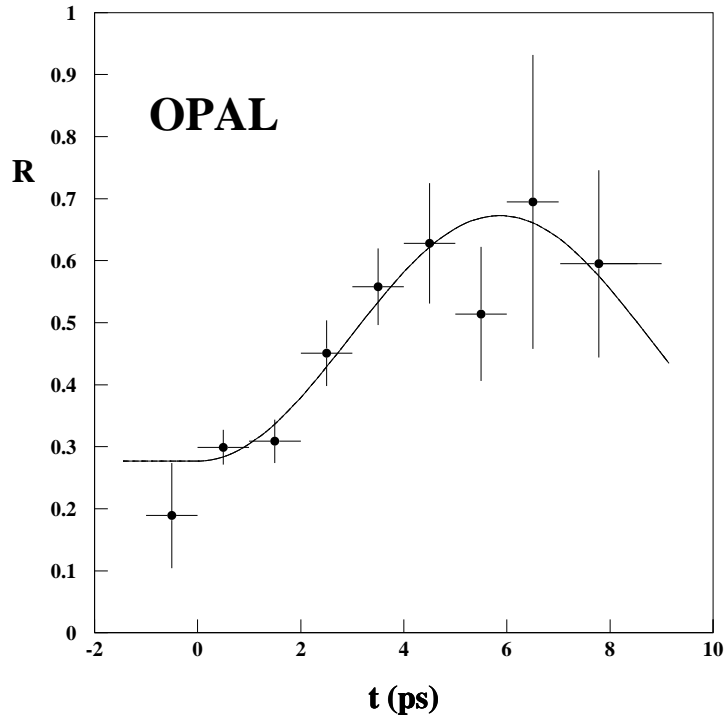


Fig. 25. The ratio, R , of like-sign to total events as a function of proper decay time, for selected $B \rightarrow D^{*+} X \ell^- \bar{\nu}$ events. The jet charge in the opposite hemisphere is used to determine the sign correlation. The curve is the result of a fit to the mixing parameter.

to play an important role in kaon decay, but there are no unique penguin final states in kaon decay. Since penguins are expected to be quite small in charm decay, it is only in B decay that penguins can clearly be discerned.

CLEO first found the exclusive final state $B \rightarrow K^* \gamma$. An updated value for the branching ratio is⁶⁰

$$\mathcal{B}(B \rightarrow K^* \gamma) = (4.2 \pm 0.8 \pm 0.6) \times 10^{-5} . \quad (41)$$

This analysis uses the standard B reconstruction technique, summarized in equation (11) used at the $\Upsilon(4S)$, combined with some additional background suppression cuts. These are separated into trying to insure that one is dealing with a real K^* and trying to suppress background leading to hard photons. The latter comes from initial state radiation (ISR), where one of the beams radiates a photon and then subsequently annihilates and from continuum quark-antiquark production ($Q\bar{Q}$). Suppression of ISR and $Q\bar{Q}$ is accomplished by combining event shape variables into a Fischer discriminant. A Fischer discriminant⁶¹ is a linear combination of several variables which individually may have poor separation between signal and background, but when taken together yield acceptable background rejection, the correlations between the variables helping. The Fischer output distribution for Monte Carlo simulations of

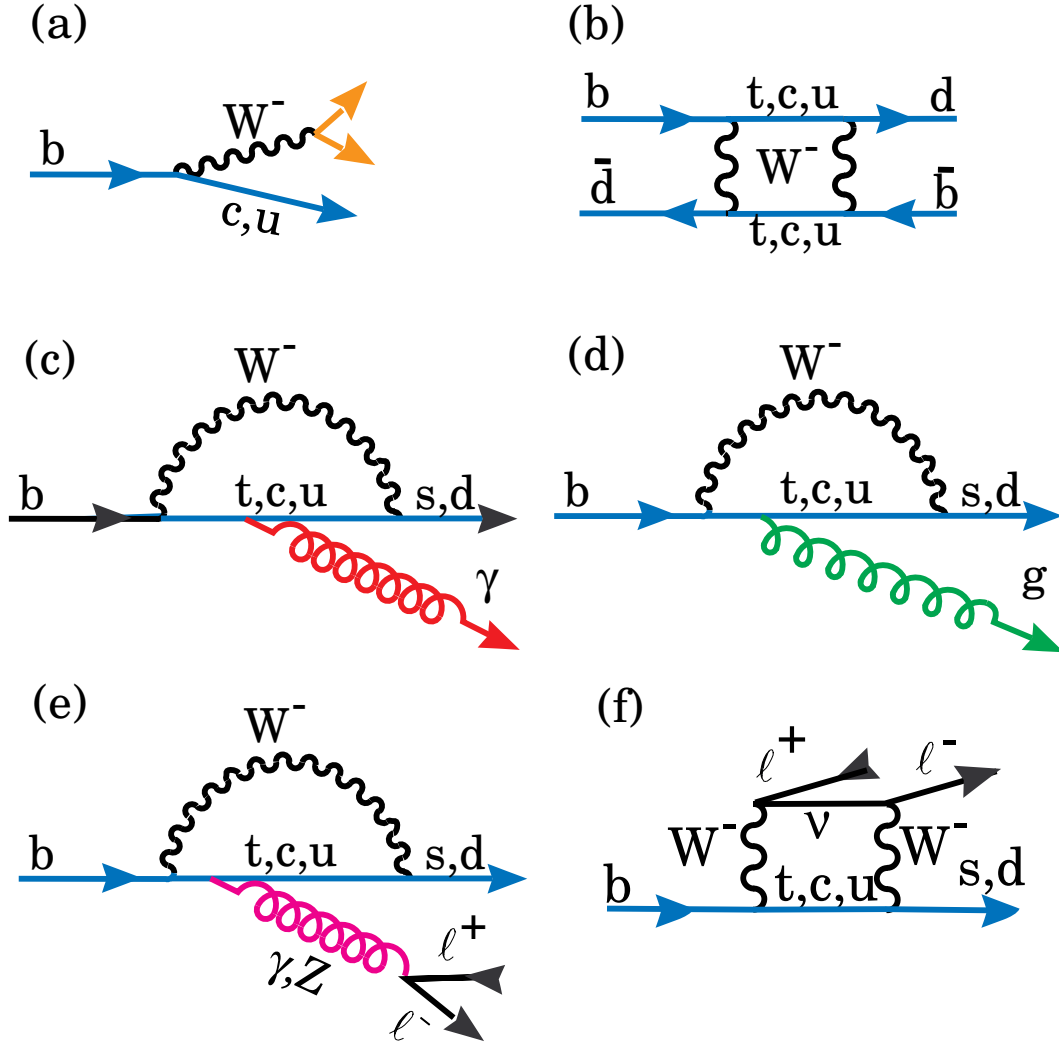


Fig. 26. A compendium of rare b decay diagrams. (a) The spectator diagram, rare when $b \rightarrow u$; (b) one of the mixing diagrams; (c) a radiative penguin diagram; (d) a gluonic penguin diagram; (e) and (f) are dilepton penguin diagrams.

signal, ISR and $Q\bar{Q}$ backgrounds are shown in Fig. 27.

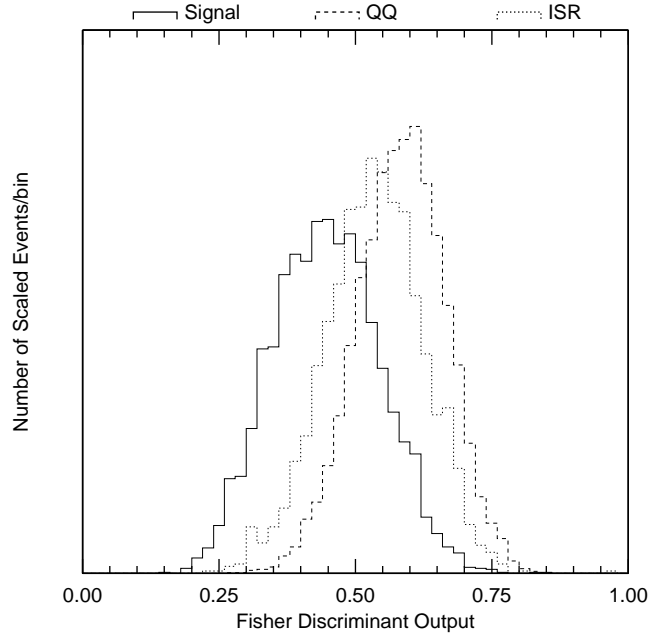


Fig. 27. The distribution of the Fischer discriminant output for Monte Carlo samples of $B^o \rightarrow K^{*o}\gamma(K^{*o} \rightarrow K^+\pi^-)$ signal, $Q\bar{Q}$ and ISR backgrounds. The histograms have equal area and the x axis has been rescaled to make the Fischer discriminant output lie between 0 and 1.

The branching ratio is extracted by making a maximum likelihood fit to four distributions, M_B , ΔE , the $K\pi$ invariant mass $m(K\pi)$, and the Fischer discriminant. To illustrate what the signal shapes look like, projection plots are made by applying restrictive selection criteria on three of the four likelihood variables and projecting the remaining events onto the axis of the fourth variable. This is shown for the $K^{*o} \rightarrow K^-\pi^+$ mode in Fig. 28.

The extraction of the inclusive rate for $b \rightarrow s\gamma$ is more difficult. There are two separate CLEO analyses.⁶² The first one measures the inclusive photon spectrum from B decay near the maximum momentum end, similar to what is done to extract an inclusive $b \rightarrow X\ell\nu$ signal, but with the additional problem that the expected branching ratio is much lower. The main problem is to reduce the ISR and $Q\bar{Q}$ backgrounds. Here instead of using a Fischer discriminant, a set of event shape variables and energies formed in a series of cones parallel and antiparallel to the candidate photon direction are fed into a neural net trained on Monte Carlo. The result is shown in Fig. 29(leftside).

The second technique constructs the inclusive rate by summing up the possible exclusive final states. Since the photons are expected to be at high momentum, and therefore take away up to half the B 's rest energy, the number of hadrons in the final state is quite limited. The analysis looks for the final states $B \rightarrow K n\pi\gamma$ where n is allowed to be a maximum of 4, but only one can be a π^o . Only one entry per event

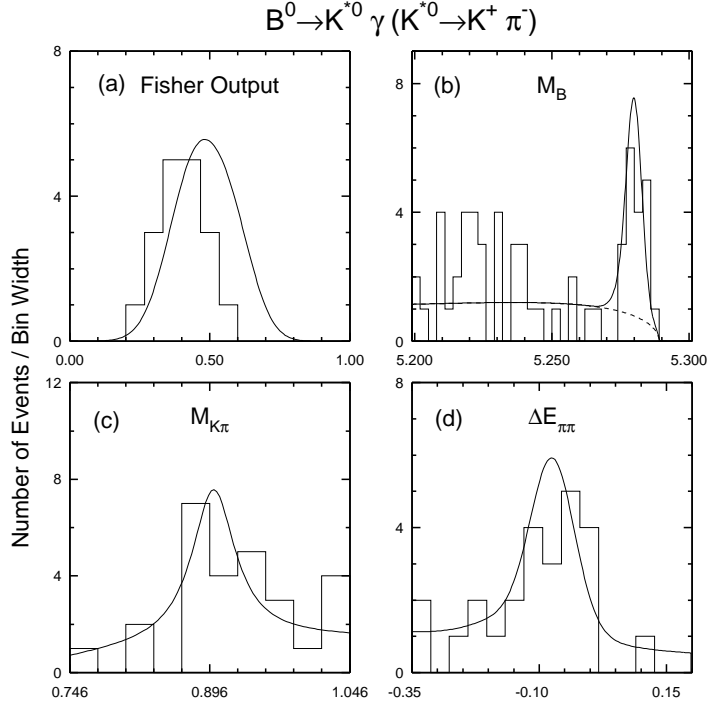


Fig. 28. Projections of $B^0 \rightarrow K^{*0} \gamma (K^{*0} \rightarrow K^+ \pi^-)$ data events (histograms) and maximum likelihood fits (curves) onto the four fit variables: (a) Fisher discriminant output, (b) M_B , (c) $M_{K\pi}$ and (d) $\Delta E_{\pi\pi}$, which is the difference between the candidate B energy and the beam energy assuming both charged tracks are pions.

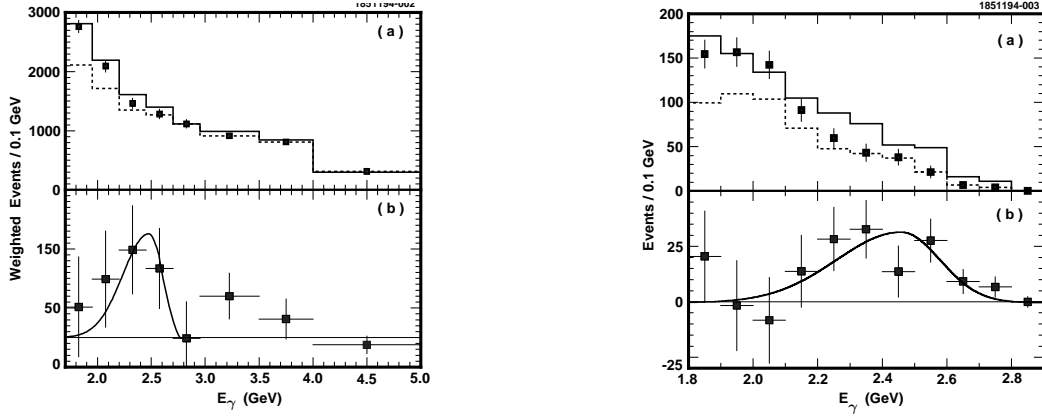


Fig. 29. Photon energy spectra from the neural net analysis shown on the left side, and from the B reconstruction analysis, shown on the right side. In (a) the on resonance data are the solid lines, the scaled off resonance data are the dashed lines, and the sum of backgrounds from off resonance data and $b \rightarrow c$ Monte Carlo are shown as the square points with error bars. In (b) the backgrounds have been subtracted to show the net signal for $b \rightarrow s \gamma$; the solid lines are fits of the signal using a spectator model prediction.

is allowed. Here background reduction is accomplished by using the full power of the exclusive B reconstruction analysis. The resulting γ energy spectrum is shown on the right side of Fig. 29.

The branching ratios found are $(1.88 \pm 0.74) \times 10^{-4}$ and $(2.75 \pm 0.67) \times 10^{-4}$ for the neural net and B reconstruction analyses, respectively. The average of the two results, taking into account the correlations between the two techniques is

$$\mathcal{B}(b \rightarrow s\gamma) = (2.3 \pm 0.5 \pm 0.4) \times 10^{-4} . \quad (42)$$

The theoretical prediction for the branching ratio is given by⁶³

$$\frac{\Gamma(b \rightarrow s\gamma)}{\Gamma(b \rightarrow c\ell\nu)} = \left| \frac{V_{ts}^* V_{tb}}{V_{cb}} \right| \frac{\alpha}{6\pi g(m_c/m_b)} |C_7^{eff}(\mu)|^2, \quad (43)$$

where $g(m_c/m_b)$ is a known function. While C_7 is calculated perturbatively at μ equal to the W mass, the evolution to b mass scale causes $\approx 25\%$ uncertainty in the prediction, since the proper point could be $m_b/2$ or $2m_b$. In the leading log approximation the theoretical prediction is $\mathcal{B}(b \rightarrow s\gamma) = (2.8 \pm 0.8) \times 10^{-4}$,⁶³ while an incomplete next to leading order calculation, gives $\sim 1.9 \times 10^{-4}$.⁶⁴ A recently completed next to leading order calculation gives 3.3×10^{-4} .⁶⁵ In all cases the data are consistent with the prediction.

The second analysis also produces the mass spectrum of the $K n\pi$ system, shown in Fig. 30. A clear $K^*(890)$ component is observed. The best way to measure the fraction of $K^*(890)$ is to divide the exclusive result by the average inclusive result. This number can test theoretical models, but mostly we are testing the prediction of the exclusive rate which is the far more difficult calculation than the inclusive rate.

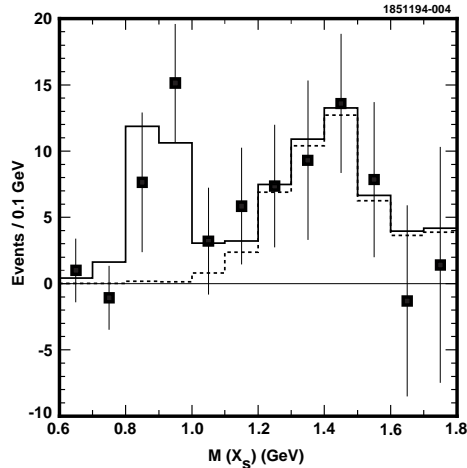


Fig. 30. The apparent $K n\pi$ mass distribution for the B reconstruction analysis. The points are the background subtracted data, not efficiency corrected, the solid histogram is fit to the data using several K^* resonance as input to a Monte Carlo simulation, while the dotted histogram shows all the fit components but the $K^*(890)$.

The CLEO result is⁶⁰

$$\frac{\Gamma(B \rightarrow K^* \gamma)}{\Gamma(b \rightarrow s \gamma)} = 0.181 \pm 0.068 \quad . \quad (44)$$

Model predictions vary between 4 and 40%.⁶⁸

Rare hadronic final states have also been measured. CLEO reported a signal in the sum of $K^\pm \pi^\mp$ and $\pi^+ \pi^-$ final states.⁶⁶ The particle identification could not uniquely separate high momentum kaons and pions. While the $K\pi$ mode results from a penguin diagram the $\pi\pi$ mode results mainly from a $b \rightarrow u$ spectator diagram. The reconstructed B mass plot is shown in Fig. 31, along with the results of several other searches from an updated analysis,⁶⁷ based on 2.4 fb⁻¹ of integrated luminosity on the $\Upsilon(4S)$. Here a best guess is made as to which final state is present. The resulting rate is

$$\mathcal{B}(B^o \rightarrow K^\pm \pi^\mp + \pi^+ \pi^-) = (1.8_{-0.5-0.3}^{+0.6+0.2} \pm 0.2) \times 10^{-5} \quad . \quad (45)$$

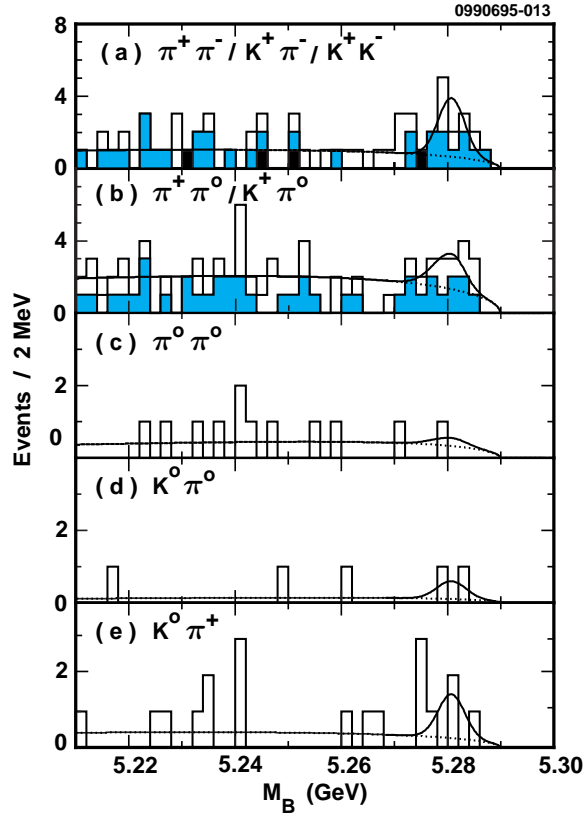


Fig. 31. M_B plots for (a) $B^o \rightarrow \pi^+ \pi^-$ (unshaded), $B^o \rightarrow K^+ \pi^-$, and $B^o \rightarrow K^+ K^-$ (black) (b) $B^+ \rightarrow \pi^+ \pi^o$ (unshaded) and $B^+ \rightarrow K^+ \pi^o$ (grey), (c) $B^o \rightarrow \pi^o \pi^o$, (d) $B^o \rightarrow K^o \pi^o$, and (e) $B^+ \rightarrow K^o \pi^+$. The projection of the total likelihood fit (solid curve) and the continuum background component (dotted curve) are overlaid.

An attempt to separate the kaon and pion components using the small difference in reconstructed energy and whatever particle identification power exists leads to the

dipion fraction shown in Fig. 32. The best current guess is that approximately half of the rate is due to $\pi^+\pi^-$.

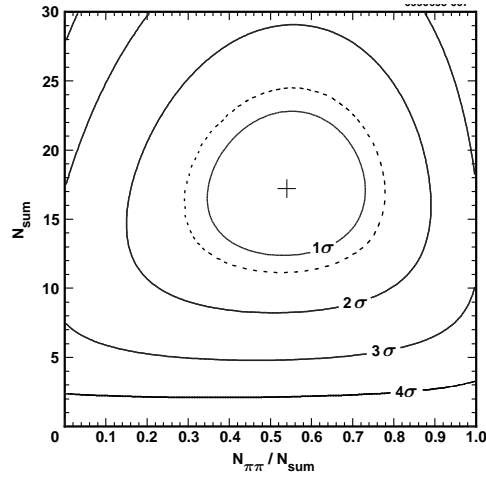


Fig. 32. The central value (+) of the likelihood fit to $N_{sum} \equiv N_{\pi\pi} + N_{K\pi}$ and the fraction $N_{\pi\pi}/N_{sum}$. The solid curves are the $n\sigma$ contours and the dotted curve is the 1.28σ contour.

CLEO also has found a signal in the sum of $\omega\pi^+$ and ωK^+ decays.⁶⁹ The B mass plot is shown in Fig. 33. The signal is 10 events observed on a background of 2 ± 0.3 events. The branching ratio is

$$\mathcal{B}(B^+ \rightarrow \omega\pi^+ + \omega K^+) = (2.8 \pm 1.0 \pm 0.5) \times 10^{-5} . \quad (46)$$

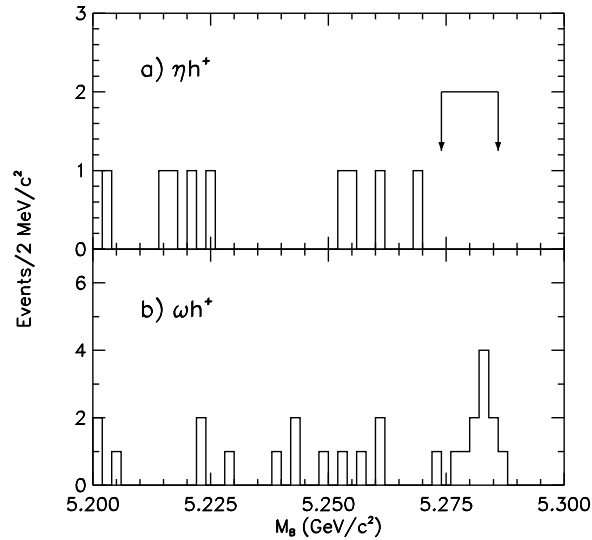


Fig. 33. The M_B projection for a) $B^+ \rightarrow \eta h^+$ and b) $B^+ \rightarrow \omega h^+$ after all other cuts, including the ΔE cut. The arrows indicate the signal region.

DELPHI also reports a signal of 11 “rare” events over a background of 1 event. The invariant mass plot is shown in Fig. 34.⁷⁰ One of these events appears to be

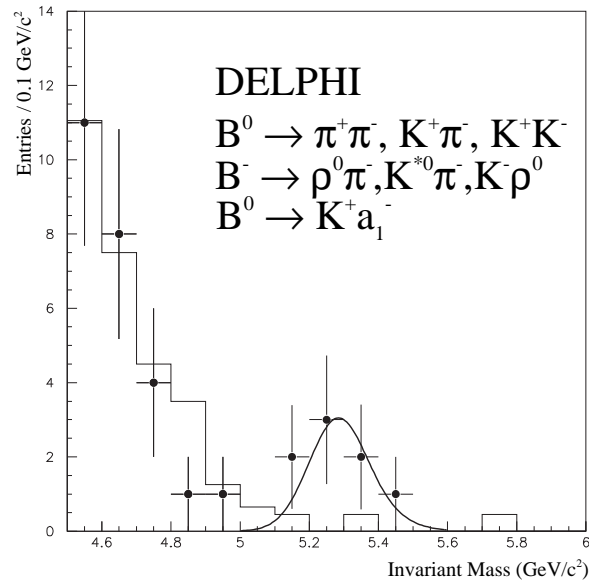


Fig. 34. Invariant mass distribution for two-body charmless hadronic B decays. The points with error bars represent the real data and the histograms the mass distributions expected in the absence of such decays as obtained from simulation. The curve represents the shape expected for the signal events normalized to the number of candidates selected in real data in the signal mass region.

uniquely identified as a $K^{*0}\pi^-$ final state and this then is an unambiguous hadronic penguin decay. The evidence is shown in Fig 35.

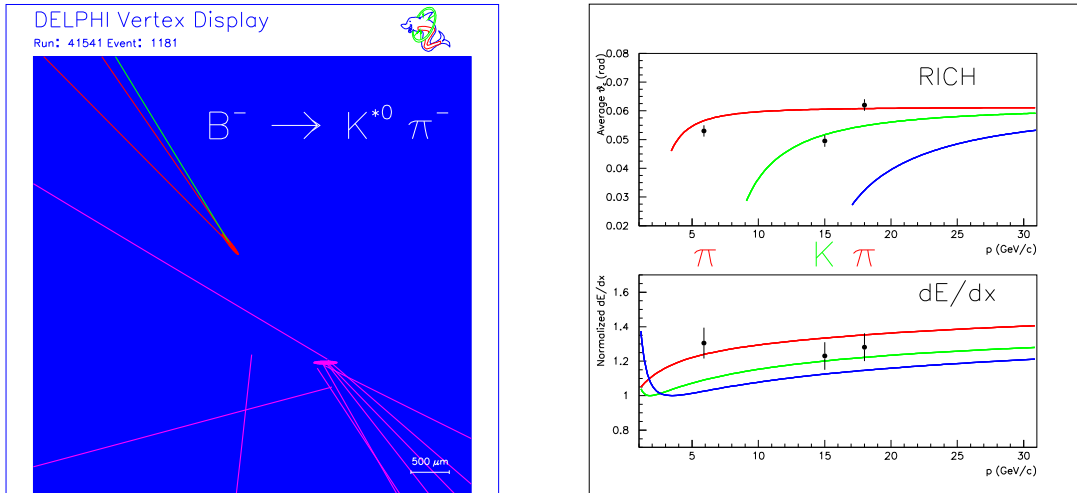


Fig. 35. The candidate $B^- \rightarrow K^{*0}\pi^-$ decay: a magnified view of the extrapolated tracks at the vertex is displayed above. The primary and secondary vertices are indicated by error ellipses corresponding to 3σ regions. The plot below summarizes the hadron identification properties. The lines represent the expected response to pions (upper), kaons (middle) and protons (lower), and the points with error bars the measured values for the reconstructed B decay products.

3. Importance of Further Study of B Decays

3.1. Tests of the Standard Model via the CKM triangle

The unitarity of the CKM matrix[†] allows us to construct six relationships. The most useful turns out to be

$$V_{ud}V_{td}^* + V_{us}V_{ts}^* + V_{ub}V_{tb}^* = 0 \quad . \quad (47)$$

To a good approximation

$$V_{ud} \approx V_{tb}^* \approx 1 \quad \text{and} \quad V_{ts}^* \approx -V_{cb}, \quad (48)$$

then

$$\frac{V_{ub}}{V_{cb}} + \frac{V_{td}^*}{V_{cb}} - V_{us} = 0 \quad . \quad (49)$$

Since $V_{us} = \lambda$, we can define a triangle with sides

$$1 \quad (50)$$

$$\left| \frac{V_{td}}{A\lambda^3} \right| = \frac{1}{\lambda} \sqrt{(\rho - 1)^2 + \eta^2} = \frac{1}{\lambda} \left| \frac{V_{td}}{V_{ts}} \right| \quad (51)$$

$$\left| \frac{V_{ub}}{A\lambda^3} \right| = \frac{1}{\lambda} \sqrt{\rho^2 + \eta^2} = \frac{1}{\lambda} \left| \frac{V_{ub}}{V_{cb}} \right|. \quad (52)$$

The CKM triangle is depicted in Fig. 36. We know two sides already: the base is

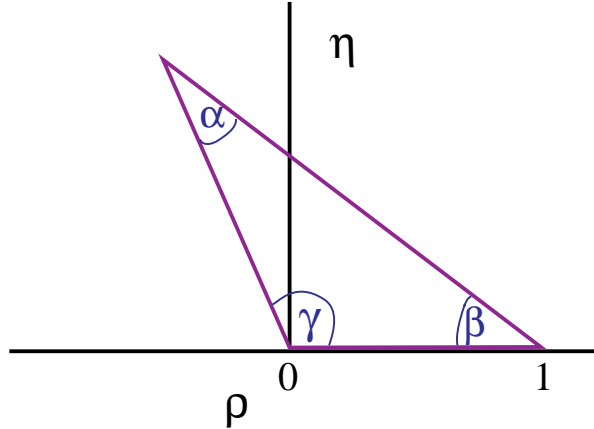


Fig. 36. The CKM triangle shown in the $\rho - \eta$ plane. The left side is determined by $|V_{ub}/V_{cb}|$ and the right side can be determined using mixing in the neutral B system. The angles can be found by making measurements of CP violation in B decays.

[†]Unitarity implies that any pair of rows or columns are orthogonal.

defined as unity and the left side is determined by the measurements of $|V_{ub}/V_{cb}|$. The right side can be determined using mixing measurements in the neutral B system. We will see, however, that there is a large error due to the uncertainty in f_B . Later we will discuss other measurements that can access this side. The figure also shows the angles as α , β , and γ . These angles can be determined by measuring CP violation in the B system. First we discuss CP violation in the K_L^0 system which also provides constraints on ρ and η .

To test the Standard Model we can measure all three sides and all three angles. If we see consistency between all of these measurements we have defined the parameters of the Standard Model. If we see inconsistency, the breakdown can point us beyond the Standard Model.

3.2. CP Violation

The fact that the CKM matrix is complex allows CP violation. This is not only true for three generations of quark doublets, but for any number greater than two. Now let us explain what we mean by CP violation. C is a quantum mechanical operator that changes particle to antiparticle, while P switches left to right, i.e. $x \rightarrow -x$. Thus under a P operation, $\vec{p} \rightarrow -\vec{p}$ since t is unaffected.

Examples of CP violation have been found in the K^0 system. Let us examine one such measurement. Consider the K^0 to be composed of long lived and short lived components having equal weight, so the wave function is

$$|K^0\rangle = \frac{1}{\sqrt{2}} (|K_S\rangle + |K_L\rangle) \quad . \quad (53)$$

In the case of neutral kaons there is a large difference in lifetimes between the short lived and long lived components. The lifetimes are 9×10^{-11} sec and 5×10^{-8} sec. Suppose we set up a detector far away from the K^0 production target. Then after the K_S decay away we have only a K_L beam. We find both

$$K_L \rightarrow e^+ \nu_e \pi^- \quad \text{and} \quad K_L \rightarrow e^- \bar{\nu}_e \pi^+ \quad (54)$$

are present. Now the initial state was a K^0 , which contains an \bar{s} quark and can only decay semileptonically into the $e^+ \nu_e \pi^-$ final state as shown in Fig. 37. Thus we have found evidence that both K^0 and \bar{K}^0 are present. This phenomenon, $K^0 \leftrightarrow \bar{K}^0$ is called mixing and can be depicted by the diagram shown in Fig. 38, much like the diagram for $B^0 \bar{B}^0$ mixing. However, here the c -quark loop has the largest amplitude, unlike the B case, where the t -quark is dominant. (This is because the CKM couplings are so much larger, i.e. V_{cs} and $V_{cd} \gg V_{ts}$ and V_{td} and this compensates for the decrease due to $(m_c/m_t)^2$.) There are also hadronic intermediate states which contribute to the real part of the mixing amplitude, such as $K^0 \rightarrow \pi\pi \rightarrow \bar{K}^0$.

An example of CP violation is the measured rate asymmetry in our K_L^0 detector⁵

$$\delta = 2Re(\epsilon) = \frac{\#(K_L \rightarrow e^+ \nu_e \pi^-) - \#(K_L \rightarrow e^- \bar{\nu}_e \pi^+)}{\#(K_L \rightarrow e^+ \nu_e \pi^-) + \#(K_L \rightarrow e^- \bar{\nu}_e \pi^+)} = 3.3 \times 10^{-3} \quad . \quad (55)$$

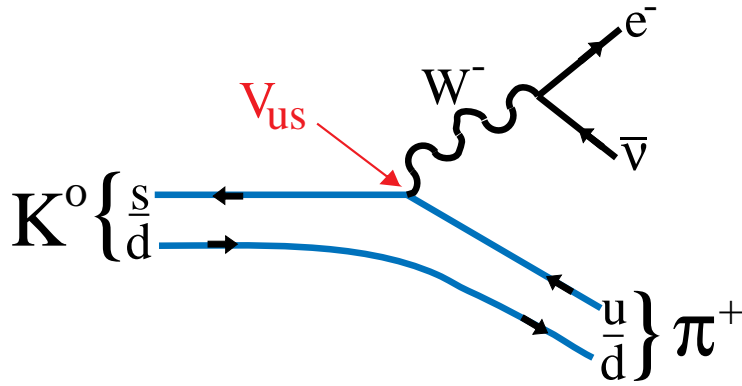


Fig. 37. Semileptonic decay of a s quark contained in a K^0 meson.

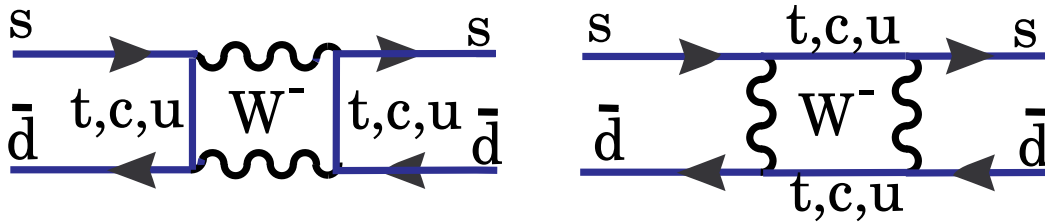


Fig. 38. $K^0 - \bar{K}^0$ mixing diagrams.

Let us look at why this violates CP. In Fig. 39 the momentum and spin vectors for the two final states are shown. The CP operation transforms the $e^+\nu_e\pi^-$ to the $e^-\bar{\nu}_e\pi^+$ final state and vice-versa. Thus CP invariance would imply equal rates for the two processes, contrary to what is observed.

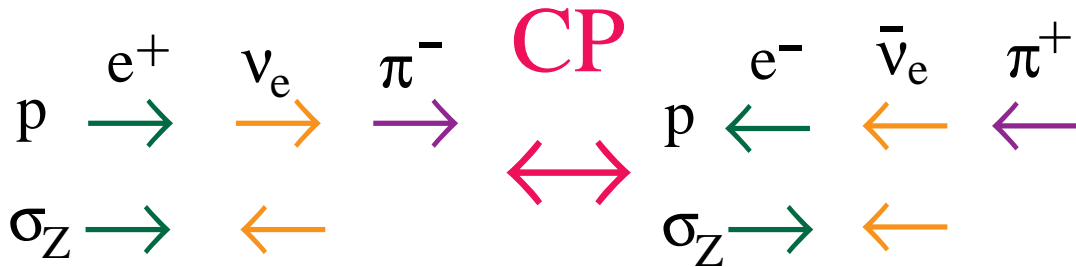


Fig. 39. The momentum and spin orientations of the two final states in semileptonic K_L^0 decay, showing that they are mapped into one another by a CP transformation.

CP violation thus far has only been seen in the neutral kaon system.[‡] If we can find CP violation in the B system we could see if the CKM model works or perhaps go beyond the model. Speculation has it that CP violation is responsible for the baryon-antibaryon asymmetry in our section of the Universe. If so, to understand the mechanism of CP violation is critical in our conjectures of why we exist.⁷¹

There is a constraint on ρ and η given by the K_L^0 CP violation measurement (ϵ), given by⁷²

$$\eta \left[(1 - \rho) A^2 (1.4 \pm 0.2) + 0.35 \right] A^2 \frac{B_K}{0.75} = (0.30 \pm 0.06), \quad (56)$$

where the errors arise from uncertainties on m_t and m_c . The constraints on ρ versus η from the V_{ub}/V_{cb} measurement, ϵ and B mixing are shown in Fig. 40. The width of the B mixing band is caused mainly by the uncertainty on f_B , taken here as $240 > f_B > 160$ MeV. The width of the ϵ band is caused by errors in A , m_t , m_c and B_K . The size of these error sources is shown in Fig. 41. The largest error still comes from the measurement of V_{cb} , with the theoretical estimate of B_K being a close second. The errors on m_t and m_c are less important.

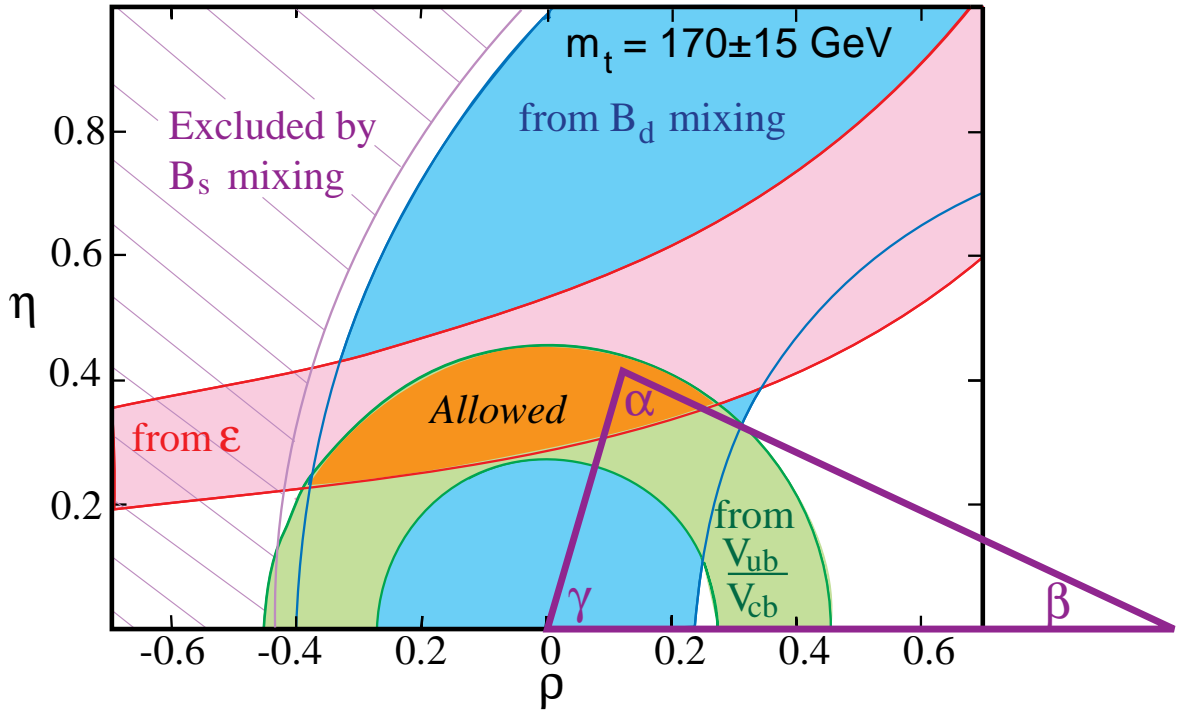


Fig. 40. The regions in $\rho - \eta$ space (shaded) consistent with measurements of CP violation in K_L^0 decay (ϵ), V_{ub}/V_{cb} in semileptonic B decay, B_d^0 mixing, and the excluded region from limits on B_s^0 mixing. The allowed region is defined by the overlap of the 3 permitted areas, and is where the apex of the CKM triangle sits.

[‡]The other observed example of CP violation is the decay $K_L^0 \rightarrow \pi\pi$.

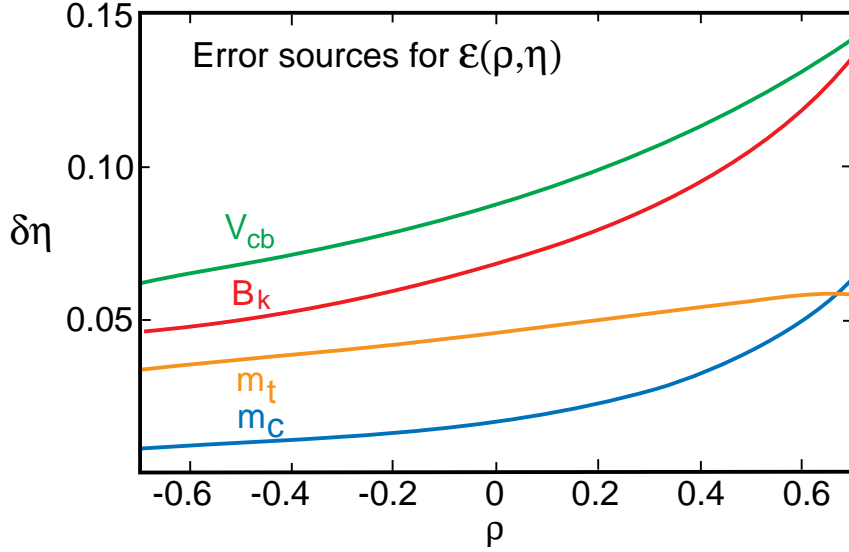


Fig. 41. Error sources in units of $\delta\eta$ on the value of η as a function of ρ provided by the CP violation constraint in K_L^0 decay.

3.3. Ways of Measuring CP violation in B Decays

3.3.1. CP Violation in Charged B Decays

The theoretical basis of the study of CP violation in B decays was given in series of papers by Carter and Sanda and Bigi and Sanda.⁷³ We start with charged B decays. Consider the final states f^\pm which can be reached by two distinct weak processes \mathcal{A} and \mathcal{B} . Then the strong (s) and weak (w) parts are

$$\mathcal{A} = a_s e^{i\theta_s} a_w e^{i\theta_w}, \quad \mathcal{B} = b_s e^{i\delta_s} b_w e^{i\delta_w} . \quad (57)$$

Under the CP operation the strong phases remain constant but the weak phases change sign, so

$$\overline{\mathcal{A}} = a_s e^{i\theta_s} a_w e^{-i\theta_w}, \quad \overline{\mathcal{B}} = b_s e^{i\delta_s} b_w e^{-i\delta_w} . \quad (58)$$

The rate difference is

$$\Gamma - \overline{\Gamma} = |\mathcal{A} + \mathcal{B}|^2 - |\overline{\mathcal{A}} + \overline{\mathcal{B}}|^2 \quad (59)$$

$$= 2a_s a_w b_s b_w \sin(\delta_s - \theta_s) \sin(\delta_w - \theta_w) . \quad (60)$$

A weak phase difference is guaranteed in the appropriate decay mode (different CKM phases), but the strong phase difference is not; it is very difficult to predict the magnitude of strong phase differences.

As an example consider the possibility of observing CP violation by measuring a rate difference between $B^- \rightarrow K^- \pi^0$ and $B^+ \rightarrow K^+ \pi^0$. The $K^- \pi^0$ final state can be

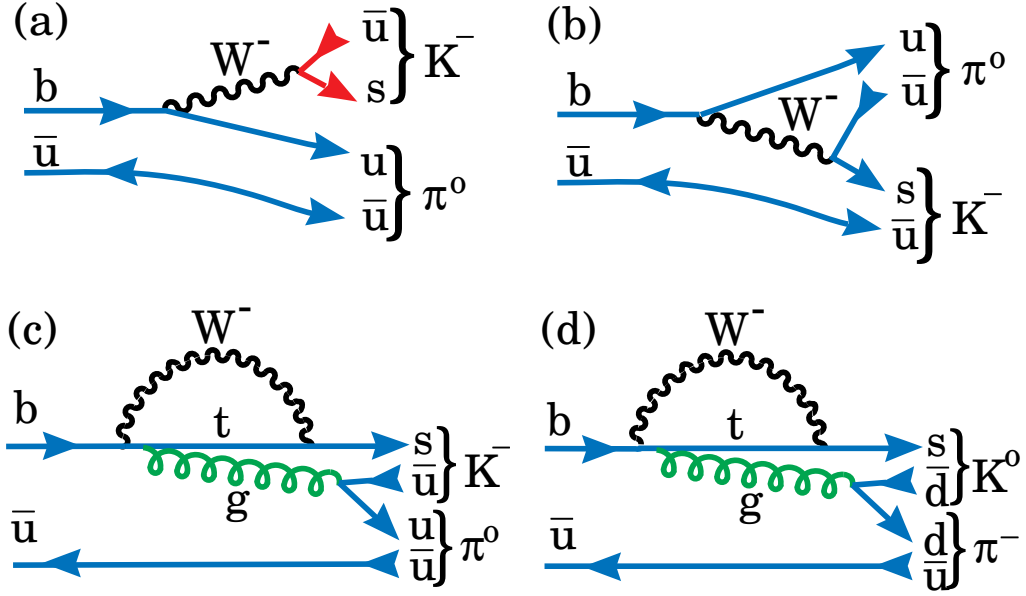


Fig. 42. Diagrams for $B^- \rightarrow K^- \pi^0$, (a) and (b) are tree level diagrams where (b) is color suppressed; (c) is a penguin diagram. (d) shows $B^- \rightarrow K^0 \pi^-$, which cannot be produced via a tree diagram.

reached either by tree or penguin diagrams as shown in Fig. 42. The tree diagram has an imaginary part coming from the V_{ub} coupling, while the penguin term does not, thus insuring a weak phase difference. This type of CP violation is called “direct.” Note also that the process $B^- \rightarrow K^0 \pi^-$ can only be produced by the penguin diagram in Fig. 42(d). Therefore, we do not expect a rate difference between $B^- \rightarrow K^0 \pi^-$ and $B^+ \rightarrow K^0 \pi^+$.

3.3.2. Formalism in neutral B decays

Consider the operations of C and P:

$$C|B(\vec{p})\rangle = |\bar{B}(\vec{p})\rangle, \quad C|\bar{B}(\vec{p})\rangle = |B(\vec{p})\rangle \quad (61)$$

$$P|B(\vec{p})\rangle = -|B(-\vec{p})\rangle, \quad P|\bar{B}(\vec{p})\rangle = -|\bar{B}(-\vec{p})\rangle \quad (62)$$

$$CP|B(\vec{p})\rangle = -|\bar{B}(-\vec{p})\rangle, \quad CP|\bar{B}(\vec{p})\rangle = -|B(-\vec{p})\rangle \quad (63)$$

For neutral mesons we can construct the CP eigenstates

$$|B_1^0\rangle = \frac{1}{\sqrt{2}} (|B^0\rangle - |\bar{B}^0\rangle) \quad , \quad (64)$$

$$|B_2^0\rangle = \frac{1}{\sqrt{2}} (|B^0\rangle + |\bar{B}^0\rangle) \quad , \quad (65)$$

where

$$CP|B_1^0\rangle = |B_1^0\rangle \quad , \quad (66)$$

$$CP|B_2^0\rangle = -|B_2^0\rangle. \quad (67)$$

Since B^o and \bar{B}^o can mix, the mass eigenstates are a superposition of $a|B^o\rangle + b|\bar{B}^o\rangle$ which obey the Schrodinger equation

$$i\frac{d}{dt}\begin{pmatrix} a \\ b \end{pmatrix} = H\begin{pmatrix} a \\ b \end{pmatrix} = \left(M - \frac{i}{2}\Gamma\right)\begin{pmatrix} a \\ b \end{pmatrix}. \quad (68)$$

If CP is not conserved then the eigenvectors, the mass eigenstates $|B_L\rangle$ and $|B_H\rangle$, are not the CP eigenstates but are

$$|B_L\rangle = p|B^o\rangle + q|\bar{B}^o\rangle, \quad |B_H\rangle = p|B^o\rangle - q|\bar{B}^o\rangle, \quad (69)$$

where

$$p = \frac{1}{\sqrt{2}}\frac{1 + \epsilon_B}{\sqrt{1 + |\epsilon_B|^2}}, \quad q = \frac{1}{\sqrt{2}}\frac{1 - \epsilon_B}{\sqrt{1 + |\epsilon_B|^2}}. \quad (70)$$

CP is violated if $\epsilon_B \neq 0$, which occurs if $|q/p| \neq 1$.

The time dependence of the mass eigenstates is

$$|B_L(t)\rangle = e^{-\Gamma_L t/2} e^{im_L t/2} |B_L(0)\rangle \quad (71)$$

$$|B_H(t)\rangle = e^{-\Gamma_H t/2} e^{im_H t/2} |B_H(0)\rangle, \quad (72)$$

leading to the time evolution of the flavor eigenstates as

$$|B^o(t)\rangle = e^{-(im + \frac{\Gamma}{2})t} \left(\cos \frac{\Delta m t}{2} |B^o(0)\rangle + i \frac{q}{p} \sin \frac{\Delta m t}{2} |\bar{B}^o(0)\rangle \right) \quad (73)$$

$$|\bar{B}^o(t)\rangle = e^{-(im + \frac{\Gamma}{2})t} \left(i \frac{p}{q} \sin \frac{\Delta m t}{2} |B^o(0)\rangle + \cos \frac{\Delta m t}{2} |\bar{B}^o(0)\rangle \right), \quad (74)$$

where $m = (m_L + m_H)/2$, $\Delta m = m_H - m_L$ and $\Gamma = \Gamma_L \approx \Gamma_H$. Note, that the probability of a B^o decay as a function of t is given by $\langle B^o(t)|B^o(t)\rangle^*$, and is a pure exponential, $e^{-\Gamma t/2}$, in the absence of CP violation.

3.3.3. Indirect CP violation in the neutral B system

As in the example described earlier for K_L decay, we can look for the rate asymmetry

$$a_{sl} = \frac{\Gamma(\bar{B}^o(t) \rightarrow X\ell^+\nu) - \Gamma(B^o(t) \rightarrow X\ell^-\bar{\nu})}{\Gamma(\bar{B}^o(t) \rightarrow X\ell^+\nu) + \Gamma(B^o(t) \rightarrow X\ell^-\bar{\nu})} \quad (75)$$

$$= \frac{1 - \left|\frac{q}{p}\right|^4}{1 + \left|\frac{q}{p}\right|^4} \approx O(10^{-2}). \quad (76)$$

These final states occur only through mixing as the direct decay occurs only as $B^o \rightarrow X\ell^+\nu$. To generate CP violation we need an interference between two diagrams. In this case the two diagrams are the mixing diagram with the t -quark and the mixing diagram with the c -quark. This is identical to what happens in the K_L^o case. This type of CP violation is called “indirect.” The small size of the expected asymmetry is caused by the off diagonal elements of the Γ matrix in equation (68) being very small compared to the off diagonal elements of the mass matrix, i.e. $|\Gamma_{12}/M_{12}| \ll 1$. This results from the nearly equal widths of the B_L^o and B_H^o .⁷⁴

3.3.4. CP violation for B via interference of mixing and decays

Here we choose a final state f which is accessible to both B^o and \bar{B}^o decays. The second amplitude necessary for interference is provided by mixing. Fig. 43 shows the decay into f either directly or indirectly via mixing. It is necessary only that f be

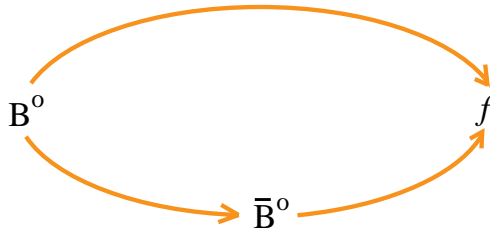


Fig. 43. Two interfering ways for a B^o to decay into a final state f .

accessible directly from either state, however if f is a CP eigenstate the situation is far simpler. For CP eigenstates

$$CP|f_{CP}\rangle = \pm|f_{CP}\rangle. \quad (77)$$

It is useful to define the amplitudes

$$A = \langle f_{CP}|\mathcal{H}|B^o\rangle, \quad \bar{A} = \langle f_{CP}|\mathcal{H}|\bar{B}^o\rangle. \quad (78)$$

If $|\frac{\bar{A}}{A}| \neq 1$, then we have “direct” CP violation in the decay amplitude, which we will discuss in detail later. Here CP can be violated by having

$$\lambda = \frac{q}{p} \cdot \frac{\bar{A}}{A} \neq 1, \quad (79)$$

which requires only that λ acquire a non-zero phase, i.e. $|\lambda|$ could be unity and CP violation can occur.

A comment on neutral B production at e^+e^- colliders is in order. At the $\Upsilon(4S)$ resonance there is coherent production of $B^o\bar{B}^o$ pairs. This puts the B 's in a $C = -1$ state. In hadron colliders, or at e^+e^- machines operating at the Z^o , the B 's are

produced incoherently. For the rest of this article I will assume incoherent production except where explicitly noted.

The asymmetry, in this case, is defined as

$$a_{f_{CP}} = \frac{\Gamma(B^o(t) \rightarrow f_{CP}) - \Gamma(\bar{B}^o(t) \rightarrow f_{CP})}{\Gamma(B^o(t) \rightarrow f_{CP}) + \Gamma(\bar{B}^o(t) \rightarrow f_{CP})}, \quad (80)$$

which for $|q/p| = 1$ gives

$$a_{f_{CP}} = \frac{(1 - |\lambda|^2) \cos(\Delta mt) - 2\text{Im}\lambda \sin(\Delta mt)}{1 + |\lambda|^2}. \quad (81)$$

For the cases where there is only one decay amplitude A , $|\lambda|$ equals 1, and we have

$$a_{f_{CP}} = -\text{Im}\lambda \sin(\Delta mt). \quad (82)$$

Only the amplitude, $-\text{Im}\lambda$ contains information about the level of CP violation, the sine term is determined only by B_d mixing. In fact, the time integrated asymmetry is given by

$$a_{f_{CP}} = -\frac{x}{1+x^2} \text{Im}\lambda = -0.48 \text{Im}\lambda. \quad (83)$$

This is quite lucky as the maximum size of the coefficient is -0.5 .

Let us now find out how $\text{Im}\lambda$ relates to the CKM parameters. Recall $\lambda = \frac{q}{p} \cdot \frac{\bar{A}}{A}$. The first term is the part that comes from mixing:

$$\frac{q}{p} = \frac{(V_{tb}^* V_{td})^2}{|V_{tb} V_{td}|^2} = \frac{(1 - \rho - i\eta)^2}{(1 - \rho + i\eta)(1 - \rho - i\eta)} = e^{-2i\beta} \quad \text{and} \quad (84)$$

$$\text{Im} \frac{q}{p} = -\frac{2(1 - \rho)\eta}{(1 - \rho)^2 + \eta^2} = \sin(2\beta). \quad (85)$$

To evaluate the decay part we need to consider specific final states. For example, consider $f \equiv \pi^+ \pi^-$. The simple spectator decay diagram is shown in Fig. 44. For the moment we will assume that this is the only diagram which contributes. Later I will show why this is not true. For this $b \rightarrow u\bar{u}d$ process we have

$$\frac{\bar{A}}{A} = \frac{(V_{ud}^* V_{ub})^2}{|V_{ud} V_{ub}|^2} = \frac{(\rho - i\eta)^2}{(\rho - i\eta)(\rho + i\eta)} = e^{-2i\gamma}, \quad (86)$$

and

$$\text{Im}(\lambda) = \text{Im}(e^{-2i\beta} e^{-2i\gamma}) = \text{Im}(e^{2i\alpha}) = \sin(2\alpha). \quad (87)$$

For our next example let's consider the final state ψK_S . The decay diagram is shown in Fig. 45. In this case we do not get a phase from the decay part because

$$\frac{\bar{A}}{A} = \frac{(V_{cb} V_{cs}^*)^2}{|V_{cb} V_{cs}|^2} \quad (88)$$

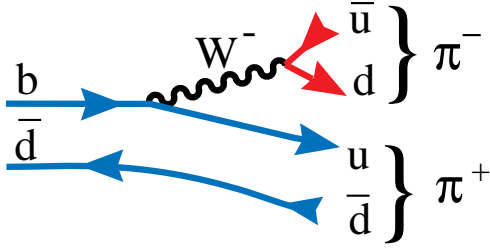


Fig. 44. Decay diagram at the tree level for $B^0 \rightarrow \pi^+\pi^-$.

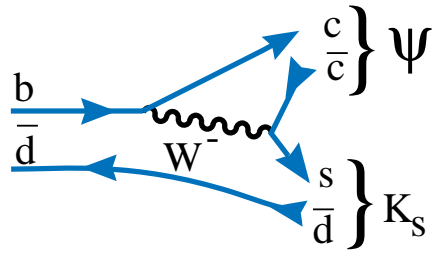


Fig. 45. Decay diagram at the tree level for $B^0 \rightarrow \psi K_S$.

is real. In this case the final state is a state of negative CP , i.e. $CP|\psi K_S\rangle = -|\psi K_S\rangle$. This introduces an additional minus sign in the result for $\text{Im}\lambda$. Before finishing discussion of this final state we need to consider in more detail the presence of the K_S in the final state. Since neutral kaons can mix, we pick up another mixing phase (see Fig. 38). This term creates a phase given by

$$\left(\frac{q}{p}\right)_K = \frac{(V_{cd}^* V_{cs})^2}{|V_{cd} V_{cs}|^2}, \quad (89)$$

which is real. It necessary to include this term, however, since there are other formulations of the CKM matrix than Wolfenstein, which have the phase in a different location. It is important that the physics predictions not depend on the CKM convention.[§]

In summary, for the case of $f = \psi K_S$, $\text{Im}\lambda = -\sin(2\beta)$.

3.3.5. Comment on Penguin Amplitude

In principle all processes can have penguin components. One such diagram is shown in Fig. 46. The $\pi^+\pi^-$ final state is expected to have a rather large penguin

[§]Here we don't include CP violation in the neutral kaon since it is much smaller than what is expected in the B decay.

amplitude $\sim 10\%$ of the tree amplitude. Then $|\lambda| \neq 1$ and $a_{\pi\pi}(t)$ develops a $\cos(\Delta mt)$ term. It turns out (see Gronau⁷⁵), that $\sin(2\alpha)$ can be extracted using isospin considerations and measurements of the branching ratios for $B^+ \rightarrow \pi^+\pi^0$ and $B^0 \rightarrow \pi^0\pi^0$.

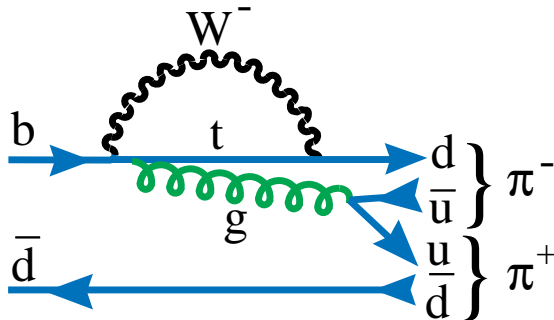


Fig. 46. Penguin diagram for $B^0 \rightarrow \pi^+\pi^-$.

In the ψK_S case, the penguin amplitude is expected to be small since a $c\bar{c}$ pair must be “popped” from the vacuum. Even if the penguin decay amplitude were of significant size, the decay phase is the same as the tree level process, namely zero.

3.3.6. What actually has to be measured?

In charged B decays we only have to measure a branching ratio difference between B^+ and B^- to see CP violation. For neutral B decays we must find the flavor of the other b -quark produced in the event (this is called tagging), since we do not have any B^0 beams. We then measure a rate asymmetry

$$a_{asy} = \frac{\#(f, \ell^+) - \#(f, \ell^-)}{\#(f, \ell^+) + \#(f, \ell^-)}, \quad (90)$$

where ℓ^\pm indicates the charge of the lepton from the “other” b and thus provides a flavor tag. In Fig. 47(a) the time dependence for the B^0 and \bar{B}^0 are shown as a function of t in the B rest frame for 500 experiments of an average of 2000 events each with an input asymmetry of 0.3. In Fig. 47(b) the fitted asymmetry is shown for 500 different “experiments.”

3.4. Better Measurements of the sides of the CKM triangle

One side of the triangle is determined by $|V_{ub}/V_{cb}|$. It appears that the best way to improve the values now is to measure the form-factors in the reactions $B \rightarrow \pi\ell\nu$ and $B \rightarrow \rho\ell\nu$. This will decrease the model dependence error, still the dominant errors, in the V_{ub} determination. Lattice gauge model calculations are appearing and should be quite useful.

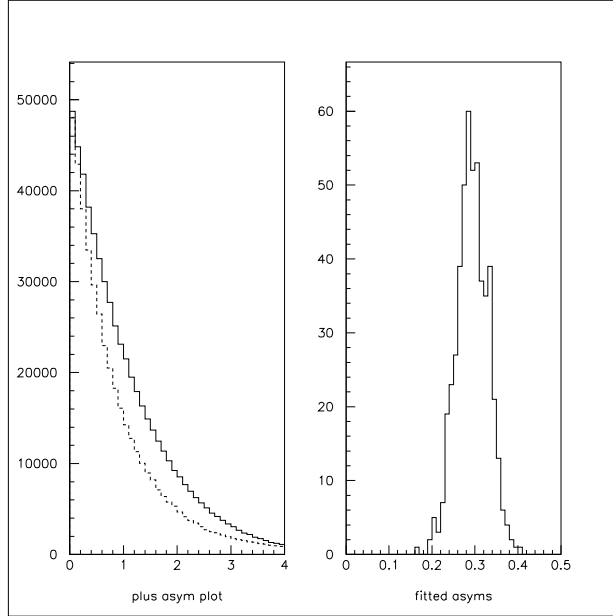


Fig. 47. (a) Time dependence of B^0 and \overline{B}^0 decaying into a CP eigenstate, for an asymmetry of 0.3 for a total of 1 million events. The x-axis is proper time. In (b) the fitted asymmetry results are shown for 500 “experiments” of average of 2000 events each.

The other side of the triangle can be determined by measuring B_s mixing, using the ratio

$$\frac{x_s}{x_d} = \left(\frac{B_s}{B}\right) \left(\frac{f_{B_s}}{f_B}\right)^2 \left(\frac{\tau_{B_s}}{\tau_B}\right) \left|\frac{V_{td}}{V_{ts}}\right|^2, \quad (91)$$

where

$$\left|\frac{V_{td}}{V_{ts}}\right|^2 = \lambda^2 [(\rho - 1)^2 + \eta^2]. \quad (92)$$

The large uncertainty in using the B_d mixing measurement to constrain ρ and η is largely removed as the ratio of the first three factors in equation (91) is already known to 10%.

As an alternative to measuring x_s , we can measure the ratio of the penguin decay rates

$$\frac{\mathcal{B}(B \rightarrow \rho\gamma)}{\mathcal{B}(B \rightarrow K^*\gamma)} = \xi \left|\frac{V_{td}}{V_{ts}}\right|^2, \quad (93)$$

where ξ is a model dependent correction due to different form-factors. Soni⁷⁶ has claimed that “long distance” effects, basically other diagrams spoil this simple relationship. This is unlikely for $\rho^0\gamma$ but possible for $\rho^+\gamma$.[¶]If this occurs, however, then

[¶]One example is the B^- decay which proceeds via $b \rightarrow uW^-$, where the $W^- \rightarrow \bar{u}d \rightarrow \rho^-$ and the u combines with the spectator \bar{u} to form a photon.

it is possible to find CP violation by looking for a difference in rate between $\rho^+\gamma$ and $\rho^-\gamma$.

The CLEO II data are already background limited. The limit quoted is⁶⁰

$$\frac{\mathcal{B}(B \rightarrow \rho\gamma)}{\mathcal{B}(B \rightarrow K^*\gamma)} < 0.19 \quad (94)$$

at 90% confidence level.

3.5. Rare decays as Probes beyond the Standard Model

Rare decays have loops in the decay diagrams so they are sensitive to high mass gauge bosons and fermions. However, it must be kept in mind that any new effect must be consistent with already measured phenomena such as B_d^0 mixing and $b \rightarrow s\gamma$.

Let us now consider searches for other rare b decay processes. The process $b \rightarrow s\ell^+\ell^-$ can result from the diagrams in Fig. 26(e or f). When searching for such decays, care must be taken to eliminate the mass region in the vicinity of the ψ or ψ' resonances, lest these more prolific processes, which are not rare decays, contaminate the sample. The result of searches are shown in Table 10.

Table 10. Searches for $b \rightarrow s\ell^+\ell^-$ decays

b decay mode	90% c.l. upper limit	Group	Ali et al. Prediction ⁷⁷
$s\mu^+\mu^-$	50×10^{-6}	UA1 ⁷⁸	
$K^{*0}\mu^+\mu^-$	25×10^{-6}	CDF ⁸⁰	2.9×10^{-6}
	23×10^{-6}	UA1 ⁷⁸	
	31×10^{-6}	CLEO ⁷⁹	
$K^{*0}e^+e^-$	16×10^{-6}	CLEO ⁷⁹	5.6×10^{-6}
$K^-\mu^+\mu^-$	9×10^{-6}	CLEO ⁷⁹	0.6×10^{-6}
	10×10^{-6}	CDF ⁸⁰	
$K^-e^+e^-$	12×10^{-6}	CLEO ⁷⁹	0.6×10^{-6}

B 's can also decay into dilepton final states. The Standard Model diagrams are shown in Fig. 48. In (a) the decay rate is proportional to $|V_{ub}f_B|^2$. The diagram in (b) is much larger for B_s than B_d , again the factor of $|V_{ts}/V_{td}|^2$. Results of searches are given in Table 11.

4. Future Experiments

4.1. e^+e^- machines operating at the $\Upsilon(4S)$

Recall that only B meson pairs are produced at the $\Upsilon(4S)$ as shown in Fig. 6. Since each B has about 30 MeV of kinetic energy, it moves on the average only 30

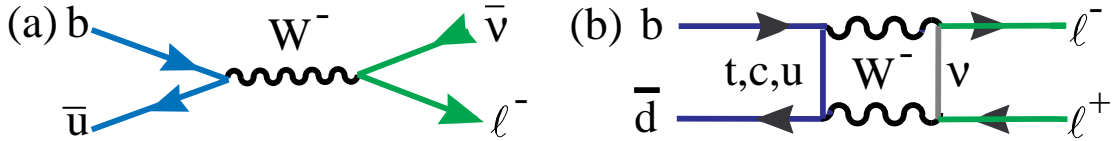


Fig. 48. Decay diagrams resulting in dilepton final states. (a) is an annihilation diagram, and (b) is a box diagram.

Table 11. Upper limits on $b \rightarrow$ dilepton decays (@90% c.l.)

	$\mathcal{B}(B^0 \rightarrow \ell^+ \ell^-)$		$\mathcal{B}(B_s \rightarrow \ell^+ \ell^-)$	$\mathcal{B}(B^- \rightarrow \ell^- \bar{\nu})$		
	$e^+ e^-$	$\mu^+ \mu^-$	$\mu^+ \mu^-$	$e^- \bar{\nu}$	$\mu^- \bar{\nu}$	$\tau^- \bar{\nu}$
SM [†]	2×10^{-15}	8×10^{-11}	2×10^{-9}	10^{-15}	10^{-8}	10^{-5}
UA1 ⁷⁸		8.3×10^{-6}				
CLEO ⁸¹	5.9×10^{-6}	5.9×10^{-6}		1.5×10^{-5}	2.1×10^{-5}	2.2×10^{-3}
CDF ⁸⁰		1.6×10^{-6}	8.4×10^{-6}			
ALEPH ⁸²						1.8×10^{-3}

[†]SM is the Standard Model prediction.⁸³

μm before it decays. Another important consequence is that the decay products mix together and do not appear in distinct jets. To measure the important time difference required in CP violation experiments via mixing, it is necessary to give the B 's a Lorentz boost which can be accomplished by using asymmetric beam energies.⁸⁴

Let me amplify on this last statement. The asymmetry I presented

$$a_{f_{CP}} = -\text{Im}\lambda \sin(\Delta mt), \quad (95)$$

is calculated for incoherent production of the B^0 and another b quark (t is the time from production of the B^0 until it decays). In e^+e^- production the B 's can be produced in a coherent state. At the $\Upsilon(4S)$ $C = -1$, while at higher energies, where $B^* \bar{B}$ ($B^* \rightarrow B\gamma$) is produced, $C = +1$. For coherent production equation (95) gets modified to

$$a_{f_{CP} \ C=\pm} = -\text{Im}\lambda \sin(\Delta m(t \pm t')), \quad (96)$$

where t refers to the decay time of f_{CP} and t' the decay time of the tagging B . In principle, $a_{f_{CP}}$ can be measured by taking a time integral. For incoherent production this works fine (see equation (83)). Here, however, the integral over the $C = -1$ case gives exactly zero, necessitating the time dependent measurement. The integral over the $C = +1$ case, does not give zero, but the measured cross-section for $B^* \bar{B}$ is about 1/7 that of the $\Upsilon(4S)$.^{85,86}

The one serious disadvantage of the $\Upsilon(4S)$ machines is that the cross-section is only 1 nb, so at a peak luminosity of 3×10^{33} , we expect only 60 million B 's/year. For example, for a rare process with a branching ratio of 5×10^{-6} and a "typical" efficiency of 20%, we get only 60 events/year.

It is also important to note that there will not be much more B physics from LEP. The data sample has been collected and there are no current plans to get another large sample of Z^0 decays to add to the brilliant b physics already done.

The CESR machine will be upgraded to produce a luminosity in excess of $2 \times 10^{33} \text{cm}^{-2} \text{s}^{-1}$, albeit with symmetric energy beams. Both the KEK laboratory in Japan and SLAC in Stanford, Cal. will construct asymmetric energy machines with planned luminosities in excess of $3 \times 10^{33} \text{cm}^{-2} \text{s}^{-1}$.

The advantages of such machines are that the b cross-section is 1/4 of the total, and the relatively clean environment and low interaction rates allow for superb photon detection using CsI crystal calorimeters⁸⁷ and for planned particle identification systems which should provide excellent π/K separation.⁸⁸

4.2. Hadron machines

Let us first discuss the characteristics of hadronic b production. Hadronic b production mechanisms are shown in Fig. 49.⁸⁹ The relative contribution of the terms

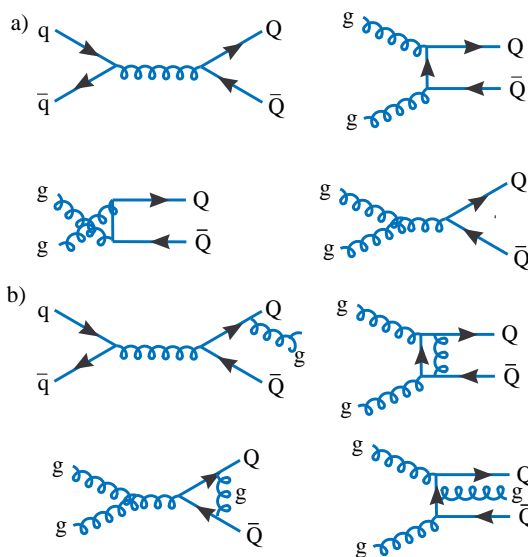


Fig. 49. Feynman diagrams for heavy quark production in hadronic collisions (a) of order α_s^2 , and (b) some diagrams of order α_s^3 .

proportional to α_s^2 and those proportional to α_s^3 is not well known. This is an important issue since the correlations in rapidity, η and in azimuthal angle between the b -quark and the \bar{b} -quark depends on the production mechanism. It is generally thought that $|\eta_b - \eta_{\bar{b}}| < 2$. In Fig. 50 I show the azimuthal opening angle distribution between a muon from a b quark decay and the \bar{b} jet as measured by CDF⁹⁰ and compare with the MNR predictions.⁹¹ The model does a good job in representing the shape which shows a strong back-to-back correlation. The normalization is about a factor of two higher in the data than the theory, which is generally true of CDF b

cross-section measurements.⁹² In hadron colliders all B species are produced at the same time.

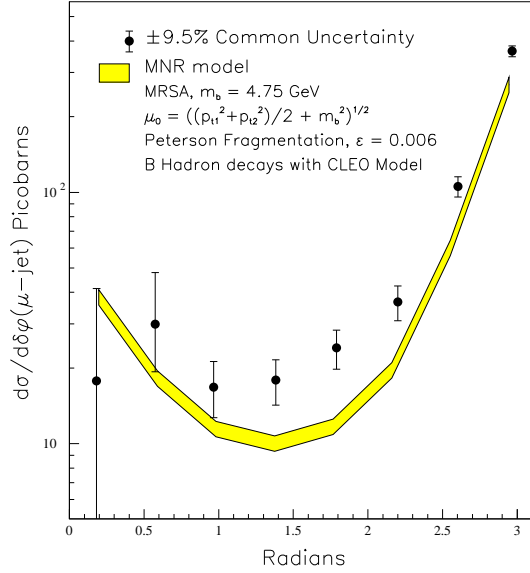


Fig. 50. The differential $\delta\phi$ cross-sections for $p_T^\mu > 9 \text{ GeV}/c$, $|\eta^\mu| < 0.6$, $E_T^{\bar{b}} > 10 \text{ GeV}$, $|\eta^{\bar{b}}| < 1.5$ compared with theoretical predictions. The data points have a common systematic uncertainty of $\pm 9.5\%$. The uncertainty in the theory curve arises from the error on the muonic branching ratio and the uncertainty in the fragmentation model.

The B meson transverse momentum distribution is severely limited and peaks near the B meson mass. The distribution in η , however is spread widely. In Fig. 51 I show the predicted (Pythia) distribution at the Tevatron collider. It should be realized

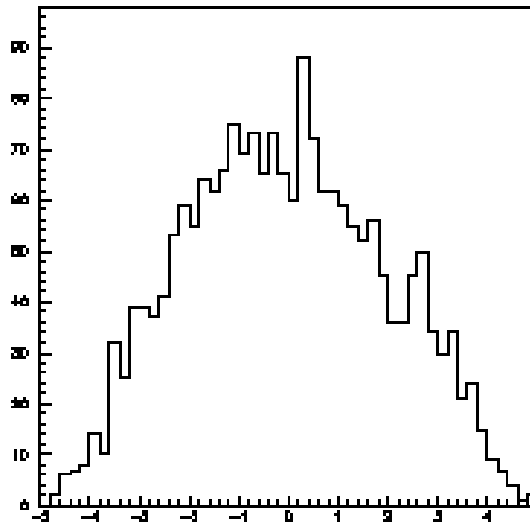


Fig. 51. The predicted distribution of B 's versus η for 1.8 TeV $p\bar{p}$ collisions.

that this distribution in η reflects into a sharply peaked distribution in spatial angle ($\cos(\theta)$). The laboratory angular distributions of the B and \bar{B} mesons expected at the LHC are shown in Fig. 52. Most of the events are far forward with the B and \bar{B} being strongly correlated.⁹³

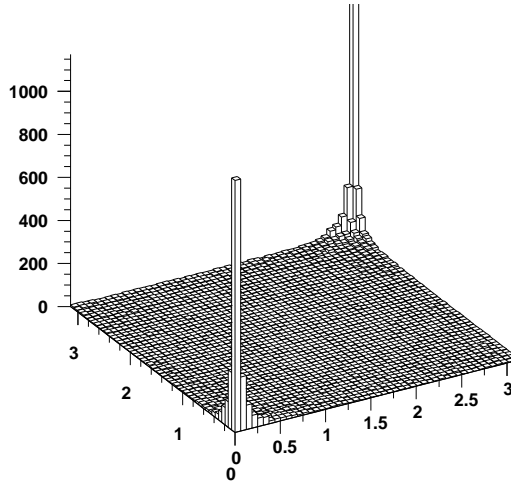


Fig. 52. Production angles of B versus production angle of the \bar{B} in the laboratory (in radians) for the LHC collider calculated using PYTHIA.

Let us review some properties of current and proposed hadron b collider experiments.⁹⁴

- The CDF and D0 detectors already exist at the Fermilab collider. The b cross-section is $\sim 50 \mu\text{b}$, with the ratio $\sigma(b)/\sigma(\text{total}) = 10^{-3}$. The luminosity is now close to 10^{31} and will increase with the advent of the main injector to 10^{32} . However, the restrictive trigger limits the b sample.
- The HERA- b experiment at DESY collides the HERA proton beam with fixed wire targets. The b cross-section is only $\sim 6 \text{ nb}$ with $\sigma(b)/\sigma(\text{total}) = 10^{-6}$. In order to produce enough b 's they plan on four interactions per crossing. The goal is to measure CP violation in the ψK_S decay mode and possibly investigate other modes that are accessible by triggering on dileptons. The experiment is now under construction.
- The LHC-B experiment is being planned. At the LHC the b cross-section is $\sim 300 \mu\text{b}$, with the ratio $\sigma(b)/\sigma(\text{total}) = 3 \times 10^{-3}$. The experiment can run at a luminosity of 10^{32} , ≈ 240 Billion B^0 /year are produced.
- Also at the LHC, the Atlas and CMS experiments will have some B capabilities.
- There is now a proposal for a dedicated B collider experiment at Fermilab called BTeV. Here ≈ 60 Billion B^0 /year are produced.

4.3. Detector Considerations

For an experiment to do frontier B physics the following components appear to be necessary:

- Silicon vertex detector
- Charged particle tracking with magnetic analysis
- Cherenkov identification of charged hadrons
- Electromagnetic shower detection
- Muon detection with iron

A precision vertex detector is necessary to use the long B lifetime to reject background. Silicon is the current technology of choice; it can be realized as strips or as pixels. Charged particle tracking with magnetic analysis is important for momentum measurement as it is in most experiments. In order to pick out specific B decay modes, such as $K^+\pi^-$ from $\pi^+\pi^-$ or $\rho\gamma$ from $K^*\gamma$, it is crucial to have kaon and pion identification. Currently this is best provided using Cherenkov radiation.⁸⁸ Electromagnetic shower detection and muon identification are required to study semileptonic decays and provide flavor tags. The BELLE experiment, shown in Fig. 53 is an example of a detector that has all of these elements.

There are important constraints on all of these detection elements. Radiation damage implies various limits and certain technologies. The number of interactions per second implies a rate limit on detector elements. It appears that the maximum rate on any detector element is about 10^7 /sec. The total detector readout rate is limited to about 10-100 MB/sec. (The smaller number is given by current technology and the larger number is based on expected improvement.) For an event size of 100 KB, this gives a maximum readout rate of 1000 events/sec.

Next, I will discuss the trigger. e^+e^- experiments have a distinct advantage here, since they merely trigger on everything. Experiments at hadron collider must trigger very selectively, or the data transmission rate will be swamped by background. There are several trigger strategies which have been developed. The one with the highest background rejection is $B \rightarrow \psi X$, $\psi \rightarrow \ell^+\ell^-$. Unfortunately the branching ratio for the former is only 1.1% and the latter 12%, giving a maximum triggerable B event rate of only 2.6×10^{-3} . This must be reduced by efficiency of the apparatus and kinematic cuts.

Another strategy is to trigger on semileptonic decays, where the 10% branching ratio to both muons or electrons is attractive. Furthermore, for CP violation measurements through mixing, this trigger also provides a tag. It has been traditionally easier to trigger on muons because electrons can easily be faked by photon conversions near the vertex or Dalitz decays of the π^0 .

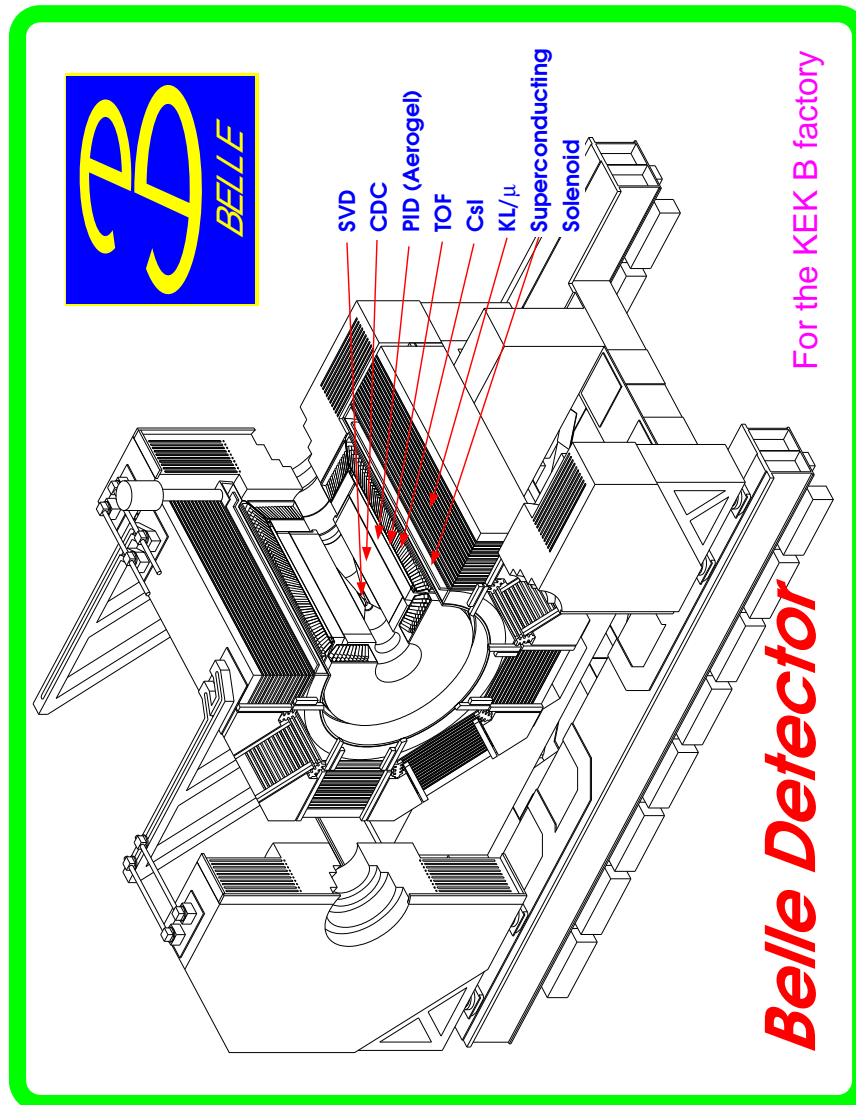


Fig. 53. Diagram of the Belle detector.

The most progressive strategy is to trigger on detached vertices. Recent simulations for BTeV have shown that it is possible to achieve a good efficiency $> 70\%$ on B decay events with a rejection on light quark background in excess of 100:1. To achieve this it is necessary to use a forward geometry with the silicon vertex detector inside the beam pipe.⁹⁵ A test of this concept was done at CERN by experiment P238.⁹⁶ A sketch of the silicon detector arrangement is shown in Fig. 54.

It is also possible to consider triggering on specific low multiplicity final states such as $B^0 \rightarrow \pi^+\pi^-$ by using hadrons with $p_t > 1 \text{ GeV}/c$.

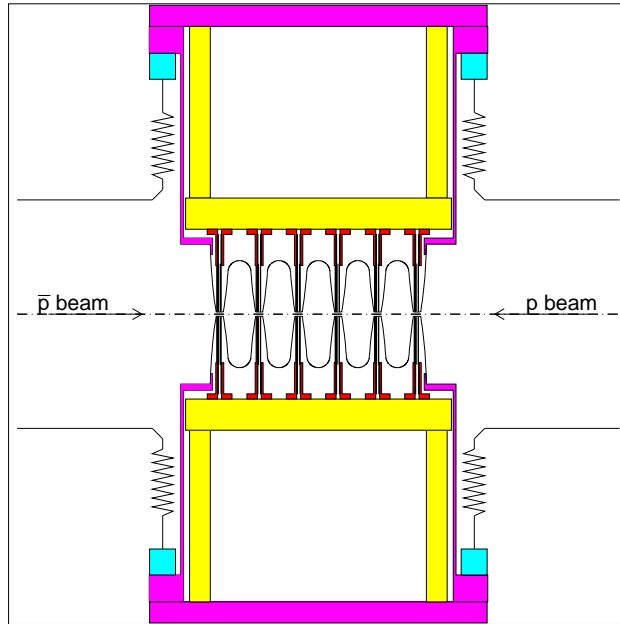


Fig. 54. Side view of the P238 silicon detector assembly and Roman pots. The 6 silicon planes are the vertical lines just above and below the beam line. The bellows (zig-zag lines) allow movements in the vertical direction of the pots, which are the thin vertical lines close to the bellows (they have 2 mm wall thickness). The edges of the 200 μm -thick aluminum RF shields closest to the beam (shown as the thin curved lines near the silicon detectors) normally ran at a distance of 1.5 mm from the circulating beams. The black horizontal pieces at top and bottom are the vacuum bulkheads bolted to the Roman pots.

The crucial issue in all of the trigger strategies is what the background rates are for a high signal efficiency. Does this give enough signal events with simultaneously rejecting background at the 100:1 level?

4.4. Hadron Geometries

There is a choice between two basic geometrical configurations that can be used for collider hadron B experiments. One is a central detector. An example is given by the planned upgraded CDF detector, shown in Fig. 55. Here the detector elements are arranged in an almost cylindrical manner about the beam pipe, so that the detector is very good near η equals zero. Notice that there are no detector elements for particle identification, though some information may be available from dE/dx measurements in the tracking chamber. An example of a forward detector is the proposed LHC-B experiment shown in Fig. 56. Here the vertex detector is inside a flared beam pipe. There are three different radiators for the RICH detectors.

In hadron colliders the most important rejection of non- B background is accomplished by seeing a detached decay vertex. In Fig. 57 I show the normalized decay length expressed in terms of L/σ where L is the decay length and σ is the error on L for the $B^0 \rightarrow \pi^+\pi^-$ decay.⁹⁷ This study was done for the Fermilab Tevatron.

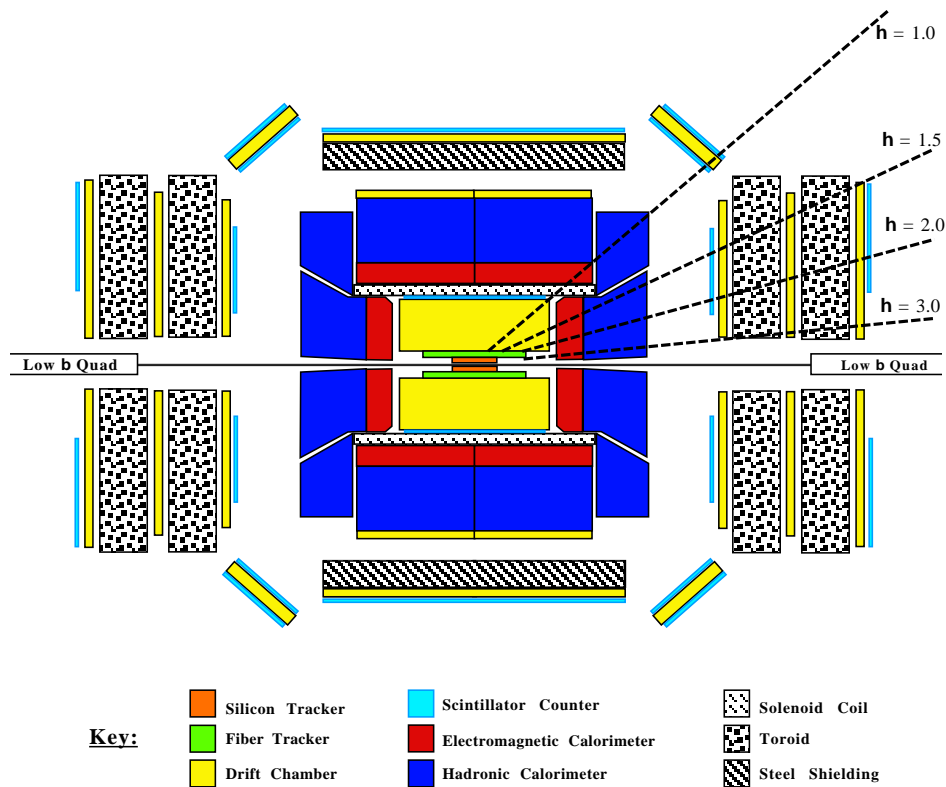


Fig. 55. A schematic diagram of the CDF upgrade. The symbol ‘h’ refers to rapidity. Note that the fiber tracker may change to a different technology.

The forward detector clearly has a much more favorable L/σ distribution. In Fig. 58 we show the time resolution in picoseconds for the forward and central detectors for the reaction $B_s \rightarrow \psi K_s$, which has been suggested as a possible way to measure B_s mixing.⁹⁸ Remarkably the time resolution is a factor of 10 smaller for the forward detector.

A comparison of different B experiments is shown in Table 12.

5. Conclusions

B decay physics started in the 1980’s and the first generation of experiments at CESR, DORIS, PEP, PETRA, LEP and CDF have made great contributions including the first fully reconstructed B ’s and precise measurement of the B meson masses, measurement of the B lifetimes, discovery of $B^0 - \bar{B}^0$ mixing, the measurement of the CKM parameters V_{cb} and V_{ub} and the sighting of the first rare decays.

Many mysteries, however, remain to be untangled. Measuring independently all sides and angles of the CKM triangle may point us beyond the Standard Model if the data are inconsistent. This will require measuring all three CP violating angles,

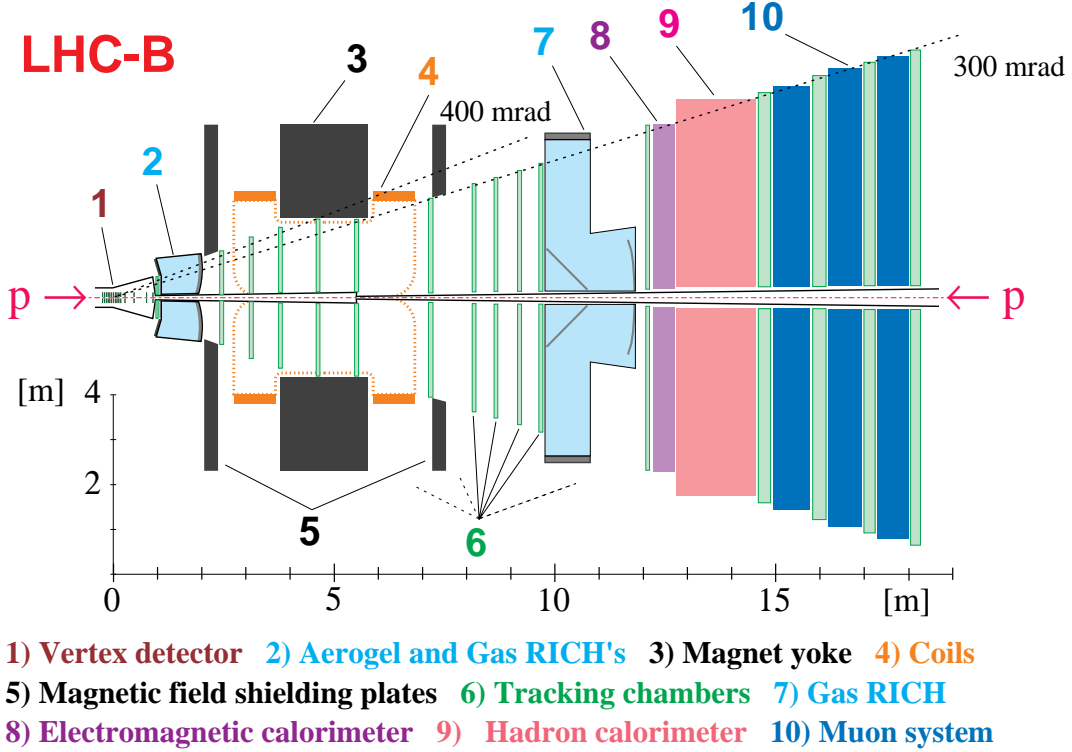


Fig. 56. A schematic diagram of the proposed LHC-B detector.

Table 12. Comparison of B decay detectors

Experiment	Particle I. D.	Vertex detection	Photon detection	$\sigma(b)$	$\frac{\sigma(b)}{\sigma(T)}$
Babar	Excellent	Good	Excellent	1 nb	0.25
Belle	Good	Good	Excellent	1 nb	0.25
CLEO	Excellent	Mediocre [†]	Excellent	1 nb	0.25
CDF	Poor	Good	Poor	50 μb	10^{-3}
D0	Poor	Good	Poor	50 μb	10^{-3}
HERA-B	Excellent	Excellent	Poor	6 nb	10^{-6}
LHC-B	Excellent	Excellent	Poor	300 μb	3×10^{-3}

[†] detector is excellent but low B velocity compromises vertex detection

measuring B_s mixing and precisely determining V_{ub}/V_{cb} . Furthermore, observation of rare B decays may also point us beyond the Standard Model.⁹⁹

e^+e^- threshold machines are great for future B physics. They will surely produce precision measurements of V_{ub} and V_{cb} and the important measurement of $\sin(2\beta)$ using the ψK_S decay mode. Possibly $\sin(\gamma)$ can be measured using charged B decays and there are some who think these machines can measure $\sin(2\alpha)$, but I find that unlikely. However, these experiments are limited by the total number of B mesons.

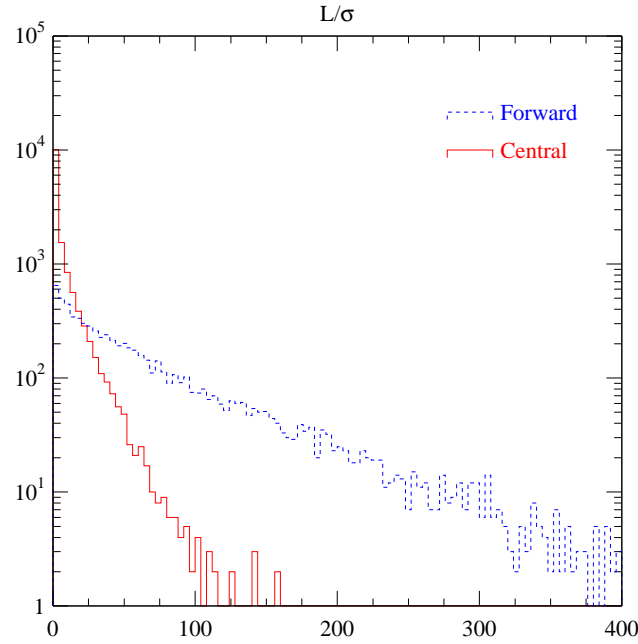


Fig. 57. Comparison of the L/σ distributions for the decay $B^0 \rightarrow \pi^+\pi^-$ in central and forward detectors produced at a hadron collider with a center of mass energy of 1.8 TeV.

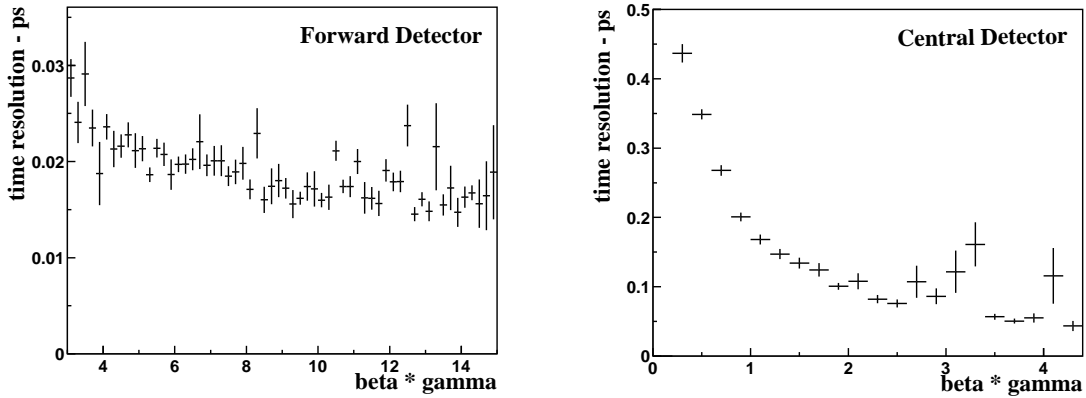


Fig. 58. The time resolution plotted as a function of $\beta\gamma$ for a forward detector ($2.0 < \eta < 4.5$) and a central detector ($|\eta| < 1.5$) for the decay $B_s \rightarrow \psi\bar{K}^*$ produced at a hadron collider with a center of mass energy of 1.8 TeV.

Even if these machines reach luminosities of $10^{34}\text{cm}^{-2}\text{s}^{-1}$, there are not enough B 's to probe most rare phenomena. The prospects for B_s mixing, Λ_b and B_c studies are dim.

There is a fantastic potential for studying CP violation phenomena and rare B studies in hadronic machines but it's not easy. Let us consider the calculation of the error on an asymmetry measurement:

$$\sigma(a_{asy}) = \frac{1}{D\sqrt{N_{eff} \cdot \epsilon \cdot B}}, \quad (97)$$

where

$$N_{eff} = N \frac{Signal}{Signal + Background}, \quad (98)$$

B is the branching ratio of the final state of interest, ϵ is the overall efficiency including the tagging efficiency. D is the dilution factor caused by anything which causes a wrong-sign tag to be found, such as away side mixing, lepton misidentification etc.. A sample calculation is shown in Table 13.

Table 13. Sensitivity Calculation for Observing a CP asymmetry in ψK_S

CM energy	2 TeV
Cross-section	50 μb
Luminosity	$10^{32} \text{cm}^{-2} \text{s}^{-1}$
N_{B^0} /'Snowmass' year	3.75×10^{10}
$\mathcal{B}(B^0 \rightarrow \psi K_S)$	5.5×10^{-4}
$\mathcal{B}(B^0 \rightarrow \psi(\mu^+\mu^-)K_S(\pi^+\pi^-))$	2.2×10^{-5}
$N(B^0 \rightarrow \mu^+\mu^-\pi^+\pi^-)/\text{year}$	8.2×10^5
Semi-leptonic decay of away side tag	0.10
Tagged $N(B^0 \rightarrow \mu^+\mu^-\pi^+\pi^-)/\text{year}$	8.2×10^4
Triggering efficiency	0.8
Reconstruction efficiency of $\mu\mu\pi\pi$	0.25
Reconstruction efficiency μ tag	0.25
Vertex finding efficiency	0.9
Cleanup & analysis cuts	0.7
Dilution factors:	
Shape dependence D_{t-int}	0.47
mixing of muon tag	0.75
muon tag misidentification	0.9
Time resolution and cuts	0.95
Background	0.95
Total sensitivity	0.07

This calculation shows an error in the asymmetry of 7%. To see if that is in the range of interest, I show in Fig. 59 the expectations for the three CP violating angles and x_s . These plots merely reflect the ‘‘allowed’’ region shown in Fig. 40. It should

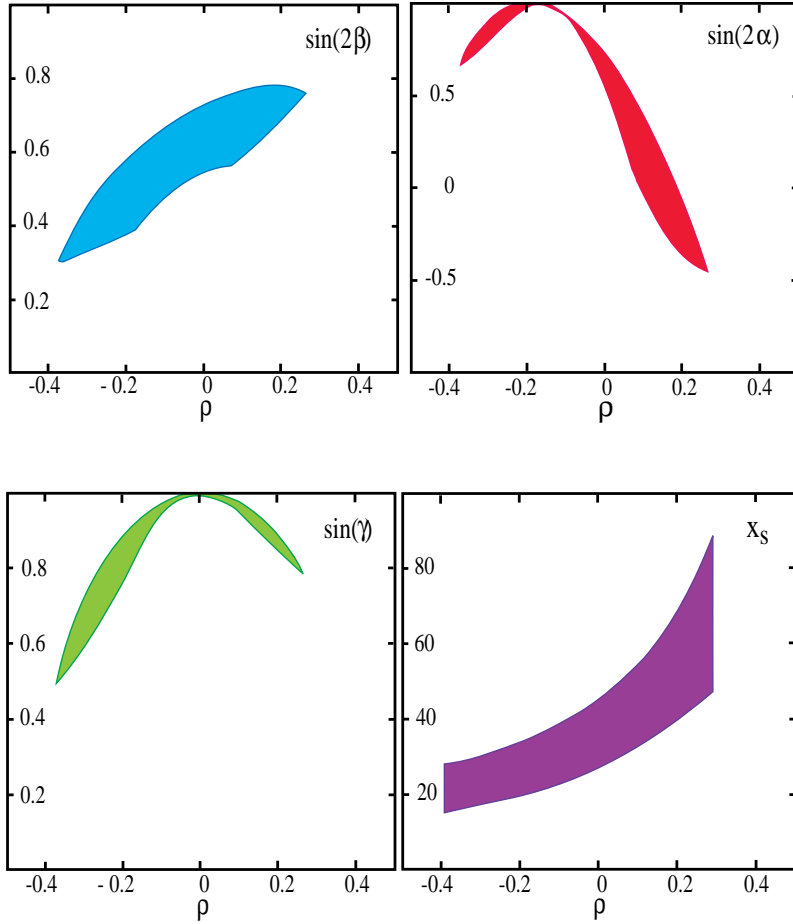


Fig. 59. The allowed values of three CP violating angles and the B_s mixing parameter x_s as a function of ρ , taken from the allowed region in Fig. 40.

be emphasized that this is not the result of a sophisticated analysis, which is difficult to do because of the non-Gaussian nature of the theoretical errors.

The decay modes which will probably be used to measure the CP violating angles are given in Table 14, with their branching ratios.

Finally, I list in Table 15 the CP violation and B_s mixing measurements of prime importance and my guess on which experiments, should they be built, are likely to perform these measurements and which could possibly perform them.

The B system challenges us with the possibility of very diverse and important measurements. Hopefully this physics will be done by the machines and experiments in the next and future decades.

Table 14. Branching ratios for decay modes used in measuring CP violation

CKM angle	Modes	\mathcal{B}	Product \mathcal{B}
β	ψK_S	0.4×10^{-3}	3.7×10^{-5}
α	$\pi^+\pi^-$	0.9×10^{-5}	0.9×10^{-5}
γ^{100}	$D^0 K^-$	3.3×10^{-4}	4.0×10^{-5}
	$\overline{D}^0 K^-$	4.1×10^{-6}	4.9×10^{-7}
	$D_{CP}^0 K^-$	2.2×10^{-5}	2.6×10^{-6}
γ^{101}	$K^\pm \pi^0, \pi^\pm \pi^0$	$\approx 10^{-5}$	$\approx 10^{-5}$
	$K^0 \pi^\pm, K^\pm \eta^{(\prime)}$	each	each

Table 15. Prospects for CP violation and B_s mixing measurements

Quantity	Modes	Possible	Likely
$\sin(2\alpha)$	$\pi^+\pi^-$	Babar, Belle	LHC-B, BTeV
$\sin(2\beta)$	ψK_S	HERA-B, CDF, CLEO	Babar, Belle, LHC-B, BTeV
$\sin(2\gamma)$	$K\pi$	Babar, Belle, CLEO	
$\sin(2\gamma)$	$D^0 K^-$	Babar, Belle, CLEO	LHC-B, BTeV
x_s	ψK^*		LHC-B, BTeV

6. Acknowledgements

I have benefited greatly by physics discussion with many of my colleagues, most recently with M. Artuso, K. Berkelman, T. Skwarnicki, M. Witherell, J. Rosner and M. Gronau, M. Neubert, C. Sachrajda, A. Ali and A. Buras. I have also learned a lot from people associated with new B efforts including, J. Butler, C. Bebek, M. Procario, P. McBride, T. Ypsilantis and P. Schlein. I also thank Thomas Ferbel and Barbara Ferbel for arranging such an interesting school. I learned a lot and so did Julia. My special thanks to J. Rosner, K. Berkelman, M. Witherell and T. Skwarnicki for reading through the manuscript and making many useful comments.

7. REFERENCES

1. S. L. Glashow, *Nucl. Phys.* 22, 579 (1961); S. Weinberg, *Phys. Rev. Lett.* 19, 1264 (1967); A. Salam in *Elementary Particle Theory*, ed. N. Svartholm, Almqvist and Wisksell, Stockholm (1968).
2. N. Cabibbo, *Phys. Rev. Lett.* 10, 531 (1963); M. Kobayashi and K. Maskawa *Prog. Theor. Phys.* 49, 652 (1973).
3. L. Wolfenstein *Phys. Rev. Lett.* 51, 1945 (1983).
4. W. J. Marciano and A. Sirlin, *Phys. Rev.* D22, 2695 (1980).
5. R. M. Barnett et al., *Phys. Rev.* D54, 1 (1996).
6. S. W. Herb et al., (CFS Collaboration) *Phys. Rev. Lett.* 39, 252 (1977).
7. J. K. Bienlein et al., *Phys. Lett.* B78, 360 (1978). See also C. W. Darden et al., *Phys. Lett.* B78, 364 (1978).
8. D. Besson et al., *Phys. Rev. Lett.* 54, 381 (1985).
9. S. Behrends et al., *Phys. Rev. Lett.* 50, 881 (1983).
10. M. S. Alam, et al., *Phys. Rev.* D50, 43 (1994).
11. For an excellent description of the techniques used at PEP and PETRA see W. B. Atwood and J. A. Jaros, "Lifetimes," in *B Decays* 2nd edition revised, ed. S. Stone, World Scientific, Singapore (1994).
12. For an excellent description of the techniques used at LEP and CDF see V. A. Sharma and F. V. Weber "Recent Measurements of Lifetimes of b Hadrons," in *B Decays* 2nd edition revised, ed. S. Stone, World Scientific, Singapore (1994).
13. CDF results from T. Huffman, "CDF B Results and Upgrade," and LEP results from R. Hawkings, "B-Lifetimes," at "BEAUTY '96," 4th International Workshop on B-Physics at Hadron Machines June 17-21, 1996 - Roma, Italy to appear in proceedings. SLD results from K. Abe et al. *Phys. Rev. Lett.* 75, 3623 (1995).
14. CDF Collaboration, "Branching Fractions of $B^+ \rightarrow \psi(2S)K^+$ and $B^0 \rightarrow \psi(2S)K^{*0}$ Decays at CDF," ICHEP96/pa01-86c, FERMILAB-Conf-96/160-E
15. C. Albajar et al., *Phys. Lett.* B186, 237 (1987); B213, 405 (1988); B256, 121 (1991).
16. K. Abe et al., *Phys. Rev. Lett.* 75, 1451 (1995).
17. D. M. Jansen et al., *Phys. Rev. Lett.* 74, 3118 (1995).
18. B. Grinstein, N. Isgur and M. B. Wise, *Phys. Rev. Lett.* 56, 258 (1986); F. J. Gilman and R. Singleton, *Phys. Rev.* D41, 142 (1990); K. Hagiwara, A. D. Martin and M. F. Wade, *Nucl. Phys.* B327, 569 (1989).
19. J. D. Richman and P. R. Burchat, *Rev. Mod. Phys.* 67, 893 (1995), and references contained therein.
20. T. Bergfeld et al., "Measurement of $\mathcal{B}(\bar{B}^0 \rightarrow D^+ \ell^- \bar{\nu})$ and Extraction of $|V_{cb}|$. CLEO-CONF 96-3, ICHEP-96 PA05-78 (1996).

21. M. Wirbel, B. Stech and M. Bauer *Z. Phys.* C29, 637 (1985); M. Bauer and M. Wirbel, *Z. Phys.* C42, 671(1989).
22. J. G. Korner and G. A. Schuler *Z. Phys.* C38, 511(1988); *ibid.*, (erratum) C41 690 (1989).
23. N. B. Demchuk, I. L. Grach, I. M. Narodetski, S. Simula, “ Heavy-to-heavy and heavy-to-light weak decay form factors in the light-front approach: the exclusive 0^- to 0^- case,” INFN-ISS 95/18, hep-ph/9601369 (1996).
24. B. Barish et al., *Phys. Rev.* D51, 1014 (1995).
25. D. Bortoletto et al., *Phys. Rev. Lett.* 16, 1667 (1989).
26. H. Albrecht et al., *Z. Phys.* C57, 533(1993).
27. D. Buskulic et al., *Phys. Lett.* B359, 236 (1995).
28. P. Abreu et al., CERN-PPE/96-11 (1996).
29. B. Grinstein, N. Isgur and M. B. Wise, *Phys. Rev. Lett.* 56, 258 (1986).
30. N. Isgur, D. Scora, B. Grinstein, and M. B. Wise, *Phys. Rev.* D39, 799 (1989).
31. W. Jaus, *Phys. Rev* D41, 3394 (1990).
32. N. Isgur and M. B. Wise, “Heavy Quark Symmetry,” in *B Decays* Revised 2nd Edition, World Scientific, Singapore (1994) p231; N.Isgur and M.B. Wise, *Phys. Rev.* D42 2388 (1990); N. Isgur and M. B .Wise, *Phys. Lett.* B232 113 (1989); *ibidem* B237, 527 (1990); M. B. Voloshin and M. A. Shifman, *Sov. J. Nucl.Phys.* 45 292 (1987); *ibidem* 47, 511 (1988); H. D. Politzer and M. B. Wise, *Phys. Lett.* 206B 681 (1988) 681; *ibidem* B208, 504 (1988); E. Eichten and B. Hill, *Phys. Lett.* B234, 511 (1990); H.Georgi, *Phys .Lett.* B240B 447 (1990); B.Grinstein, *Nucl. Phys.* B339, 253 (1990); A.F.Falk, H.Georgi, B.Grinstein and M. B .Wise, *Nucl. Phys.* B343, 1 (1990).
33. M. Neubert, *Int. J. Mod. Phys.* A11, 4173 (1996), hep-ph/9604412.
34. M. E. Luke, *Phys. Lett.* B252, 447 (1990).
35. A. Czarnecki, *Phys. Rev. Lett.* 76, 4121 (1996); M. Shifman, N.G. Uraltsev and A. Vainshtein, *Phys. Rev.* D51, 2217 (1995); M. Shifman and N. G. Uraltsev, *Int. J. Mod. Phys.* A10, 4705 (1995).
36. H. Albrecht et al., *Z. Phys.* C57, 533 (1993).
37. B. Barish et al., *Phys. Rev.* D51, 1041 (1995).
38. D. Buskulic et al., *Phys. Lett.* B359, 236 (1995).
39. P. Abreu et al., CERN-PPE/96-11 (1996), submitted to *Z. Phys. C*.
40. J. Bartelt et al., “Inclusive Measurements of B -meson Semileptonic Branching Fractions,” submitted to Lepton Photon conf., Cornell (1993), CLEO-CONF 93-19.
41. B. Barish et al., *Phys. Rev. Lett.* 76, 1570 (1996).
42. H. Albrecht et al., (ARGUS) *Phys. Lett* B318, 397 (1993).
43. G. Altarelli, N. Cabibbo, G. Corbo and L. Maiani *Nuclear Phys.* B208, 365 (1982).
44. T. Skwarnicki, “Decays of b Quark,” in Proc. of Lepton Photon Conf., Beijing, China August 1995, hep-ph/9512395.

45. R. Fulton et al., *Phys. Rev. Lett.* 64, 16 (1990).
46. H. Albrecht, et al., *Phys. Lett.* B234, 409 (1990).
47. J. Bartelt et al., *Phys. Rev. Lett.* 71, 4111 (1993).
48. G. Fox and S. Wolfram, *Phys. Rev. Lett.* 41, 1581 (1978).
49. M. Artuso, *Phys. Lett.* B311, 307 (1993).
50. M. Artuso, “CLEO Results,” presented at **Beauty ’96**, Rome, Italy, June 1996, to appear in proceedings.
51. J. Alexander et al., preprint CLNS 96/1419, CLEO 96-9 (1996).
52. R. Fulton et al. (CLEO), *Phys. Rev. Lett.* 64, 16 (1990); H. Albrecht et al. (ARGUS), *Phys. Lett.* B234, 409 (1990); a table of results and the average is given in S. Stone, “Semileptonic B Decays,” in **B Decays** revised 2nd edition, ed. S. Stone, World Scientific, Singapore (1994) p349.
53. Since the resolution on is about 2.5 worse than the resolution on $|p_{miss}|$ (≈ 110 MeV), the neutrino four-vector is defined as $(E_\nu, \vec{p}_\nu) = (|\vec{p}_{miss}|, \vec{p}_{miss})$.
54. M. Gaillard and B. Lee, *Phys. Rev.* D10, 897, (1974); J. Hagelin, *Phys. Rev.* D20, 2893, (1979); A. Ali and A. Aydin, *Nucl. Phys.* B148, 165 (1979); T. Brown and S. Pakvasa, *Phys. Rev.* D31, 1661, (1985); S. Pakvasa, *Phys. Rev.* D28, 2915, (1985); I. Bigi and A. Sanda, *Phys. Rev.* D29, 1393, (1984).
55. H. Albrecht et al., *Phys. Lett.* B192, 245 (1983).
56. Using the ratio of like-sign to opposite sign dilepton events, UA1 published a mixing signal at the 3σ level that resulted from a combination of B_s and B_d , see C. Albajar et al., *Phys. Lett* B186, 245 (1987).
57. R. Akers et al., A Measurement of the B_d^0 Oscillation Frequency using Letponts and $D^{*+}\ell^-$ mesons, CERN-PPE/96-74 (1996); R. Akers et al., *Z. Phys.* C66 555 (1995).
58. C. Zeitnitz, “Oscillations and Mixing,” presented at BEAUTY 96.
59. R. Ammar et al., *Phys. Rev. Lett.* 71, 674 (1993).
60. R. Ammar et al., “Radiative Penguin Decays of the B Meson,” CLEO-CONF 96-6 (1996).
61. R. A. Fischer, “The Use of Multiple Measurements in Taxonomic Problems,” *Annals of Eugenics* 7, 179 (1936); M. G. Kendall and A. Stuart, “The Advanced Theory of Statistics,” Volume III, Hafner Publishing, NY 2nd edition (1968).
62. M. S. Alam et al., *Phys. Rev. Lett.* 74, 2885 (1995).
63. S. Bertolini, F. Borzumati and A. Masiero, *Phys. Rev. Lett.* 59, 180 (1987); R. Grigjanis et al., *Phys. Lett. B* 213, 35 (1988); B. Grinstein, R. Springer and M. Wise *Nucl. Phys.* B339, 269 (1990); see also N. G. Desphande, “Theory of Penguins in B Decay,” in **B Decays** Revised 2nd Edition, ed. S. Stone, World Scientific, Singapore (1994).
64. M. Ciuchini et al., *Phys. Lett.* B334, 137 (1994).
65. K. Chetyrkin and M. Misiak, ‘ $b \rightarrow s\gamma$ Decay Beyond Leading Logarithms,’ pa08-005, presented at ICHEP ’96, Warsaw, Poland, August (1996).
66. M. Battle et al., *Phys. Rev. Lett.* 71, 3922 (1993).

67. D. Asner et al., *Phys. Rev.* D53, 1039 (1996).
68. S. Playfer and S. Stone, "Rare B Decays," *Int. Journal of Mod. Phys.* A10, No 29. 4107, (1995).
69. B. Barish et al., "Observation of the Decay $B \rightarrow \omega\pi^+$," CONF 96-23, ICHEP-96 PA05-95 (1996).
70. W. Adam et al., "Study of Rare B Decays with the DELPHI Detector at LEP," CERN PPE 96-67 (1996).
71. P. Langacker, "CP Violation and Cosmology," in **CP Violation**, ed. C. Jarlskog, World Scientific, Singapore p 552 (1989).
72. A. J. Buras, "Theoretical Review of B-physics," in **BEAUTY '95** ed. N. Harnew and P. E. Schlein, *Nucl. Instr. and Meth.* A368, 1 (1995).
73. A. Carter and A. I. Sanda, *Phys. Rev. Lett.* 45, 952 (1980); *Phys. Rev.* D23, 1567 (1981); I. I. Bigi and A. I. Sanda, *Nucl. Phys.* B193, 85 (1981); *ibid* B281, 41 (1987).
74. I. Bigi, V. Khoze, N. Uraltsev, in **CP Violation**, ed. C. Jarlskog, World Scientific, Singapore 175 (1989).
75. M. Gronau, *Phys. Rev. Lett.* 63, 1451 (1989); M. Gronau and D. London, *Phys. Rev. Lett.* 65, 3381 (1990).
76. D. Atwood, B. Blok and A. Soni, *Int. J. Mod. Phys.* A11, 3743 (1996); see also N. Deshpande, X. He & J. Trampetic, Preprint OITS-564-REV (1994); see also J. M. Soares, *Phys. Rev.* D53, 241 (1996). G. Eilam, A. Ioannissian R. R. Mendel and P. Singer, *Phys. Rev.* D53, 3629 (1996).
77. A. Ali, C. Greub and T. Mannel, "Rare B Decays in the Standard Model," in Hamburg 1992, Proceedings, ECFA Workshop on a European B-meson Factory, Eds. R. Aleksan and A. Ali, p155 (1993).
78. C. Albajar et al., *Phys. Lett.* B262, 163 (1991).
79. R. Balest et al., "Search for $B \rightarrow K\ell^+\ell^-$ and $B \rightarrow K^*\ell^+\ell^-$ decays," CLEO-CONF 94-4 (1994).
80. F. Abe et al., *Phys. Rev. Lett.* 76, 2015 (1996).
81. R. Ammar et al., *Phys. Rev.* D49, 5701 (1994); M. Artuso, et al., *Phys. Rev. Lett.* 75, 785 (1995).
82. D. Buskulic et al., *Phys. Lett.* B343, 444 (1995).
83. A. Ali and T. Mannel, *Phys. Lett.* B264, 447 (1991). Erratum, *ibid*, B274, 526 (1992).
84. The use of asymmetric beam energies to study CP violation in e^+e^- machines operating the $\Upsilon(4S)$ was first suggested by Pierre Oddone.
85. D. S. Akerib et al., *Phys. Rev. Lett.* 67, 1692 (1991).
86. S. Stone, *Mod. Phys. Lett.* A3, 541 (1988).
87. E. Blucher et al., *Nucl. Instr. and Meth.* A249, 201 (1986); Y. Kubota et al., *Nucl. Instr. and Meth.* A320, 66 (1992).
88. M. Artuso, *Nucl. Instr. and Meth.* A371, 324 (1996); B. N. Ratcliff, *Nucl. Instr. and Meth.* A371, 309 (1996)

89. M. Gluck, J. F. Owens and E. Reya, *Phys. Rev. D* **17**, 2324 (1978); B. L. Cambridge, *Nucl. Phys.* **B151**, 429 (1979); P. Nason et al., *Nucl. Phys.* **B327**, 49 (1989); W. Beenakker et al., *Nucl. Phys.* **B351**, 507 (1991), *Phys. Rev. D* **40**, 54 (1989).
90. F. Abe et al., *Phys. Rev. D* **53**, 1051 (1996). See also, M. Artuso, "Experimental Facilities for b-Quark Physics," in *B Decays* revised 2nd Edition, Ed. S. Stone, World Scientific, Singapore (1994).
91. M. Mangano, P. Nason and G. Ridolfi, *Nucl. Phys.* **B373**, 295 (1992).
92. F. Abe et al., *Phys. Rev. Lett.* **75**, 1451 (1995). Previous UA1 measurements agreed with the theoretical predictions, see C. Albajar et al., *Phys. Lett.* **B256**, 121 (1991). Recent D0 measurements agree with both the CDF measurements and the high side of the theoretically allowed range. See S. Abachi et al., *Phys. Rev. Lett.* **74** 3548 (1995).
93. S. Erhan, *Nucl. Instr. and Meth.* **A368**, 133 (1995).
94. For more information, the reader is referred to proceedings of conferences called "Beauty 93" through "Beauty 96," the proceedings of which are published by Nucl. Instru. and Methods volumes **A333** (1993), **A351** (1994), **A368** (1995).
95. J. N. Butler, "The BTeV Experiment at Fermilab," presented at 2nd Int. Conf. on Hyperons, Charm and Beauty Hadrons, Montreal, Quebec, Canada, Aug. 1996.
96. J. Ellet et al., *Nucl. Instr. and Meth.* **A317** 28, (1992).
97. M. Procaro, "B Physics Prospects Beyond the year 2000," presented at the 10th Topical Workshop on Proton-Antiproton Collider Physics, to appear in proceedings, Fermilab-BONF-95/166.
98. P. McBride and S. Stone, *Nucl. Instr. and Meth.* **A368**, 38 (1995).
99. A. G. Cohen et al., "B-Factory Physics from Effective Supersymmetry," UW-PT-95-22, hep-ph/9610252 (1996); J. L. Hewett and J. D. Wells, "Searching for supersymmetry in rare B decays," SLAC-PUB-7290, hep-ph/9610323 (1996); Y. Nir and H. R. Quinn, "Theory of CP Violation in B Decays," in *B Decays* ed. S. Stone, World Scientific, Singapore p520 (1994).
100. M. Gronau and D. Wyler, *Phys. Lett.* **B265**, 172 (1991).
101. M. Gronau, J. L. Rosner and D. London, *Phys. Rev. Lett.* **73**, 21 (1994).